

Non-linear diffusion in fractured porous media and application to dual-medium inter-porosity flux

Sina Momeni

▶ **To cite this version:**

Sina Momeni. Non-linear diffusion in fractured porous media and application to dual-medium inter-porosity flux. Earth Sciences. Sorbonne Université, 2022. English. NNT : 2022SORUS496 . tel-04043143

HAL Id: tel-04043143
https://theses.hal.science/tel-04043143

Submitted on 23 Mar 2023

HAL is a multi-disciplinary open access archive for the deposit and dissemination of scientific research documents, whether they are published or not. The documents may come from teaching and research institutions in France or abroad, or from public or private research centers.

L'archive ouverte pluridisciplinaire **HAL**, est destinée au dépôt et à la diffusion de documents scientifiques de niveau recherche, publiés ou non, émanant des établissements d'enseignement et de recherche français ou étrangers, des laboratoires publics ou privés.

Sorbonne Université

ED 398 - Géosciences, Ressources Naturelles et Environnement

IFP Energies Nouvelles / Direction Sciences de la Terre et Technologies de l'Environnement

Non-linear diffusion in fractured porous media and application to dual-medium inter-porosity flux

Par Sina MOMENI

Thèse de doctorat en Géosciences

Dirigée par Dr. Benoît NOETINGER

Présentée et soutenue publiquement le 22 novembre 2022

Devant un jury composé de :

Pr. LAGREE Pierre Yves	Directeur de Recherche	CNRS	Président
Dr. SOULAINE Cyprien	Chargé de Recherche	CNRS	Rapporteur
Dr. MEHEUST Yves	Maître de Conférences	Université de Rennes1	Rapporteur
Dr. ROUBINET Delphine	Chargée de Recherche	CNRS	Examinateur
Dr. KLEPIKOVA Maria	Chargée de Recherche	CNRS	Examinateur
Dr. NOETINGER Benoît	Ingénieur de Recherche	IFPEN	Directeur de thèse
Dr. DOUARCHE Frederic	Ingénieur de Recherche	IFPEN	Promoteur de thèse
Dr. BRACONNIER Benjamin	Ingénieur de Recherche	IFPEN	Co-promoteur de thèse
Pr. QUINTARD Michel	Directeur de Recherche	CNRS	Invité

Except where otherwise noted, this work is licensed under
http://creativecommons.org/licenses/by-nc-nd/3.0/

Acknowledgment

I want to express my most sincere acknowledgments to all the people who in one way or another have made it possible to accomplish this work. I want to express my deepest gratitude to my supervisors, Dr. Frederic Douarche, Dr. Benoit Neotinger, and Dr. Benjamin Braconnier for their support, encouragement, feedback, and patience throughout this project. I have learned a lot from you!

Special thanks to our consultant and advisor Pr. Michel Quintard and to my former supervisor Dr. Bernard Bourbiaux for their time and comments.

I am also very thankful to committee members Dr. Cyprien Soulaine, Dr. Yves Meheust, Dr. Delphine Roubinet, Dr. Maria Klepikova, and Pr. Pierre Yves Lagree for accepting our invitation and for their contribution to this dissertation.

I would like to thank colleagues and friends at IFP Energies Nouvelles for supporting me and who made my stay pleasant during these three years of PhD, Djamela Buda, Dr. Narges Dashtbesh, Marc Perret, Ancilla Almeida, and many others. Also, Thanks IFP Energies Nouvelles for giving me the opportunity and financial support to reach this goal in my professional life.

And finally, I am very grateful to my family and friends for their support and encouragement since as far as I can remember, and for helping me achieving what I consider to be a successful education. I want to deeply thank my beloved, Sara, for her love, understanding, patience, and endless help.

Abstract

Transfers in fractured porous media are involved in many industrial applications such as oil production, geothermal exploitation, soil remediation, or geological storage. Dimensional analysis of matrix-fracture transfers must consider all physical mechanisms driving transfers, pressure diffusivity, gravity/segregation, capillary force, viscous flow, molecular diffusion for compositional transfers, and chemical alteration of fluid/rock. Modeling and up-scaling these transfers in linear and non-linear forms remain a major challenge in many applications. The "dual-medium" model is a powerful tool for up-scaling transfers to the matrix block scale of Naturally Fractured Reservoirs but, unfortunately, most of their formulations rely on the asymptotic value (at large/late times) of a so-called "shape factor" in a single-phase flow context. This research increases the reliability of the up-scaling of matrix-fracture dual-medium models that are adopted to simulate fluid or heat transport at the scale of geological reservoirs.

Analytical solutions for single-phase diffusion are well-known at the Darcy-scale. These Darcy-scale models provide reference solutions whose physical analysis helps in setting up the up-scaling methods for parameterizing macro-scale models based on the dual-medium concept. This study derived an analytical shape factor for linear diffusion in the dual-medium model with specific fracture boundary conditions and suggested a correction function to modify the dual-medium numerical simulator. The matrix-fracture transfer time is characterized by early- and late-time behaviors that turned to our methodology to solve the non-linear two-phase transfer.

In many situations of practical interest, capillarity is the dominant driving force, and the saturation-dependent diffusion coefficient vanishes at the saturation end points, which renders the driving equation highly singular. We revisit this non-linear problem with Dirichlet boundary condition by presenting two exact asymptotic solutions valid for early- and late-times, under the assumption that the non-linear diffusion coefficient vanishes as a power-law of both phase saturations at the extreme values of the fluid saturation. In the early-time an exact self-similar solution is adopted. Focusing on the late-time domain, the asymptotic solution is derived using an Ansatz that is written under the form of a power-law time decay of the NAPL saturation. The spatial variations of the solution are given analytically for a one-dimensional porous medium corresponding to parallel fracture planes. The analytical solution is in very good

agreement with the results of numerical simulations involving various realistic sets of input transport parameters.

Generalization to the case of two- or three-dimensional matrix blocks of arbitrary shape is proposed using a similar Ansatz. A fast-converging algorithm based on a fixed-point sequence starting from a suitable first guess was developed. Comparisons with full-time simulations for several typical block geometries show an excellent agreement.

These analytical results generalize the linear single-phase representation of matrix-to-fracture exchange term to two-phase capillary imbibition transfer. This formulation accounts for the non-linearity of the local flow equations using the power-law dependence of the conductivity for low NAPL saturation. The corresponding exponent can be predicted from the input conductivity parameters. Similar findings are also presented and validated numerically for two- or three-dimensional matrix blocks. Finally, we present a matrix-fracture transfer model with a characteristic time that scales the full range of a counter-current capillary imbibition in a multi-dimensional system.

That original approach paves the way to research leading to a more faithful description of matrix-to-fracture exchanges when considering a realistic fractured medium composed of a population of matrix blocks of various size and shapes.

Nomenclature

L,l	block length
R,r	radius, radial coordinate
h	matrix block height
t	time
x,y,z	cartesian space coordinates
$\mathbf{x}$	position in space
P	pressure
ϕ	porous medium porosity
ρ	phase density
S	phase saturation
C	mass fraction of chemical species
$\boldsymbol{u}$	Darcy velocity
$\boldsymbol{J}$	molecular diffusion-dispersion
$\dot{Q}$	source term volumetric rate
$\mathbf{k}$	absolute permeability tensor
k	absolute permeability scalar
k_r	relative permeability
$\bar{k}$	permeability average
μ	fluid dynamic viscosity
m	capillary pressure exponent
p, q	Corey's rel. perm. exponent
κ	maximum relative permeabilit
$\boldsymbol{g}$	gravity acceleration
γ	interfacial tension
θ	contact angle between fluid and rock
P_c	capillary pressure
c_{fluid}	isothermal fluid compressibility
c_{rock}	isothermal rock compressibility
c_t	total compressibility
η	pressure diffusivity coefficient
τ	characteristic time
σ	shape factor
N	number of parallel fracture sets
f	transfer across block face
F	matrix-fracture total transfer
D	diffusion coefficient
β	dispersivity coefficient
Φ	matrix-fracture flux
λ	phase mobility
τ_s	porous medium tortuosity
$\mathfrak{C}$	control volume/calculation cell
Ω, Γ	domain, boudary surface of domain
dv	elementary control volume unit
$d\Gamma$	elementary unit of boundary surface
$\boldsymbol{n}$	unit normal of the surface
$\boldsymbol{v}$	fluid velocity
A	surface area between cells
$A_{0,\infty}$	matrix-fracture flux prefactors
V	volume of matrix block
E	error function
L_c	characteristic length
l_{cap}	capillary length
J	molecular diffusion transfer rate
M	end point mobility ratio/total mass
Bo	Bond number
Ca	capillary number
Ψ	correction factor
ξ	Boltzmann variable
α	saturation exponent at diffusion asymptotics
$B(x; a, b)$	Euler incomplete beta function
$\Gamma(z)$	Euler gamma function

Subscripts/Superscripts

x,y,z	cartesian directions
m	matrix
f	fracture
φ	phase
c	chemical species

t	total	t,d	transfer mechanism type
w	water	s	block lateral faces
o	oil	eff	effective
g	gas	Max	maximum
ir	irreducible	min	minimum
i,j	cell denotes	tr	transient
n,l	numerical scheme index	PSS	pseudo steady-state

Table of contents

Acknowledgment 2
Abstract 3
Nomenclature 5
Table of contents 7
1 Introduction 9
1.1 Fractured Reservoirs 9
1.1.1 Characterization 9
1.1.2 Transfer mechanisms and recovery challenges 10
1.1.3 Modeling at different scales 13
1.1.4 Introduction to multi-phase fluid flow in porous media at the Darcy-scale 15
1.1.5 Single-phase pressure flow in porous media at Darcy-scale 16
1.1.6 Up-scaling fractured porous media 18
1.2 Objectives of the Ph.D. project 24
1.3 Methods, tools, data 26
1.4 References 28
2 Single-phase Diffusion Transfer in Fractured Porous Media 30
2.1 Pressure diffusion (viscous flow) in the matrix block 30
2.2 Molecular diffusion in the matrix block 31
2.3 Analytical solution of constant fracture condition 32
2.4 Up-scaling the matrix-fracture single-phase flux with dual-medium model 35
2.5 Literature review on dual-medium shape factors 40
2.6 Numerical simulation of linear diffusion with fine-grid and dual-medium model 45
2.7 Methodology to improve/up-scale transient diffusion transfer in dual-medium model 48
2.8 Discussion 53
2.9 References 55
3 Non-linear Diffusion Transfer in Fractured Porous Media 57
3.1 Introduction 57
3.2 Driving equations 59
3.2.1 Driving forces involved in matrix-fracture transfers to consider capillary imbibition 62
3.2.2 Counter-current imbibition in the three-dimensional incompressible two-phase flow case without gravity 64
3.2.3 Driving equations in the one-dimensional case 66
3.2.4 Analyzing the non-linear diffusion coefficient of counter-current capillary imbibition transfer 67
3.2.5 Numerical fine-grid simulations 71
3.3 Some previous solutions to the capillary imbibition problem 71
3.3.1 Specific form of capillary diffusion coefficient 72

3.3.2 Semi-infinite solutions 74
3.3.3 Scaling with experimental analysis 75
3.4 Early time solution 78
3.4.1 Power law diffusion function 78
3.4.2 General non-linear diffusion function (Parlange extension) 82
3.5 Late time solution 86
3.6 Non-linear closure for matrix-fracture flux 90
3.7 Generalization to 2D and 3D blocks 94
3.7.1 Early-time regime 95
3.7.2 Late-time regime 95
3.7.3 Fixed-point algorithm 96
3.7.4 Results 97
3.8 Ongoing work 103
3.9 Discussion 105
3.10 References 107
Conclusions and perspectives 113
Annex A. Puma reservoir numerical discretization and discrete equations 116
Convergence study 120
Annex B. Preliminary numerical verification of dual-medium model 125
Dual-medium fluid flow 125
Matrix-fracture dual-medium simulator 126
Annex C. Numerical scheme of non-linear diffusion 132
Cylindrical geometry 134
Spherical geometry 134
Scilab code 135
Annex D. Fixed-point algorithm 145
List of figures 148
List of tables 152

1 Introduction

This chapter introduces fractured porous media and their characteristics including transfer mechanisms at different scales to produce from a matrix block. Fluid flow modelling methods in this system are usually oversimplified to avoid expensive calculations at large scales. We present the principle of the dual-medium approach as a typical up-scaling method, where the oversimplifications make some downsides. Finally, the chapter presents our method and tools to improve the matrix-fracture transfer up-scaling in single-phase condition.

1.1 Fractured Reservoirs

Fractured reservoirs are geological porous media in which geochemical or tectonic activity has disrupted the rock's continuity. Carbonate rocks (Mg/Ca -CO_3) are mostly prone to fracturing. These discontinuities introduce complexity in the internal structure and the flow of fluids within fractured reservoirs. They induce strong contrasts of transport characteristic times, which is known as one of the most challenging problems in up-scaling transport in multi-scale systems. Figure 1-1 illustrates these discontinuities of rock blocks (so-called matrix blocks) including fractures, open channels, vugs, and stylolites.

Transfers in fractured porous media are involved in many industrial applications such as water management, oil production, geothermal exploitation, soil remediation, or geological storage. Fractured oil reservoirs include a large share (~50 to 60 percent) of the world's oil reserves (Burchette, 2012). Besides, the geothermal energy domain, either for electricity generation or for direct applications of geothermal heat, carries out the energy in a wide range of geological settings including fractured reservoirs. The most essential requirements for a geothermal reservoir are sufficient temperature and permeability, which can be provided by fracture networks.

1.1.1 Characterization

Geologists characterize fractured reservoirs mainly by the following fracture parameters: (a) distance between fractures (fracture spacing), (b) direction (or azimuth) and dip of fracture planes, (c) fracture length, (d) fracture aperture and degree of cementation.

The above parameters are inferred from several sources of information such as: description of cores, Seismic profiles, outcrops, Production Logging Tools, Bore Hole Images, fluid contacts, etc. The characterization of Naturally Fractured Reservoirs (NFR) shows specific challenges in fluid flow and recovery process that are introduced afterward.

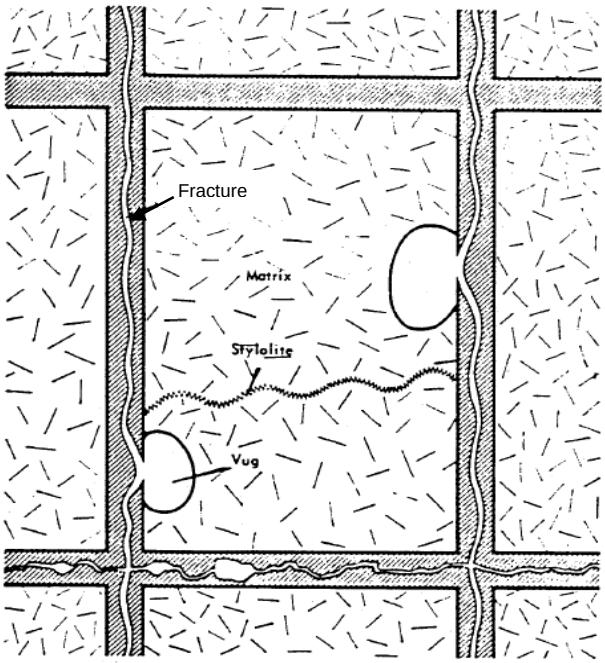


Figure 1-1 Illustration of an element of a fractured porous media including parallel fractures, open channels, vugs, and stylolite (Reiss, 1980).

1.1.2 Transfer mechanisms and recovery challenges

Fractured reservoirs present complex recovery mechanisms because inhomogeneous fractures with large transmissibility are in contact with low transmissibility matrix blocks and these matrix blocks are the primary fluid container. The transfer mechanisms include fluid expansion, solution gas drive, viscous flow, capillary imbibition, gravity segregation/drainage, rock compaction, molecular diffusion, heat conduction for non-isothermal transfers, and chemical alteration of the matrix. Figure 1-2 shows the main physical driving mechanisms in this study, which are important for many fluid or heat transfer applications.

As the pressure drops in the fracture system, during production time, fluid expands and flows out from the matrix block to equilibrate the matrix pressure with the surrounding fracture pressure, which is mentioned as pressure diffusion. Also, the compressibility of rock can gain importance in case of low fluid compressibility or low porosity.

If matrix and fracture are saturated with different fluids with different densities, gravity creates a pressure difference between the matrix and the fracture. This additional potential difference may force water or gas from the fracture into the matrix and expel the oil out of the matrix; this process is called gravity drainage. The matrix block height and fluid densities have a huge impact on this mechanism, which usually has a small contribution in comparison with other mechanisms.

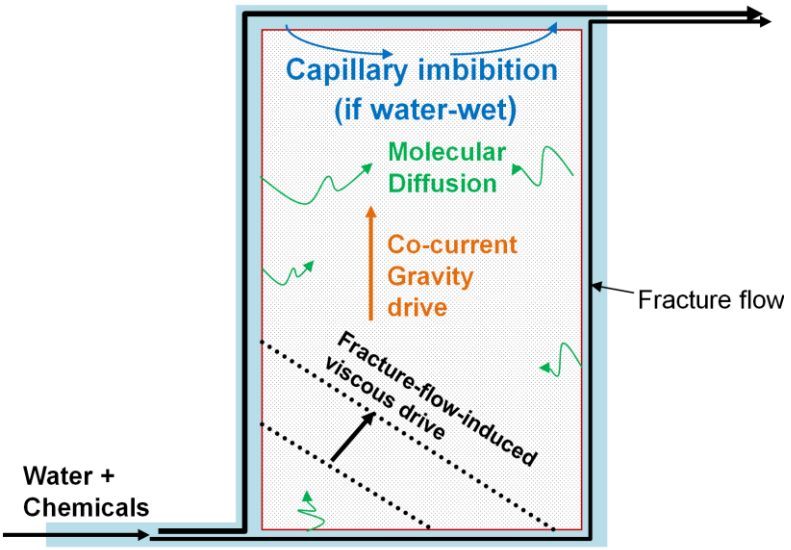


Figure 1-2 A schematic of main matrix-fracture transfer mechanisms in a matrix block (dotted rectangle area) surrounded by fractures flowing with water (light blue). The arrows guide to understand the flow paths.

Due to the flow in the fracture network, there can be a pressure gradient in the fracture system along the two faces of the block (see Figure 1-2). Normally in this condition, most of the water bypasses the matrix block through the high permeable fracture network, which leads to poor sweep efficiency and low recoveries.

Also, preferential affinities of the matrix rock for different fluids give rise to capillary forces that can improve or inhibit matrix-fracture transfers (such a mechanism depends on the propensity of the porous medium that constitutes the matrix block to spontaneously imbibe water or oil, or more significantly trap one of them). The water invading the fractures imbibes into the matrix, displacing oil in a co-current or counter-current way. As we will show later in chapter 3, the rate of imbibition depends strongly on rock and fluid properties and is more effective in the case of a water-wet matrix rock. Modeling of this two-phase transfer mechanism is the main objective of this study.

In fractured reservoirs, as opposed to non-fractured reservoirs, molecular diffusion may play a key role, because of the matrix-fracture contact area for diffusion. This transfer mechanism becomes dominant (not that it is more efficient than the others in absolute terms) when the other aforementioned mechanisms are not really active in the matrix-fracture system. Molecular diffusion is for example a key in chemical Enhanced Oil Recovery to change the physicochemical properties of rock or fluid. This single-phase flow is similar to viscous flow (pressure diffusion) which is discussed in chapter 2.

The respective roles played by each of these mechanisms can be quantified through dimensionless numbers such as Bond number (the ratio of gravitational forces to surface/interfacial tension forces), capillary number (the ratio of viscous forces to surface/interfacial tension forces), Peclet number (the ratio of the mechanical dispersion coefficient to the effective molecular diffusion coefficient), etc. If their transfer roles are not well appraised, development and production from fractured reservoirs can leave in place most of the fluid volume. Therefore, matrix-fracture transfer analysis in a fractured porous medium has to consider all physical mechanisms driving transfers. Based on fractured reservoirs characterization, two-phase capillary imbibition (natural or chemically assisted) is a main recovery method from the matrix blocks. However, efficient implementation of the field-scale capillary imbibition modeling in complex fractured reservoirs remains a challenge and needs precise modeling.

An overview of the diversity of matrix-fracture transfer mechanisms involved in the production of oil & gas fractured reservoirs is found in (Reis, 1990). Reis reviewed the mechanisms that allow recovering the oil from matrix blocks during steam injection in fractured reservoirs. These mechanisms include thermal expansion, capillary imbibition in water-wet blocks, gas generation, gravity drainage, chemical alteration of matrix, solution gas drive, and rock compaction. He estimated oil expulsion rates from a matrix block for each mechanism and found that the recovery characteristic time is the longest for gravity drainage, followed by capillary imbibition. Gravity drainage could be possibly effective in thick formations having high matrix permeability, low matrix capillary pressure, and continuous vertical fractures. Although such a study refers to a given recovery method and given matrix block properties, the evaluation of characteristic times for each involved physical mechanism is helpful to identify the main physical contributions to a-priori-complex recovery scenarios.

(Bourbiaux et al., 2003) gave a synthetic description of matrix-fracture transfer mechanisms (see Figure 1-3). Several difficulties related to the simulation of multiphase compositional transfers were underlined, such as:

- The representation of driving mechanisms having a directional effect like gravity, in conjunction with other non-directional, i.e., diffusive, mechanisms, like capillarity as shown in Figure 1-3;
- The long transient states of the matrix medium involved in capillary imbibition transfers.

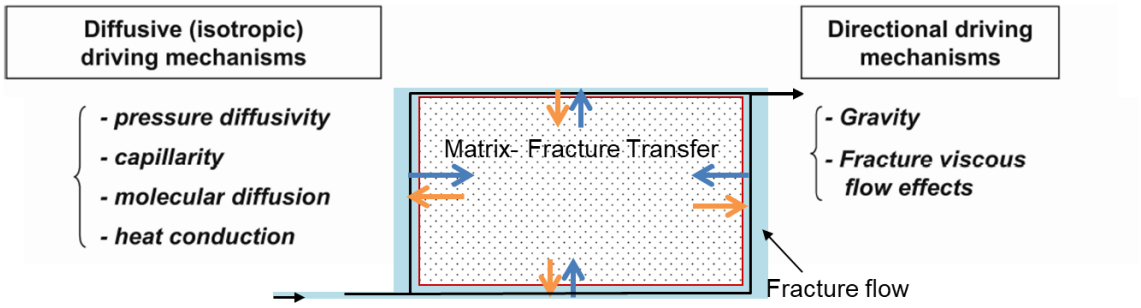


Figure 1-3 Schematics of the matrix-fracture transfer mechanisms in groups of diffusion like and directional driving (Bourbiaux et al., 2003). The blue and orange arrows show the fluid flux of aqueous and non-aqueous phases between the matrix block and the surrounding fracture network. Our study focuses on diffusive driving mechanisms.

We can understand the diffusive driving mechanisms in matrix-fracture transfer show different characteristic time in the recovery process that needs to be more evaluated.

1.1.3 Modeling at different scales

Fractured reservoir models, both geological and reservoir fluid flow models, represent a challenge for reservoir engineers. A detailed geological model needs plentiful data acquisition, which is costly and time-consuming. Even with a good knowledge of the geological structure, an exact detailed geological model still faces several challenges associated with predicting flow through fractured systems.

Porous medium modeling is typically a multi-scale problem in which transfer mechanisms may be described at pore-scale (so-called micro-scale), at the scale of laboratory cores, at matrix fine-grid scale and at the scale of the fractured geological blocks. Pore-scale is the scale of fluid/fluid and solid/fluid interfaces. In fact, smaller scale models may lead to a more accurate simulation of a larger system but will result in prohibitive computational costs.

Therefore, we may have to find an appropriate tradeoff for our concerned fluid flow in porous media behaviors in engineering.

Figure 1-4 illustrates the different scales of fluid flow problem in the context of fractured reservoirs. It starts with pore-scale formulations and a change of scale from micro-scale to local scale. We may need again to change this scale, which is the scale of small geological features (e.g. matrix surrounded by fractures), to large block scale (in macro-scale) taking into account fracture boundary condition. Modeling a system at different scales demands distribution of properties with respect to that scale. Up-scaling, or homogenization, replaces the distribution of properties of the fine grid of a heterogeneous region by an equivalent property value (i.e. a specific "average" value) assigned to a single coarse-grid block.

We start the model with the **Darcy** equation (Darcy, 1856), which is already an up-scaled model from pore-scale to local scale (or Darcy-scale). The volume averaging technique, presented by (Quintard & Whitaker, 1996; Slattery, 1967; Whitaker, 1967), is a reliable method to obtain a Darcy-scale model from pore-scale flow equations. Darcy law is applied in porous media of very various sizes, from small cores of a few millimeters to the hundreds of meters volume unit of the reservoir.

The Darcy-scale momentum balance equation has the form of a linear relationship between velocity of phase φ ($\vec{u}_\varphi$) and pressure (head or potential) gradient and it has been the fundamental principle of flow in porous media (Darcy, 1856). Darcy's law is mathematically analogous to other linear phenomenological transport laws, such as Ohm's law for electrical conduction, Fick's law for solute diffusion, and Fourier's law for heat conduction. Darcy's law for phase φ, under multi-phase flow writes:

$$\boldsymbol{u}_\varphi = -\frac{\mathbf{k} k_{r\varphi}(S_\varphi)}{\mu_\varphi}.\left(\boldsymbol{\nabla} P_\varphi - \rho_\varphi \boldsymbol{g}\right), \qquad \text{Eq. 1-1}$$

where **k** is the rock absolute permeability tensor. We will consider for simplicity that the latter is diagonal and can be written as a scalar (k) in each direction of the flow. In which, φ is the phase of fluid, k_r is the relative permeability for phase φ, μ is the fluid dynamic viscosity, P is the intrinsic pressure and $\vec{g}$ is the gravity acceleration.

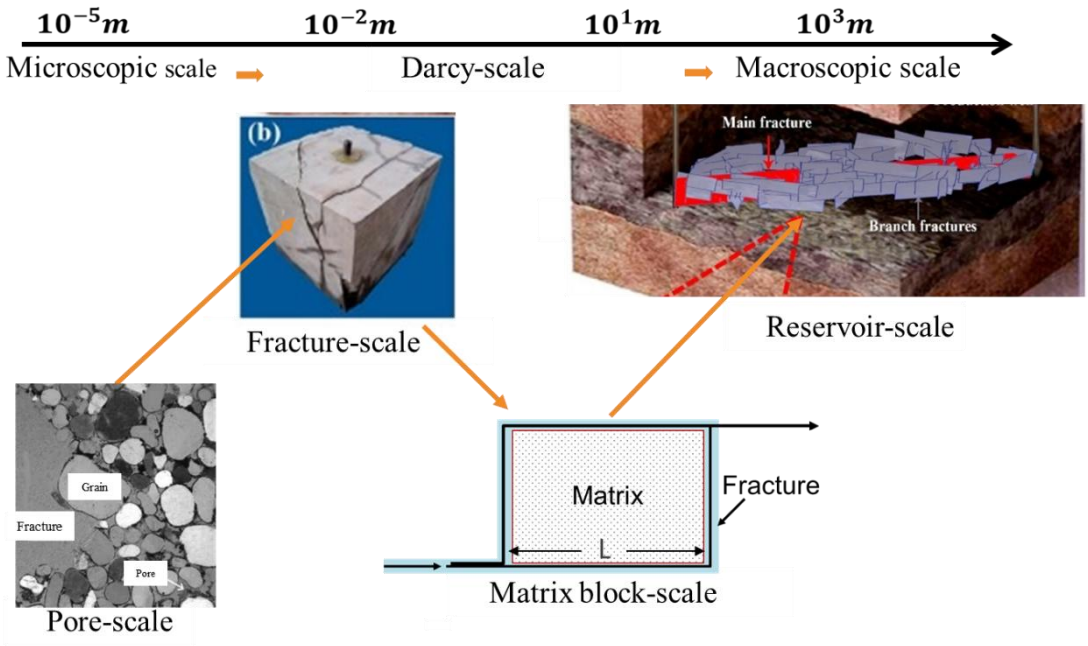


Figure 1-4 Multi-scale feature of fluid flow modeling in porous medium, up-scaling from pore-scale (Microscopic scale) to reservoir-scale (Macroscopic scale).

1.1.4 Introduction to multi-phase fluid flow in porous media at the Darcy-scale

This section gives a general overview of the governing equations for fluid flow equation in porous media at local-scale for single- and two-phase transfer. If we use the volume averaging method (Quintard & Whitaker, 1996; Slattery, 1967; Whitaker, 1967) of pore-scale equations for momentum or mass balance, we can develop the local-scale equations of pressure or molecular diffusion respectively.

Considering a control volume of porous medium $\mathfrak{C}$ at the local-scale that is fixed in space, the total mass of a component *k* in phase φ is:

$$M_{\varphi k}(t) = \int_{\mathfrak{C}} \rho_{\varphi} \phi S_{\varphi} C_{\varphi k} dv, \qquad \text{Eq. 1-2}$$

where subscript φ indicates a fluid phase and subscript *k* indicates a chemical species. Also, S is the phase saturation, ρ_{φ} is the phase density, ϕ is the porous medium porosity and $C_{\varphi k}$ is mass fraction of chemical species *k* in phase φ. Also, the global conservation of phases and phases compositions implies that:

$$\sum_{\varphi} S_{\varphi} = 1 \ (phase\ \varphi), \qquad \text{Eq. 1-3}$$

$$\sum_{k} C_{\varphi k} = 1 \ (species\ k\ \in phase\ \varphi).$$ Eq. 1-4

The rate of change of mass for the considered phases and species in a control volume element yields as many continuity (or conservation laws) equations. Considering advection, diffusion, dispersion and production/injection of phases and species carried within those phases, the equation in the local-scale (Darcy-scale) and for each species (*k*), the conservation of the mass fraction $C_{\varphi k}$ reads:

$$\frac{\partial}{\partial t}\left(\phi \sum_{\varphi} \rho_{\varphi} S_{\varphi} C_{\varphi k}\right) + \nabla.\left(\sum_{\varphi} \rho_{\varphi} C_{\varphi k} \boldsymbol{u}_{\varphi} + \boldsymbol{J}_{\varphi k}\right) + \left(\rho_{\varphi} C_{\varphi k} \dot{Q}_{\varphi}\right) = 0,$$ Eq. 1-5

where $\boldsymbol{u}_{\varphi}$ is the Darcy velocity of phase φ (described in Eq. 1-1), and $\dot{Q}_{\varphi}$ is the source term (volumetric injection/production rate). Eq. 1-5 is already an up-scaled model from pore-scale (micro-scale) to local-scale (Darcy-scale), see Figure 1-4. Also, $\boldsymbol{J}_{\varphi k}$ is the diffusive mass flux of species *k* in phase φ, writes as:

$$\boldsymbol{J}_{\varphi k} = -\rho_{\varphi}\left(\phi\, S_{\varphi} \boldsymbol{D}_{k\varphi} + \beta \left\|\boldsymbol{u}_{\varphi}\right\|\right) \nabla C_{\varphi k},$$ Eq. 1-6

where $\boldsymbol{D}_{k\varphi}$ is the molecular diffusion coefficient, (which is roughly assumed as a diagonal tensor) and β is the dispersivity of the medium.

Also, in a multiphase generalized Darcy framework the difference in pressure between two phases is called capillary pressure. In the case of two-phase flow involving water and NAPL (i.e., oil), it writes $P_c(S_w) = P_o - P_w$. In addition to being physical properties, mathematically speaking, capillary pressure relationships, which couple pressures P_{φ} through saturations S_{φ}, are closure relationships, in addition to saturation and composition relationships Eq. 1-3 and Eq. 1-4, for the system of Eq. 1-5 and Eq. 1-1. This additional driving (or trapping) force is developed in chapter 3. But before that, we should present the simple single-phase case where most of up-scaling approaches are developed.

1.1.5 Single-phase pressure flow in porous media at Darcy-scale

For this part of the study, we consider only the pressure gradient in the matrix block for single-phase flow ($S_{\varphi} = 1$), and we separate the diffusion-dispersion and the source term ($\dot{Q}$) per unit

bulk volume of reservoir. Besides, we consider that the fluid contains a single species. Substituting the Darcy velocity Eq. 1-1 into Eq. 1-5 gives a Partial Differential Equation as:

$$\frac{\partial}{\partial t}\,(\rho\phi) - \boldsymbol{\nabla}\cdot\left[\rho\frac{k}{\mu}(\boldsymbol{\nabla}P - \rho\boldsymbol{g})\right] = 0. \qquad \text{Eq. 1-7}$$

We can simplify the above equation by redefining pressure as $P \pm \rho g z$ (depending on z-coordinate downward/upward orientation), which is acceptable for an incompressible fluid.

One can further simplify by assuming constant permeability and viscosity:

$$\rho\frac{\partial\phi}{\partial t} + \phi\frac{\partial\rho}{\partial t} - \frac{k}{\mu}[(\boldsymbol{\nabla}\rho)\cdot(\boldsymbol{\nabla}P) + \rho\Delta P] = 0. \qquad \text{Eq. 1-8}$$

Defining the isothermal fluid and rock compressibility relations and the pressure gradient as:

$$\begin{cases} c_{fluid} = \dfrac{1}{\rho}\left(\dfrac{\partial\rho}{\partial P}\right)_T \\ c_{rock} = \dfrac{1}{\phi}\left(\dfrac{\partial\phi}{\partial P}\right)_T \end{cases}, \qquad \text{Eq. 1-9}$$

where c_{fluid} is the isothermal fluid compressibility and c_{rock} is the isothermal rock compressibility. Substituting the expressions of Eq. 1-9 into equation Eq. 1-8 gives:

$$\rho\phi\,\underbrace{(c_{fluid} + c_{rock})}_{c_t}\frac{\partial P}{\partial t} - \rho\frac{k}{\mu}\,(c_f|\boldsymbol{\nabla}P|^2 + \Delta P) = 0, \qquad \text{Eq. 1-10}$$

where c_t is total compressibility. c_{rock} is typically in the range 4 to $8\times10^{-5}\,\frac{1}{bar}$ and c_{water} is about $4.3\times10^{-5}\,\frac{1}{bar}$, which gives a total compressibility of $\sim10^{-4}\,\frac{1}{bar}$ in our model.

The quadratic pressure gradient term can be neglected for low-compressibility fluids so that Eq. 1-10 can be simplified to:

$$\phi c_t\,\frac{\partial P}{\partial t} = \frac{k}{\mu}\,\Delta P. \qquad \text{Eq. 1-11}$$

Eq. 1-11 describes a single-phase pressure diffusion in a porous media at Darcy scale. Later, we use this equation to model linear diffusion in matrix-fracture transfer condition.

1.1.6 Up-scaling fractured porous media

Different modeling approaches describe how the behavior of the system at the local-scale (Darcy equation) is again up-scaled to the macro-scale reservoir simulations. This process also demands up-scaling of matrix-fracture flux in single-phase and two-phase diffusion transfer at the block-scale.

Discrete Fracture Network (DFN) and **Dual-Medium** (so-called dual-porosity) models are two common approaches used to simulate the flow in fractured systems. The discrete fracture network model explicitly simulates the fluid flow in each fracture and the matrix using Darcy's law. Provided that a reliable characterization of the naturally fractured reservoir under consideration is available, flow simulation with a DFN model is accurate but extremely expensive and time-consuming. Previously, the use of DFN was limited both by our ability to describe fractured reservoir accurately and by the computational cost involved in flow simulation. Advanced characterization tools and software are now able to provide realistic realizations of fracture networks. This, combined with increased computing capabilities, enables DFN simulations in some cases. However, the use of DFNs for flow modeling at the field scale is still computationally demanding, especially when the displacement mechanism is complex, and various flow scenarios must be considered. In this study we rather focus on the dual-medium model.

These challenges inspired an effective dual-medium model, which can be very fast and reliable as long as the equivalent averaged parameters are available. However, it suffers from limiting approximations for multiphase flow, as we will show later. It was introduced first in the 1960s and still is the most common method to simulate fluid flow within the fractured reservoirs. (Pirson, 1953) introduced the concept of separating two porosity-permeability systems for the first time. He considered two porosity-permeability relations for porous media grains and for pores spaces of the fractures and fissures. By that, he explained the production performance of fractured reservoirs.

(Barenblatt et al., 1960) introduced an early dual-medium up-scaling model for single-phase condition. They distinguished, at the pore-scale, two systems of pores in a fractured porous medium; the fractures occupy a much smaller volume in comparison with the pores of the matrix. A first up-scaling within the fracture and the matrix leads to a Darcy-scale

description of the fracture-matrix system. The following system of equations describes pressure diffusion transfer (Eq. 1-11) in matrix and fracture region separately:

$$\begin{cases} c_f \dfrac{\partial}{\partial t} P_f = \boldsymbol{\nabla}.\left(\dfrac{\mathbf{k}_f}{\mu}.\boldsymbol{\nabla} P_f\right) & in\ \Omega_f \\ \boldsymbol{n}_{fm}.\left(\mathbf{k}_f.\boldsymbol{\nabla} P_f\right) = \boldsymbol{n}_{fm}.\left(\mathbf{k}_m.\boldsymbol{\nabla} P_m\right) & on\ \Gamma_{mf}, \\ P_f = P_m & on\ \Gamma_{mf} \\ \phi_m c_m \dfrac{\partial}{\partial t} P_m = \boldsymbol{\nabla}.\left(\dfrac{\mathbf{k}_m}{\mu}.\boldsymbol{\nabla} P_m\right) & in\ \Omega_m \end{cases} \qquad \text{Eq. 1-12}$$

where, P_f and P_m represent the local pressure, $\boldsymbol{n}_{fm}$ is the vector normal to fracture-matrix interface (Γ_{mf}). The subscripts refer to the properties in matrix and fracture medium respectively. Even starting with an isotropic scalar permeability at Darcy-scale, the anisotropy of fracture system can produce permeability tensors for matrix and fracture system. However, this aspect of the fractured porous media is out of the scope of this study, and we assume a scalar as averaged permeability tensor (k_f, k_m) time the identity tensor for both regions. The properties need to be up-scaled to this dual-medium scale.

At this scale (Eq. 1-12), fracture and matrix are still spatially discriminated, and the permeability of the fracture network is considerably larger than the permeability within individual porous blocks. A further up-scaling can be undertaken for a large-scale representative elementary volume (REV) containing fracture media and matrix media. Because of the relaxation time necessary to homogenize flow field properties within a REV, it is convenient to introduce a two- or dual-medium large-scale description. At a given point in the large-scale description are associated two large-scale liquid pressures, $\bar{P}_m$ and $\bar{P}_f$. The fracture pressure ($\bar{P}_f$) represents the average pressure of the fluid in the fractures held in that element, while matrix pressure ($\bar{P}_m$) is the average pressure of the fluid in the matrix pores. A large-scale velocity is also defined. Combining large-scale mass and momentum balances for each large-scale continua, we can write two equations for $\bar{P}_f$ and $\bar{P}_m$, which feature a mass exchange term connecting the two media. Two conservation equations can be written for the single-phase fluid in unit-volume of the dual-medium to link the average pressures of the fracture and matrix media:

$$\phi_f \rho c_f \frac{\partial \bar{P}_f}{\partial t} = \boldsymbol{\nabla}.\left[\frac{\rho k_f}{\mu}\boldsymbol{\nabla}\bar{P}_f\right] + \Phi_{mf}, \qquad \text{Eq. 1-13}$$

$$\phi_m \rho c_m \frac{\partial \bar{P}_m}{\partial t} = \boldsymbol{\nabla}.\left[\frac{\rho k_m}{\mu}\boldsymbol{\nabla}\bar{P}_m\right] - \Phi_{mf}, \qquad \text{Eq. 1-14}$$

where, Φ_{mf} is the fluid mass transfer (so-called flux in this study) per volume [M/(TL^3)] from the matrix region to the fracture region. c_m and c_f are the total compressibilities in the matrix and the fracture regions respectively, and k_f and k_m represent the average permeabilities in fracture and matrix regions. Note that if viscous flow does not happen in the matrix block (as explained in 1.1.2) we can neglect the first right hand side term in Eq. 1-14.

The study by (Warren & Root, 1963) was one of the first attempts to characterize the flow behavior of a fractured medium from well test analysis. These authors analyzed pressure build-up data to determine parameters that quantify fracture flow and (matrix-fracture) inter-porosity flow. Their objective was to present a model that accounts for the single-phase flow behavior of a formation with two porosities. The dual-medium model, in their investigation, is based on the following general assumptions:

- The material containing the primary porosity is homogeneous and isotropic and is contained within a systematic array of identical, rectangular parallelepipeds.
- Matrix blocks are fluid containers, and their properties are averaged to be only connected to fractures (no connection between matrix blocks).
- All the secondary porosity is contained within an orthogonal system of continuous and uniform fractures, which are oriented so that each fracture is parallel to one of the principal axes of permeability; the fractures normal to each of the principal axes are uniformly spaced and are of constant width; the permeability may however differ from one principal axis of permeability to another to consider different fracture spacing and/or apertures.

Figure 1-5 shows the idealized representation of a fractured reservoir in dual-medium models. This classical model faces several questionings of its validity:

- The concept of equivalent block: is a sugar cube block a good representative of an irregular block with non-homogeneous fractures?
- Does this form of approximation model the exact exchange between matrix and fractures?
- How accurate is the approximation for the equivalent properties such as effective fracture permeability?

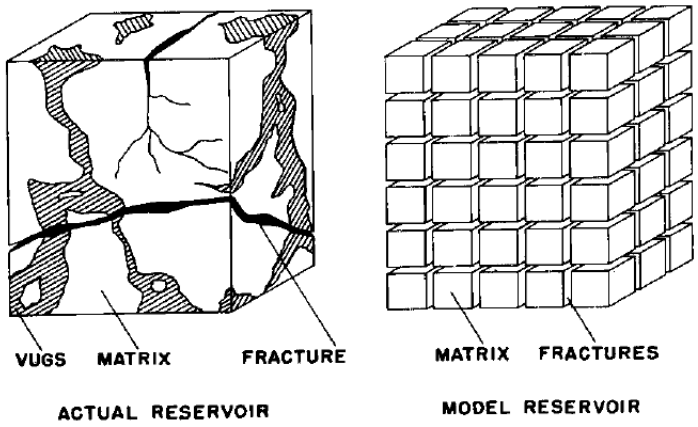


Figure 1-5 Classical representation of a 3D fractured matrix block (left) with the equivalent dual-medium model (right) known as sugar cube model (Warren & Root, 1963).

Warren and Root modeled the dynamic response of a fractured reservoir by considering two interacting continua with contrasted flow properties as a homogenized matrix and homogenized fracture medium like a sugar cube. They suggested an inter-porosity transfer condition with an underlying Darcy-description to model the flux between homogenized matrix medium and homogenized fracture medium at the macro-scale by the following relation:

$$\Phi_{mf} = \sigma \frac{\rho k_m}{\mu} \left(\bar{P}_f - \bar{P}_m \right), \qquad \text{Eq. 1-15}$$

in which, σ [1/L^2] is a shape factor that has to be evaluated. Eq. 1-15 expresses an approximation for matrix-fracture flux using averaged properties. Generally, several effective properties appear in these equations (Eq. 1-13 – 1-15), in particular: a (large-scale) fracture effective permeability (k_f), and a coefficient that was suggested to model fluid transfer between the blocks and fractures continua (Quintard & Whitaker, 1996). In fact, describing the exchange between the fractures through a single parameter is not obvious, for mathematical reasons that will be underlined later, which explains why the characterization of this matrix-fracture fluid transfer equation has become one of the main questions in fractured reservoir modeling.

Otherwise, we can express the matrix/fracture flux with Darcy-scale considerations of the fluid mass conservation equation for the matrix block. The matrix/fracture flux can be obtained from the fluid mass fluctuation in the matrix domain (from Eq. 1-12), which reformulates after the use of Green's formula:

$$\Phi_{mf} = \frac{1}{|\Omega_m|}\int_{\partial\Omega_m} \frac{\rho \mathbf{k}_m}{\mu}.\boldsymbol{\nabla} P_m d\Gamma, \qquad \text{Eq. 1-16}$$

where Ω_m denotes the matrix block, $|\Omega_m|$ its volume, P_m the local pressure inside this block, dΓ is an infinitesimal (surface) element of Ω_m. The density vanishes if Φ_{mf} is considered as fluid volume transfer, which has a dimension of [L/T, L^2/T, L^3/T] for 1D to 3D respectively.

Back to the dual-medium context, the matrix and fracture medium refer to the homogenized matrix and the homogenized fracture medium. Eq. 1-15 is a so-called "**inter-porosity flux"**. This transfer equation also involves a geometric factor σ, well-known as the "**shape factor**", to only take into account the impact of matrix blocks shape and size on transfer. From analytical derivations, Warren and Root gave the following approximation of σ:

$$\sigma = \frac{4N(N+2)}{L^2}, \qquad \text{Eq. 1-17}$$

where *N* is the number of parallel fracture sets (1, 2, or 3) with a fracture spacing of *L* in related directions. For three sets of fracture (see Figure 1-5), Eq. 1-17 yields $\sigma = 60/L^2$. More literature on approximation of the shape factor is given in section 2.5.

Dual medium models with constant shape factor have an advantage: their relative simplicity. In most cases, for both analytical and numerical models, once the single porosity model is available, getting the corresponding dual porosity model with constant shape factor is quite easy (Kazemi et al., 1976; Swaan O., 1976). Such models are characterized by a single characteristic time (typically the overall diffusion time over one matrix block) on a characteristic length of the matrix blocks.

By construction, inter-porosity models with constant shape factor possess several limitations: they cannot capture short time effects, such as diffusive boundary layer effects that may be dominant at short times (they are observed in case of very tight medium, involved in geothermal recovery resources, or for gas recovery in fractured tight rocks (Kucuk & Sawyer, 1980; Ran, 2020; Wei et al., 2022; Zhang et al., 2016). In that situation, the relevant quantity is the surface to volume ratio of the fracture network. In addition, the dual-medium models are not capable of capturing the effect of the block size heterogeneity.

To overcome those limitations, several authors investigated different approaches. In order to capture short-time effects, relaxing the instantaneous flux condition using transient dual-porosity models was proposed. Considering problems driven by a linear diffusion equation, the exchange flux can be written under the form of a time convolution of the matrix/fracture potential difference with a time-dependent kernel that corresponds to the solution of a well-defined boundary value evolution problem (Barenblatt et al., 1960; Landereau et al., 2001b; Landereau et al., 2001a; Swaan & Ramirez-Villa, 1993). That convolution form respects both linearity and causality of the system and is thus valid even if the overall forcing terms are time-dependent. In practice, for applications to purely diffusive problems such as pumping tests, that kernel may be computed by means of Continuous Time Random Walk methods that are very efficient (Noetinger et al., 2001; Noetinger et al., 2016; Noetinger & Estebnet, 2000). For pumping tests, complete analytical solutions are available considering simple matrix block shapes such as layers or spherical blocks. They are encoded in commercial pumping tests (pressure transient analysis) software.

When considering applications to problems where advection in the fractures may be one of the dominant transport processes, other strategies were investigated: to capture short time effects, (Zimmerman et al., 1993) proposed to change the analytical form of the exchange term, selecting an ad-hoc non-linear form. Such approaches work well if the forcing boundary conditions are not changing, because there is an ambiguity in the definition of the starting time (time invariance is lost). Other models avoid the tedious convolution by considering multiple porosity models (Landereau et al., 2001a): in which each porosity is coupled to the fracture network only. Such models are shown to converge very slowly especially at short times.

Other approaches proposed to use Multiple Interacting Continua (MINC) (Al-Rudaini et al., 2020; Bourbiaux & Ding, 2016; Narasimhan & Pruess, 1988; Pruess & Narasimhan, 1985; Saidi, 1983) in which matrix blocks are discretized as unidimensional media as shown in Figure 1-6. The resulting model corresponds to “in series” porosity that are coupled to each other, the last one being coupled to the fracture network and gathering the contributions of all the others.

(Babey et al., 2015) considered a general case where both approaches are mixed. Another set of approaches are the so called Multiple rate transfer models (Haggerty & Gorelick, 1995). The fractional derivatives tool of (Raghavan, 2011) is another particular way to condense the convolution approach.

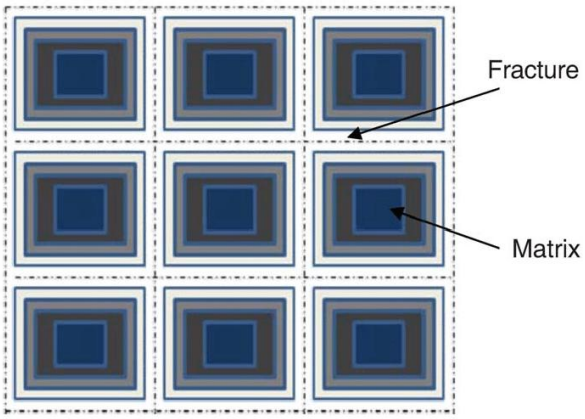


Figure 1-6 scheme of MINC sub-gridding method to capture the transient transfer inside the matrix blocks (after Pruess & Narasimhan, 1985).

In summary, several approaches are proposed to overcome the limitations of the steady state dual porosity approach. For applications, the choice depends on the problem at hand, and if one is interested in capturing early-time effects, or late-time effects. Most approaches resolve the up-scaling problem for simplified single-phase condition, where more exact solutions are available. For non-linear problems such as multiphase flow, to our knowledge, no well documented solution exists, and one still relies on ad hoc models. All these brief characterizations of the fractured reservoirs and the lack of specific simulation of complex two-phase transfers in dual-porosity models encouraged us to initiate this research study for both single-phase and two-phase diffusive transfer mechanisms.

1.2 Objectives of the Ph.D. project

Transfers in fractured porous media are key processes in many industrial applications such as water management, oil production, geothermal exploitation, soil remediation or geological storage. The main application for geosciences of fluid dynamics in fractured porous media is the simulation of the best realistic models for single- or two-phase flow such as producing a matrix block saturated by NAPL. The objective of this Ph.D. research is to increase the reliability of up-scaling of matrix-fracture inter-porosity flux in a two-phase capillary imbibition transfer, which is useful to simulate fluid transport at the scale of reservoir blocks. Parameterizing such models remains an unsolved issue when multiphase and simultaneous transfers must be simulated.

We model the fractured reservoirs through the dual-medium approach with matrix-fracture connections. Previous studies have extensively investigated the up-scaling of the

geological parameters and the matrix-fracture transfer homogenization in single phase flow. However, very soon after the start of exploitation, the production from fractured reservoirs becomes multiphase, and modeling complicated two-phase transfer mechanisms in dual-medium system is still a matter of research. One of the tough challenges for all researchers in this domain is to evaluate and improve the accuracy of dual-medium simulators in predicting matrix-fracture transfers. Specifically, as we will see in chapter 2, even in the simplest monophasic case, the shape factor (an equivalent dynamical parameter that results from the dual-medium averaging process as we will show later) that is used to compute fracture-matrix transfers is time-dependent. Therefore, the use of a constant shape factor, as it is done in most multiphase flow reservoir simulators, does not accurately capture the transient regime of block imbibition. DFN models will not be considered in our work. However, analytical models or fine grid numerical solutions will be used to provide references, i.e., quasi-exact, solutions for validation purposes in chapters 2 and 3.

Flow or mass transfer up-scaling issue is inherent to dual-medium reservoir models for two main reasons. Firstly, the actual geological fracture network is not modeled accurately but simulated via an equivalent permeability tensor. Secondly, matrix blocks are not sub-gridded and the transfers into the matrix porosity are simulated at the scale of reservoir matrix blocks using up-scaled properties (see Figure 1-4). This matrix-fracture flux up-scaling issue is emphasized in oil recovery processes involving multiple transfer mechanisms. The distribution of matrix blocks size and shape at the scale of a coarse reservoir model cell adds more difficulty in that up-scaling issue.

While the main focus is on the two-phase capillary diffusion, the molecular diffusion in single-phase transfer is worth investigating. That can be the main mechanism to transfer a chemical into the matrix blocks in fractured carbonate reservoirs. Carbonate reservoirs are often oil-wet and that leaves a high residual oil saturation in the matrix blocks. Therefore, in such reservoirs, the aqueous phase does not imbibe into the matrix medium spontaneously at low saturation levels. The use of chemical molecular diffusion was also motivated by the fact that molecular diffusion is an ever-acting mechanism that transfers chemical additives into oil-wet matrix blocks, with possible rock wettability alteration giving rise to capillary imbibition.

The main objective of this study is to model the well-known single-phase transfer in matrix-fracture flux of dual-medium models and to adapt a flux calculation technique for capillary imbibition as the main two-phase transfer.

1.3 Methods, tools, data

As mentioned, the dual-medium modeling framework is a powerful tool for addressing transfers in fractured porous media but, unfortunately, most of their formulations rely on the simplified constant value of a so-called "shape factor". This parameter can be derived in a single-phase flow context for several block shapes by resorting to simplifying assumptions in the initial and boundary conditions. The analytical solutions in a simple single-phase flow demonstrate that this shape factor, is obtained from the up-scaling procedure and is not a constant and depends on the transfer mechanism, boundary condition and so on. Although a late-time steady-state shape factor is most often adopted for practical purposes, that choice may lead to errors in the flow and transfers calculation for the transient regime. The question of the computation of that shape factor and its time dependency is still open regarding multiphase compositional flows and transfer mechanisms such as those described in the previous sections. In this context, it is worth noting practical techniques have been implemented by engineers, such as empirical pseudoization of flow properties (such as relative permeabilities and capillary pressures), which is matching a dual-medium simulation over a reference, unbiased, single-medium one. This type of approach has the disadvantage of having to be carried out on a case-by-case basis each time. These modifications are effortful, especially when dealing with heterogeneous media for which those are subject to rock-typing and several up-scaling.

Rather than resorting to this type of approach, this thesis tries to find more predictive formulations using analytical and semi-analytical solutions to model both transient and steady-state matrix-fracture transfers in single-phase and two-phase diffusive transfers. We investigate three types of diffusive transfer in fractured porous media: single-phase pressure diffusion and molecular diffusion assuming constant diffusion coefficient and two-phase capillary imbibition with highly non-linear diffusion function.

To do this, the pressure diffusivity equation is developed for porous media at the beginning of **chapter 2** and a specific analytical solution for one-dimensional flow under constant fracture boundary condition is proposed. The molecular diffusion process shows the same problem with a different scale of diffusion time. The solution divides transfer time into early-times and late-times. Dual-medium model is developed and both solutions of analytical and numerical types are derived and compared. The calculation determines an analytical shape

factor formulation, which is compared with the available literature studies at the end of this chapter.

In the single-phase diffusion where an analytical solution is available, IFP Energies nouvelles reservoir simulator "PumaFlow" is used in single-porosity version to reproduce the reference solutions on finely-gridded (i.e. local-scale) matrix block models, then in its dual-porosity version to simulate the equivalent up-scaled matrix-fracture flux scenario. The simulator's results are consistent with these up-scaling methods. These initial steps help to set up and validate the up-scaling methodology before undertaking the study of the more complicated transfers. This chapter indicates that a challenge lies in different transfer behaviors at early times and late times because of the finite size of matrix blocks.

In **chapter 3**, we consider capillarity as a driving force in porous media where the rock surface has different tendency to the water phase (water-wet or non-water-wet). Indeed, capillary pressure is a critical parameter for non-water-wet porous media, as it traps NAPL in matrix blocks and inhibits matrix-blocks imbibition by water. We revisit this driving force as a non-linear diffusion phenomenon in fractured porous media by presenting two exact asymptotic solutions valid for short and long times. The best choice of parameter for those analytical solutions is discussed in detail. Generalization of the proposed approach to two- and three-dimensional models is presented under a few assumptions. The solution allows to adapt dual-porosity models to two-phase flows following a rigorous workflow. The solution and scaling-up of two-phase capillary imbibition in a dual-medium framework is precisely the core of this thesis.

In the two-phase condition the partial differential equation is non-linear with singularities at the boundaries and it was difficult to be simulated by a regular simulator (like PumaFlow). Therefore, a specific numerical prototype (written with Scilab) is used to model transfer in one- and two-dimensional cases. Another open-source finite element solver, FreeFEM is used to solve a partial differential equation in any arbitrary domain. The latest has the advantage of solving one of the Ph.D. problems on any arbitrary domain.

Regarding model data input, 1D flow properties in the single- and two-phase conditions are usually measured on matrix medium cores in the laboratory. We have selected some ordinary rock and fluid properties based on experiments or available models.

1.4 References

Al-Rudaini, A., Geiger, S., Mackay, E., Maier, & Pola, J. (2020). Comparison of Chemical-Component Transport in Naturally Fractured Reservoirs Using Dual-Porosity and Multiple-Interacting-Continua Models. *SPE Journal*, *25*(4), Article SPE-195448-PA.

Babey, T., Dreuzy, J.‐R. de, & Casenave, C. (2015). Multi-Rate Mass Transfer (MRMT) models for general diffusive porosity structures. *Advances in Water Resources*, *76*, 146–156.

Barenblatt, G. I., Zheltov, I. P., & Kochina, I. N. (1960). Basic Concepts in The Theory of Seepage of Homogeneous Liquids in Fissured Rocks. *PMM*, *24*(5), 852–864.

Bourbiaux, B., Basquet, R., Cacas, M. C., Daniel, J. M., & Sarda, S. (Eds.) (2003). *An Integrated Workflow to Account for Multi-Scale Fractures in Reservoir Simulation Models: Implementation and Benefits*.

Bourbiaux, B., & Ding, D. (2016). Simulation of Transient Matrix-Fracture Transfers of Compressible Fluids. *Transport in Porous Media*, *114*(3), 695–717. https://doi.org/10.1007/s11242-016-0740-9

Burchette, T. P. (2012). Carbonate rocks and petroleum reservoirs: a geological perspective from the industry. In J. Garland, J. E. Neilson, S. E. Laubach, & K. J. Whidden (Eds.), *Advances in Carbonate Exploration and Reservoir Analysis* (Vol. 370, p. 0). Geological Society of London. https://doi.org/10.1144/SP370.14

Darcy, H. (1856). *Les Fontaines publiques de la ville de Dijon ; Exposition et application des principes à suivre et des formules à employer dans les questions de distribution d'eau*. V. Dalmont.

Haggerty, R., & Gorelick, S. M. (1995). Multiple-Rate Mass Transfer for Modeling Diffusion and Surface Reactions in Media with Pore-Scale Heterogeneity. *Water Resources Research*, *31*(10), 2383–2400. https://doi.org/10.1029/95WR10583

Kazemi, H., Merrill, L. S., & Zeman, P. A. (1976). Numerical Simulation of Water-Oil Flow in Naturally Fractured Reservoirs. *SPE Journal*, *16*(6), Article 5719, 317–326.

Kucuk, F., & Sawyer, W. K. (1980). Transient Flow In Naturally Fractured Reservoirs And Its Application To Devonian Gas Shales. In *SPE Annual Technical Conference and Exhibition*.

Landereau, P., Noetinger, B., & Quintard, M. (2001). Quasi-steady two-equation models for diffusive transport in fractured porous media: large-scale properties for densely fractured systems. *Advances in Water Resources*, *24*(8), 863–876.

fractured systems. *Advances in Water Resources*, *24*, 863–876.

Narasimhan, T. N., & Pruess, K. (1988). MINC: An Approach for Analyzing Transport in Strongly Heterogeneous Systems. In E. Custodio, A. Gurgui, & J. P. L. Ferreira (Eds.), *Groundwater Flow and Quality Modelling* (pp. 375–391). Springer Netherlands. https://doi.org/10.1007/978-94-009-2889-3_21

Noetinger, B., Estebenet, T., & Landereau, P. (2001). A direct determination of the transient exchange term of fractured media using a continuous time random walk method. *Transport in Porous Media*, *44*(3), 539–557.

Noetinger, B., & Estebnet, T. (2000). Up-scaling of double porosity fractured media using continuous-time random walks methods. *Transport in Porous Media*, *39*(3), 315–337.

Noetinger, B., Roubinet, D., Russian, A., Le Borgne, T., Delay, F., Dentz, M., Dreuzy, J.‐R. de, & Gouze, P. (2016). Random walk methods for modeling hydrodynamic transport in porous and fractured media from pore to reservoir scale. *Transport in Porous Media*, *115*(2), 345–385.

Pirson, S. J. (1953). Performance of Fractured Oil Reservoirs. *Bulletin of the American Association of Petroleum Geologists*, *37*(2), 232–244.

Pruess, K., & Narasimhan, T. N. (1985). A Practical Methd for Modeling Fluid and Heat Flow in Fractured Porous Media. *SPE Journal*, *25*, Article SPE-10509-PA, 14–26.

Quintard, M., & Whitaker, S. (1996). Transport in Chemically and Mechanically Heterogeneous Porous Media I: Theoretical Development of Region-Averaged Equations for Slightly Compressible Single-Phase Flow. *Advances in Water Resources*, *19*, Article 0309-1708(95)00023-C, 29–47.

Raghavan, R. (2011). Fractional derivatives: Application to transient flow. *Journal of Petroleum Science and Engineering*, *80*(1), 7–13. https://doi.org/10.1016/j.petrol.2011.10.003

Ran, Q. (2020). Flow and Recovery Mechanisms in Tight Oil and Gas Reservoirs. In Q. Ran (Ed.), *Unconventional Tight Reservoir Simulation: Theory, Technology and Practice* (pp. 35–70). Springer Singapore. https://doi.org/10.1007/978-981-32-9848-4_2

Reis, J. C. (Ed.) (1990). *Oil Recovery Mechanisms in Fractured Reservoirs During Steam Injection*.

Reiss, L. H. (1980). *The Reservoir Eengineering Aspects of Fractured Formations*. technip.

Saidi, A. M. (Ed.) (1983). *Simulation of Naturally Fractured Reservoirs*.

Slattery, J. C. (1967). Flow of viscoelastic fluids through porous media. *AIChE Journal*, *13*(6).

Swaan, A. de, & Ramirez-Villa, M. (1993). Functions of flow from porous rock blocks. *Journal of Petroleum Science and Engineering*, *9*(1), 39–48. https://doi.org/10.1016/0920-4105(93)90027-C

Swaan O., A. de (1976). Analytic Solutions for Determining Naturally Fractured Reservoir Properties by Well Testing. *SPE Journal*, *16*(03), 117–122. https://doi.org/10.2118/5346-PA

Warren, J. E., & Root, P. J. (1963). The Behavior of Naturally Fractured Reservoirs. *SPE Journal*, *3*, 245–255. https://doi.org/10.2118/426-PA

Wei, C., Liu, Y., Deng, Y., Cheng, S., & Hassanzadeh, H. (2022). Temperature Transient Analysis of Naturally Fractured Geothermal Reservoirs. *SPE Journal*, 1–23. https://doi.org/10.2118/205862-PA

Whitaker, S. (1967). Diffusion and dispersion in porous media. *AIChE Journal*, *13*(3).

Zhang, R., Zhang, L., Wang, R., Zhao, Y., & Zhang, D. (2016). Research on transient flow theory of a multiple fractured horizontal well in a composite shale gas reservoir based on the finite-element method. *Journal of Natural Gas Science and Engineering*, *33*, 587–598. https://doi.org/10.1016/j.jngse.2016.05.065

Zimmerman, R. W., Chen, G., Hadgu, T., & Bodvarsonn, G. S. (1993). A numerical dual-porosity model with semianalytical treatment of fracture/matrix flow. *Water Resources Research*, *29*(7), 2127–2137.

2 Single-phase Diffusion Transfer in Fractured Porous Media

This chapter outlines the fluid flow modeling in a simple fractured porous medium and introduces an up-scaling solution based on some matrix-fracture assumptions. This single-phase transfer as a linear diffusion problem includes viscous flow (pressure diffusivity) and molecular diffusion with constant diffusion coefficients. The diffusivities in these two transfers differ by several orders of magnitude. The chapter develops analytical and numerical solutions for a one-dimensional flow with a particular initial boundary value problem, where a matrix block is surrounded by a fracture with constant pressure/concentration. The analytical solution is compared with both fine-grid and dual-medium numerical simulations.

The dual-medium transfer model, as the basis of the study, is addressed in detail. The results show the need for considering early-time transient behaviour and coupling a time dependent shape factor for the dual-medium model. Finally, an analytical approximation in terms of the averaged unknown under consideration is obtained to improve the dual-medium model.

The chapter ends with a literature review on different solutions of inter-porosity shape factor and an analytical approximation to up-scaling single-phase matrix-fracture diffusion in section 2.5 and 2.7 respectively.

2.1 Pressure diffusion (viscous flow) in the matrix block

This transfer mechanism is developed in the previous chapter (Eq. 1-2 – 1-11), where we can rearrange Eq.1-11 as:

$$\frac{\partial P}{\partial t} = \underbrace{\frac{k}{\phi \mu c_t}}_{\eta\ (diffusivity)} \Delta P, \qquad \text{Eq. 2-1}$$

where, the coefficient η is the pressure diffusivity. The solution to this partial differential equation depends on the initial and boundary conditions that must be specified. Considering a permeability of 10 to 100 md, with a porosity of 0.05 to 0.2 and a fluid dynamic viscosity of 1 $mPa.s$, pressure diffusivity has a typical range of 1 to $20 \times 10^{-4}\,\frac{m^2}{s}$.

2.2 Molecular diffusion in the matrix block

Diffusion is the transport process from regions of large concentration of a system to regions of lesser concentration due to random molecular motions. Transfer of heat by conduction is also due to random molecular motions, and there is an obvious analogy between the two processes, which was represented by (Fick, 1855) for the first time. In fact, the topic of analogy stated that temperature, pressure, and concentration gradients, provide the driving potential for heat, momentum, and solute mass transfer, respectively. The mathematical theory of diffusion in isotropic substances is therefore based on the hypothesis that the rate of transfer of diffusing substance through the unit area of a section is proportional to the concentration gradient measured normal to the section area, i.e.

$$F = -D\nabla C, \qquad \text{Eq. 2-2}$$

where, F is the rate of transfer per unit area of the section [*amount of substance*/L^2/T], C is the concentration [*amount of substance*/L^3] of the diffusing substance, x is the space coordinate measured normal to the section, and D is called the diffusion coefficient with a dimension of [L^2/T]. Simplifying, in some cases, e.g. diffusion in dilute solutions, D can reasonably be taken as constant, while in others, e.g., diffusion in polymers, it is a function of concentration (Reis et al., 2001). In an aqueous solution, typical diffusion coefficients for solutes are in the range of $\sim 10^{-9}$ to 10^{-11} $\frac{m^2}{s}$.

The fundamental differential equation of diffusion is derived in similar steps for pressure diffusion, by writing the mass conservation equation in one dimension, for an element with a constant diffusion coefficient and using Fick's law instead of Darcy's law:

$$\frac{\partial C}{\partial t} = D\Delta C. \qquad \text{Eq. 2-3}$$

Assuming a constant D, Eq. 2-3 is also a linear PDE. This time-dependent equation can be solved analytically based on initial and boundary conditions. Besides, a comprehensive study on analytical solutions of diffusion systems with various boundary conditions is proposed by (Crank, 1975).

Molecular diffusion in the fluid saturating the pores of a porous medium is a slower mechanism than free diffusion in the fluid in bulk. The impact of porous medium characteristics, like available cross-section area for diffusion and diffusion paths lengths, is considered by an **effective diffusion coefficient, $\boldsymbol{D_{eff}}$**. Different analytical formulas based on porous media properties were established to determine D_{eff} from experimental diffusion data (Weissberg, 1963). They will not be reviewed herein. Under multiphase flow conditions, phase saturation is assumed to reduce diffusion flux proportionally. The effective diffusion, in a porous medium saturated by a single-phase fluid, is defined as molecular diffusion multiplied by porosity and divided by the tortuosity, that is:

$$D_{eff} = \frac{\phi D}{\tau_s}. \qquad \text{Eq. 2-4}$$

Tortuosity (τ_s) accounts for the differences between diffusion in a porous medium with non-rectilinear and irregular paths for mass transfer and diffusion in a bulk fluid phase. Different parameters such as reaction or phase location within pores (related to wettability) may also impact the tortuosity. Besides many empirical relations for tortuosity (Ghanbarian et al., 2013; Pisani, 2011), a fixed value of 2 (dimensionless) in flow direction was adopted for all the models of this study in this chapter. The final PDE writes

$$\frac{\partial C}{\partial t} = \underbrace{\frac{D_{eff}}{\phi}}_{D^*} \Delta C \qquad \text{Eq. 2-5}$$

Those two problems (Eq. 2-1 and Eq. 2-5) represent a linear form and differ in diffusion coefficient value, where, η is about $\sim 10^{-4}\,\frac{m^2}{s}$, while D^* is in the range of $\sim 10^{-11}\,\frac{m^2}{s}$ in our model. We can continue with any of the linear diffusion unknowns (pressure or concentration even temperature) to get dimensionless analytical solutions.

2.3 Analytical solution of constant fracture condition

Now, we derive analytical solutions for Eq. 2-1 and Eq. 2-5 with Dirichlet boundary conditions on a simple matrix-fracture block. A source of chemical or pressure keeps fracture concentration/pressure at a constant value all the time. These solutions will be useful in the next sections to determine analytical up-scaling matrix-fracture flux.

Let us now consider a fictitious one-dimensional matrix block of linear extension l, whose ends are located at $x = 0$ and $x = l$ and each corresponds to a surrounding fracture. Such a model may be a very first approximation of a large lateral extension block with each face in contact with a fracture, at the local Darcy scale as shown in Figure 1-2. Assuming translational invariance along each of these faces, they can be reduced to 1D point-like interfaces. It is worth noting that the fracture medium is not explicitly described here and is assimilated to boundary conditions. (Carslaw & Jaeger, 1959) solved the one-dimensional diffusivity equation for different initial and boundary conditions. Assuming the matrix block initially at uniform pressure (P_i) and subjected from initial time onwards to another pressure (P_f) applied in the two opposite fractures limiting that block, Eq. 2-1 rewrites as:

$$\frac{\partial P}{\partial t} = \eta \frac{\partial^2 P}{\partial x^2} \qquad \begin{cases} P(x = 0\,, t > 0) = P_f \\ P(x = l\,, t > 0) = P_f \\ P(0 < x < l\,, t = 0) = P_i \end{cases}, \qquad \text{Eq. 2-6}$$

where P_f denote the surrounding uniform fractures pressure, that are assumed to be time independent.

Due to symmetry, one can simulate transfer in half of the block. The full solution writes as the following series expansion:

$$P(x,t) = P_f + \frac{4}{\pi}(P_i - P_f) \sum_0^\infty \frac{1}{2n+1}\, sin\frac{(2n+1)\pi x}{l} e^{-\eta(2n+1)^2\pi^2 t/l^2}. \qquad \text{Eq. 2-7}$$

We can present dimensionless solution by denoting:

$$\tau = \frac{1}{\eta}\left(\frac{l}{\pi}\right)^2. \qquad \text{Eq. 2-8}$$

where, τ is the characteristic time (or relaxation time) that naturally appears in the solutions. And applying a dimensionless unknown of $P_D = (P(x,t) - P_i)/(P_f - P_i)$, one gets:

$$\boxed{P_D(x,t) = 1 - \frac{4}{\pi}\sum_0^\infty \frac{1}{2n+1} sin\frac{(2n+1)\,\pi x}{l} e^{-(2n+1)^2 t/\tau}} \qquad \text{Eq. 2-9}$$

Different methods are proposed to predict the evolution of the **average matrix block pressure** with time. We took a volume average ($\frac{1}{l}\int_0^l P(x,t)\,dx$) over the matrix slab:

$$\bar{P}_D(t) = 1 - \frac{8}{\pi^2}\sum_{0}^{\infty}\frac{1}{(2n+1)^2}e^{-(2n+1)^2 t/\tau} \qquad \text{Eq. 2-10}$$

This solution is valid for molecular diffusion and heat conduction by considering concentration (C) instead of pressure (P) and with a characteristic time of Eq. 2-8 where η is replaced by $D^* = \frac{D}{\tau_s}$.

This equation expresses simplified single-phase, one-dimensional pressure diffusion to the matrix block with initial and boundary conditions of Eq. 2-6. Figure 2-1 illustrates several pressure profiles with dimensionless variables. Because the solution is in the series form, a whole series of relaxations times, that are proportional to τ, controls the average pressure time evolution. Figure 2-2 shows the average pressure plots with different number of series expansion and based on this figure. The solution converges to an acceptable solution with 100 terms of the series expansion where the result does not change (more than 0.1%) even for very low t/τ values.

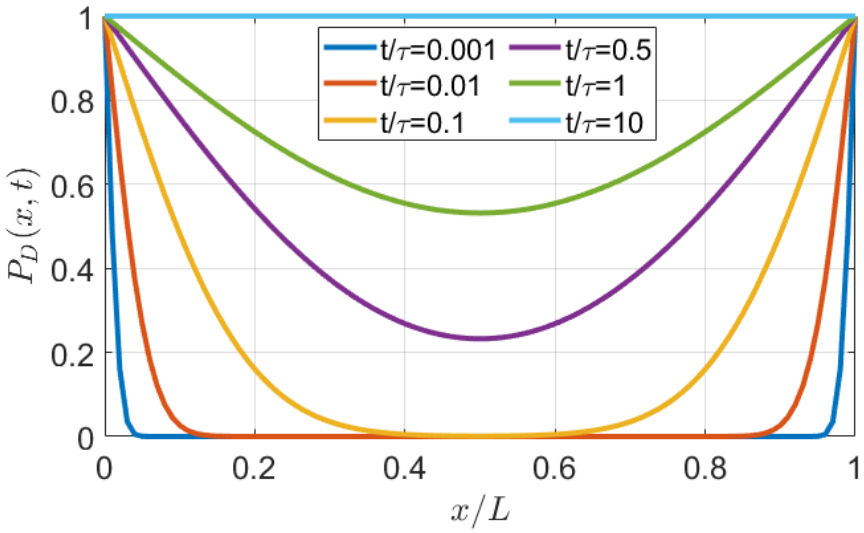


Figure 2-1 Pressure profile of one-dimensional pressure diffusion to the matrix block from both sides for different dimensionless time (t/τ) with $\tau = \frac{1}{\eta}\left(\frac{l}{\pi}\right)^2$.

The following section uses the analytical solution of average pressure to model accurately the inter-porosity flux (presented in Eq. 1-15), which is a classical approximation.

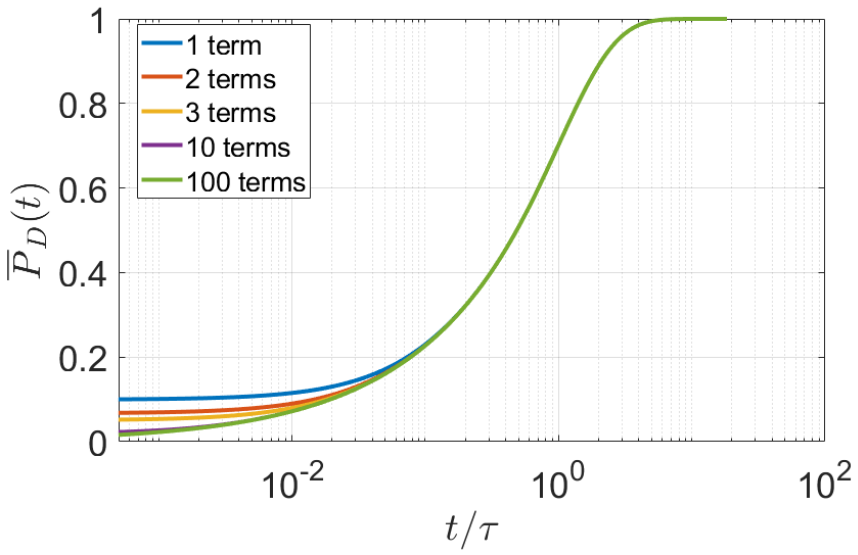


Figure 2-2 Average matrix block pressure of the one-dimensional pressure diffusion versus dimensionless time (t/τ) with $\tau = \frac{1}{\eta}\left(\frac{l}{\pi}\right)^2$.

2.4 Up-scaling the matrix-fracture single-phase flux with dual-medium model

Here, we average the analytical solution of single-phase diffusion with the dual-medium up-scaling approach for this initial boundary value problem. This up-scaling offers a modification with respect to matrix-fracture flux, by presenting a non-linear analytical shape factor.

Using the 1D solution given by Eq. 2-10, the averaged matrix fracture pressure ($\overline{P}_m$) can be substituted in the inter-porosity flux equation Eq. 1-15. We will show hereafter by identification that the shape factor involved in Eq. 1-15 is time dependent. Substituting the analytical solution of matrix average pressure, for our specific initial boundary value problem, gives:

$$\begin{aligned} \Phi_{mf}(t) &= \sigma(t)\frac{k_m}{\mu}(\overline{P}_m(t) - P_f) \\ &= \sigma(t)\frac{k_m}{\mu}\frac{8}{\pi^2}(P_i - P_f)\sum_0^\infty \frac{1}{(2n+1)^2} e^{-(2n+1)^2 t/\tau}, \end{aligned} \qquad \text{Eq. 2-11}$$

where, $\Phi_{mf}(t)$ in a one-dimensional transfer is the volume flow rate per unit volume, which should be multiplied by bulk length to get a total one-dimensional flux [L/T]. And on the other hand, the flow rate resulting from the total compressibility of the matrix block is expressed as:

$$\Phi_{mf}(t) = \phi_m\, c_m \frac{\partial \overline{P}_m(t)}{\partial t} = \frac{k_m}{\mu}\frac{8}{\pi^2}(P_i - P_f)\left(\frac{\pi}{l}\right)^2 \sum_0^\infty e^{-\frac{(2n+1)^2 t}{\tau}}, \qquad \text{Eq. 2-12}$$

combining Eq. 2-11 and Eq. 2-12 yields the shape factor in the following form:

$$\boxed{\sigma(t) = \left(\frac{\pi}{l}\right)^2 \frac{\sum_0^\infty e^{-(2n+1)^2 t/\tau}}{\sum_0^\infty \frac{1}{(2n+1)^2} e^{-(2n+1)^2 t/\tau}} = \left(\frac{\pi}{l}\right)^2 \frac{\sigma_1(t)}{\sigma_2(t)}} \qquad \text{Eq. 2-13}$$

The shape factor for this specific initial boundary value problem is indeed time-dependent as announced. Let us now examine its time dependency and specifically how it behaves at short-time ($t/\tau \ll 1$) and late-time ($t/\tau \gg 1$) regimes. For late time regime ($t/\tau \gg 1$), the series expansions can be approximated by their first term only ($e^{-t/\tau}$) and they cancel out as:

$$\boxed{\lim_{t\to\infty} \sigma(t) = \left(\frac{\pi}{l}\right)^2} \qquad \text{Eq. 2-14}$$

This late time approximation ($t \to \infty$) simplifies to a constant value for shape factor as Warren and Root proposed. In the early time regime $t/\tau \ll 1$, the numerator and denominator do not cancel and σ is time-dependent. Figure 2-3 shows the plots for the σ_1/σ_2 ratio in early and late time scale.

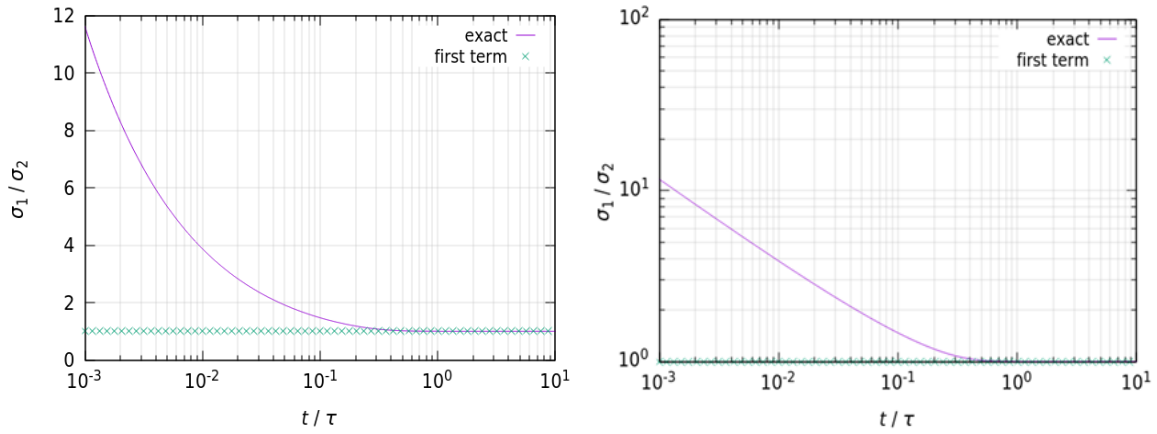


Figure 2-3 Comparison of the time-dependent part of shape factor (Eq. 2-13) with its late time approximation (Eq. 2-14) in linear and logarithmic y-axis.

Finally, if we plot the estimation for different number of terms in the series expansion Eq. 2-13, we can observe the convergence of numerator (σ_1) and denominator (σ_2) to the exact solution as shown in Figure 2-4.

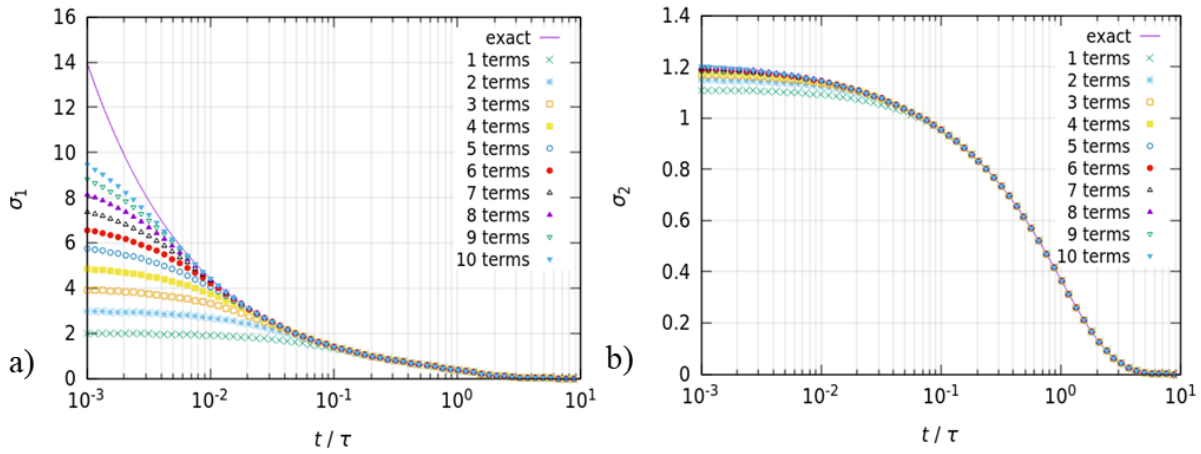


Figure 2-4 Expansion of the series solution of $\sigma_{1,2}$ (numerator and denominator of Eq. 2-13) and convergence speed to exact solution. All expansions converges to the exact solution at late times ($t/\tau \gg 1$).

We can conclude that the convergence approximation mainly concerns the numerator (σ_1) at early time regime (which, needs more than 10 terms of series expansion) while the denominator (σ_2) is converging fast (with only 5 terms). The series expansion σ_1 can be estimated with the following expression (using below Poisson summation formula):

$$\sigma_1(t) = \sum_{n=0}^{\infty} e^{-(2n+1)^2 t/\tau} = \frac{\sqrt{\pi}}{4\sqrt{\frac{t}{\tau}}}\left[1 + 2\left(\sum_{k=1}^{\infty} e^{-\pi^2 k^2 \tau/t} - \sum_{k=0}^{\infty} e^{-\pi^2 (2k+1)^2 \tau/(4t)}\right)\right]$$

$$\sim \frac{\sqrt{\pi}}{4\sqrt{\frac{t}{\tau}}} \qquad for \frac{t}{\tau} \ll 1$$

Eq. 2-15

Figure 2-5 shows the accuracy of series estimation of Eq. 2-15, where the approximation converges to the full series expansion in the early times, which is up to $t/\tau = 1$. Also, we can plug in the approximation of Eq. 2-15 into the average pressure calculation to quantify the validity range. Figure 2-6 shows the early time estimation of transient flow is valid up to $t/\tau = 1$ and the late time approximation of series solution converges to the exact solution about $t/\tau = 0.5$ and larger times. Note that the time limit of early time approximation ($t/\tau = 1$) is longer than the time it takes until the diffusion front reaches the model boundary as seen in Figure 2-1.

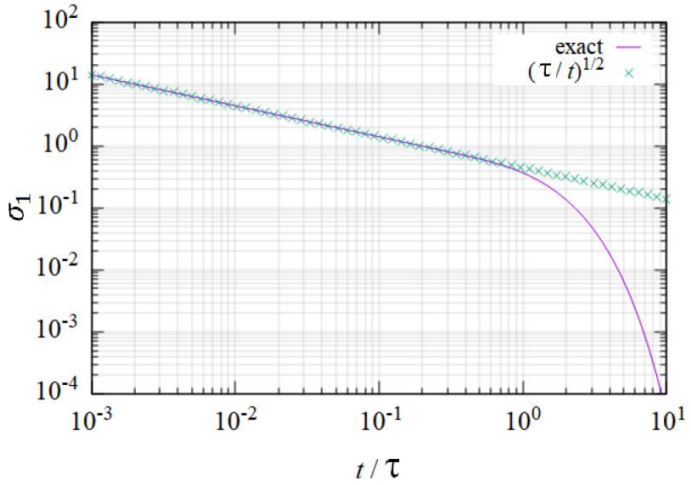


Figure 2-5 Comparison of the exact series expansion σ_1(numerator of time-dependent shape factor in Eq. 2-13) and its early time ($t/\tau \ll 1$) approximation Eq. 2-15.

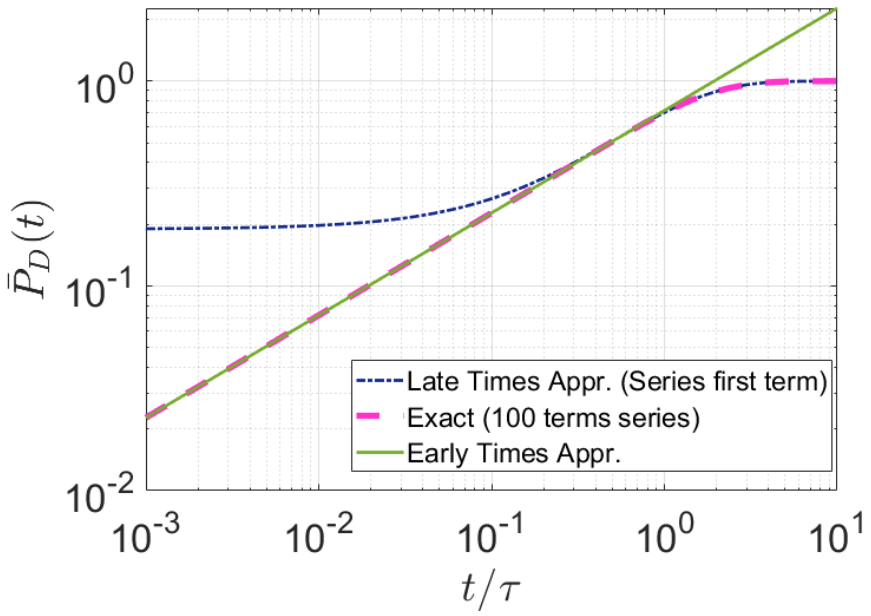


Figure 2-6 Comparison of the exact average block pressure Eq. 2-10 (approximated by analytical series expansion with 100 terms) with its early time approximation ($t/\tau \ll 1$ giving Eq. 2-15) and late time approximation ($t/\tau \gg 1$ expansion with first term in exact solution)

We can observe that the uniform pressure distribution (Eq. 1-15) in the matrix (approximation by a constant shape factor) is reached after an initial transient transfer period during which the transfer through matrix blocks is not influenced by block size, i.e. is **Infinite Acting** (acting as a block of infinite size). However, that transient period is very short for transfers driven by pressure diffusivity; hence it can be neglected when predicting the long-term production from conventional reservoirs. But for transfers driven by multiphase and/or slow transfer mechanisms like molecular diffusion or capillary imbibition or in well-test

analysis (large-scale reservoirs), the transient transfer period lasts for a long time and should be considered. The transient period can be scaled by characterization time (τ), which is about 10^5 days for molecular diffusion in comparison with less than 1 hour for pressure diffusion in a matrix block of 1 meter.

The final analytical formulation for the shape factor for this particular problem can be expressed at early and late times as:

$$\sigma(t) = \left(\frac{\pi}{l}\right)^2 \frac{\sigma_1(t)}{\sigma_2(t)} \sim \begin{cases} \left(\frac{\pi}{l}\right)^2 \dfrac{\dfrac{\sqrt{\pi}}{4\sqrt{\frac{t}{\tau}}}}{\sum_0^5 \frac{1}{(2n+1)^2} e^{-(2n+1)^2 t/\tau}} & for\ t/\tau \ll 1 \\ \left(\frac{\pi}{l}\right)^2 & for\ t/\tau \gg 1 \end{cases} \quad \text{Eq. 2-16}$$

Based on Figure 2-7 results, ("Instantaneous") shape factor values decrease rapidly to lower values, until an asymptotic quasi-constant value is reached for t/τ exceeding about 0.5 to 1, which is consistent with the dimensionless time found by various authors. This regime, also known as **pseudo-steady state (PSS)** transfer, refers to approximation of flux by a constant shape factor. One can also call the inter-porosity flux approximation of late time as the PSS linear inter-porosity or closure.

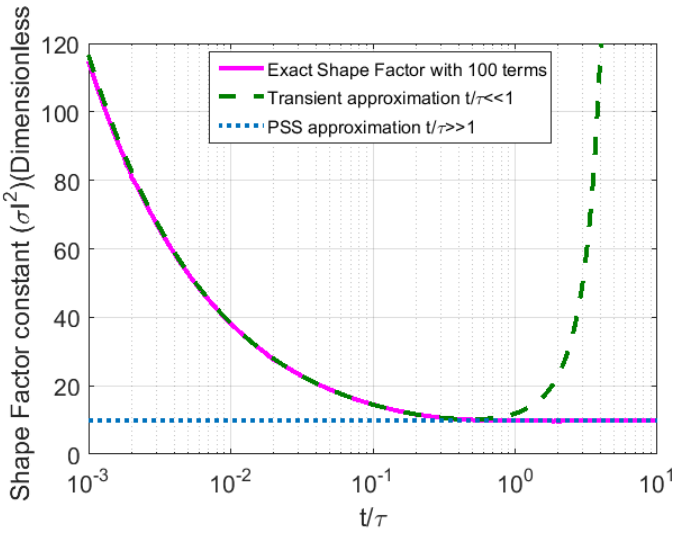


Figure 2-7 Exact analytical ("Instantaneous") shape factor with early- and late-times approximations (from Eq. 2-16) in dimensionless time with $\tau = \frac{1}{D^*}\left(\frac{l}{\pi}\right)^2$. Shape factor values are dimensionless based on the block length (l).

The early matrix-fracture transfer is time-dependent and depends on a series of relaxation time (diffusivity coefficient and block geometrical features). But, at late-times, the shape factor converges to a size-dependent constant value of $\frac{\pi^2}{l^2}$ and PSS linear closure estimates matrix-fracture transfer with good accuracy. The same type of calculation can be performed on other simple homogeneous and isotropic 2D and 3D geometries and leads to approximately the same result, with additional characteristic lengths that are involved and that are representative of the considered matrix block geometry. For example, late time asymptotic value for 2D cube, 3D cubic, cylindrical and spherical blocks (with radius of R) are $\frac{2\pi^2}{l^2}$, $\frac{3\pi^2}{l^2}$, $\frac{23.3}{R^2}$ and $\frac{39.3}{R^2}$ respectively. Some of those approximations are presented in 2.5.

The model proposed by Warren and Root has been a framework for many applications. It gave rise to several subsequent investigations focused on the evaluation of the transfer function through different definitions of the well-known shape factor. Recently, the concept of the shape factor has been enlarged to consider not only the size and shape of the matrix block but also other flow mechanisms and other flow conditions.

2.5 Literature review on dual-medium shape factors

Some studies tried to develop or discretize the Warren and Root equation for different matrix block shapes and conditions. (Kazemi et al., 1976) presented an extension of the dual-porosity model of Warren and Root to a two-phase flow numerical simulator, which could account for the relative mobility of fluids, gravity, imbibition, and variable formation properties.

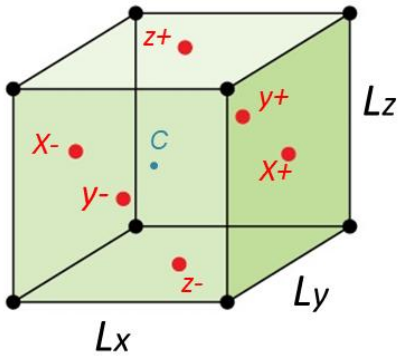


Figure 2-8 Formulation of shape factor transfer for a parallelepiped matrix block and surrounding fractures by assuming a transfer length from each face ($s = x^-, x^+, y^-, y^+, z^-, z^+$) to the block center ($c$).

Three-dimensional matrix-fracture transfer is formulated for a seven-point elementary volume, as shown in Figure 2-8, L_x,L_y and L_z are the dimensions of the identical matrix blocks that represent the matrix medium in that cell. (Kazemi et al., 1992) proposed a more general form of shape factor to account for the effect of matrix-block boundary geometry:

$$\sigma = \frac{1}{V_m}\sum_{s=1}^{n}\frac{A_s}{l_s}, \qquad \text{Eq. 2-17}$$

where V_m is the volume of matrix block, *s* refers to one face of that matrix block open to transfer, A_s is the area of that face, l_s is the flow length that can be the distance from that face to the center of the matrix block, and *n* is the total number of faces of the matrix block open to imbibition. This shape factor is calculated based on the matrix block volume and integrating the surface open to flow in all directions and the distances of these surfaces to the center of the matrix block. A method to define a characteristic length of a matrix block, is the average flow length of an irregular matrix block and can be defined as:

$$L_c = \frac{1}{\sqrt{\sigma}}. \qquad \text{Eq. 2-18}$$

The larger the shape factor, the smaller the average flow length. In reality, this characteristic length changes from early times (transient period) to late times.

To drive the simplest case investigated in this chapter (flow in a cubic parallelepiped), we consider flow across the 6 faces ($s= x^-, x^+, y^-, y^+, z^-, z^+$). Kazemi method calculates the shape factor expression as below:

$$\sigma = \frac{1}{L_x L_y L_z}\left(2\times\frac{L_y L_z}{\frac{L_x}{2}} + 2\times\frac{L_x L_z}{\frac{L_y}{2}} + 2\times\frac{L_x L_y}{\frac{L_z}{2}}\right) \qquad \text{Eq. 2-19}$$

which simplifies to:

$$\sigma = 4\left(\frac{1}{L_x^2}+\frac{1}{L_y^2}+\frac{1}{L_z^2}\right). \qquad \text{Eq. 2-20}$$

Most classical models use the inter-porosity flux calculation of Eq. 1-15 for all the time with a constant (time-invariant) shape factor that is a function of matrix block dimensions and involves a dimensionless pre-factor (known as shape factor constant) equal to 4 for a cube.

Indeed, several studies found that shape factor expression Eq. 2-20 needed some corrections, and alternative approximations were proposed (Coats, 1989; Ueda et al., 1989).

(Lim & Aziz, 1995) introduced a more general form of shape factor, including the anisotropy concept. Their derivation for matrix-fracture shape factor was based on analytical solutions of pressure diffusivity in a matrix block subjected to a constant fracture pressure condition on its boundary from initial time onwards, as presented in the previous section. Various flow geometries were considered and the analytical solutions to these problems involved no pseudo-steady state assumption. The exact analytical solutions consist of infinite summation series as derived in equations Eq. 2-9 and Eq. 2-10 for a specific case. However, Lim and Aziz formulated shape factor expressions by taking only the first term of those series solutions. This simplification to their solution is also equivalent to assuming a pseudo-steady state transfer, although it is based on the exact solution of transfer, as shown previously. Their general expression of shape factor lumps all the contributions in directions x, y, z to transfer within an anisotropic parallelepidedic matrix block of dimensions L_x, L_y, L_z as:

$$\sigma = \frac{\pi^2}{\bar{k}}\left(\frac{k_x}{L_x^2} + \frac{k_y}{L_y^2} + \frac{k_z}{L_z^2}\right), \qquad \text{Eq. 2-21}$$

with k_x, k_y, and k_z the matrix permeabilities in the three directions x, y, z, and $\bar{k}$ is the geometric average of permeabilities. For an isotropic parallelepidedic matrix block, the shape factor reduces to:

$$\sigma = \pi^2\left(\frac{1}{L_x^2} + \frac{1}{L_y^2} + \frac{1}{L_z^2}\right). \qquad \text{Eq. 2-22}$$

Lim and Aziz show values for one, two and three sets of fractures are compared to previous works (shown in Table 2-1).

(Quintard & Whitaker, 1996) applied large-scale volume averaging techniques under Pseudo Steady-State assumption to find the shape factor constant. This technique can be used for many up-scaling problems, from pore-scale to Darcy-scale and next to the Macro-scale. Through the averaging of local-scale matrix transfers to the scale of the entire matrix block, they determined a constant equal to 49.6 for the shape factor of the 3D transfer in the case of parallelepidedic blocks. In fact, their theory is applicable to any geometry and results in a value much closer to Warren and Root value (60) than from Kazemi's value (12).

Shape factor calculation depends on the transfer mechanism, boundary and initial condition, block size and shape in different fractured porous media. The dual-medium method adopt different expressions of shape factor as shown in a study by (Firoozabadi & Thomas, 1990).

Table 2-1 is an extensive collection of dimensionless shape factor values for 1D, 2D, and/or 3D diffusive transfers, that are found in reported studies herein, where authors assumed a pseudo-steady transfer or considered the whole (transient) transfer process. The geometry is cubic (1D, 2D or 3D) or cylindrical or spherical matrix blocks. Different approached are used to approximate the shape factor for transient (early times) or PSS (late-times). The fracture has a constant pressure or a variable function defined by declining functions (linear, exponential and etc.).

An old version of such table is found in several studies, and it was completed by other recent studies. Although most studies consider only single-phase transfers, significant differences can be found between authors, which reflect differences in assumptions (PSS versus transient), and also the various approaches and solution methods adopted by authors.

Table 2-1 Shape factor constant (σl^2, dimensionless shape factor) for 1D to 3D shapes (rectangular square cube, cylindrecal dimension size = l) based on different calculation approaches and different initial/boundary conditions. More details are provided in the corresponding references.

References	1D	2D	3D	Approach	Flow State PSS/Transient	Fracture Conditions
(Warren & Root, 1963)	12	32	60	Geometrical	PSS	Single Phase
(Kazemi et al., 1976)	4	8	12	Numerical	PSS	Single Phase
(Coats, 1989)	12	28.45	49.85	Analytical	PSS	Single Phase
(Kazemi et al., 1992)	-	-	$3\pi^2$	Analytical	Transient	Single Phase
(Lim & Aziz, 1995)	π^2	$2\pi^2$	$3\pi^2$	Analytical	Transient/PSS	Single Phase
(Quintard & Whitaker, 1996)	12	28.4	49.6	Averaging	Transient	Single Phase
(Bourbiaux et al., 1999)	-	20	-	Numerical	PSS	Single Phase
(Noetinger & Estebnet, 2000)	11.5	27.1	-	Random Walk	Transient	Single Phase
(Sarda et al., 2002)	8	24	48	Numerical	Transient	Single Phase

(Hassanzadeh et al., 2009; Hassanzadeh & Pooladi-Darvish, 2006)	(2006)	9.87	18.2	25.65	Anl. Laplace	PSS	Constant Rate
	(2009)	12	25.13	38.9	Anl. Laplace	Transient	Constant P_f
(Mora & Wattenbarger, 2009)		12	28.43	49.48	Numerical	PSS	Constant Rate
		π^2	$2\pi^2$	$3\pi^2$	Numerical	Transient	Constant P_f
(He et al., 2017)		10	18	26	Analytical	Transient	Non-linear Pressure
(Rostami et al., 2020)		Slab	Cyl	sph			
		4.17	9.7	16.7			Constant P_f
		4.53	11	20.2	Numerical	PSS	Linear dec.
		4.22	9.9	7.2			Exponential
		10	23.3	39.3			Constant P_f
		10	23.3	48.2	Numerical	Transient	Linear dec.
		10.1	23.7	40.9			Exponential

To end with, despite some limitations, the dual-medium approach offers better computational efficiency than the single medium approach to simulate the physics of matrix-fracture transfers. However, in many cases, the diffusive variable (pressure or concentration) cannot be assumed uniform within the matrix blocks, and spatial variability of that variable should be modeled. The underlying matrix flow dynamics can be approximately captured via time- or variable-dependent transfer functions. Procedures along these lines were introduced by, among others, (Penuela et al., 2002; Sarma & Aziz, 2004; Swaan O., 1976; Zimmerman et al., 1993).

A numerical solution of the same initial boundary value problem with fine grid scheme and dual-medium approach will be compared with the analytical solution in the next part to compare the dual-medium calculation with the exact solution.

2.6 Numerical simulation of linear diffusion with fine-grid and dual-medium model

In the following, we introduce the up-scaling issue raised by the dual-medium representation of matrix-fracture transfers, then we compared the dual-medium model results with the reference solution of transfer (analytical or numerical fine-grid model) of the matrix block limited by fractures.

The numerical simulator with single or dual-porosity option is used to predict the diffusion flux between fractures and matrix block. The dual-medium approach as a common up-scaling tool is modified for this one-dimensional linear diffusion problem. The detail of the numerical scheme is presented in Annex A and B. Also, a convergence study is conducted for those simulations and the details are attached to Annex A.

It is recalled that 1D transfer is considered in all models, that is only two opposite faces (x^+, x^-) of the block (shown in Figure 2-9) are open to transfer with fracture; the 4 other faces (y^+, y^-, z^+, z^-) are no-flux ("closed") boundaries.

Table 2-2 summarizes matrix and fracture properties. Note that the fracture permeabilities is not used for matrix-fracture transfer problem but, to show the fluid permeability contrast in each zone.

Table 2-2 Example set of the properties of the simulation model

properties	value
Matrix Porosity (ϕ_m)	0.25
Fracture Porosity (ϕ_f)	0.02
Matrix Permeability (k_m)	10 mD
Fracture Permeability (k_f)	10000 mD
Full Matrix Block Length (l)	1 m
Fluid viscosity	1 cp
Total fluid/rock compressibility	10^{-4} 1/bar
Molecular Diffusion Coefficient (D)	4.3×10^{-11} m^2/s*
*value is taken from surfactant experiment by (Bourbiaux et al., 2016).	

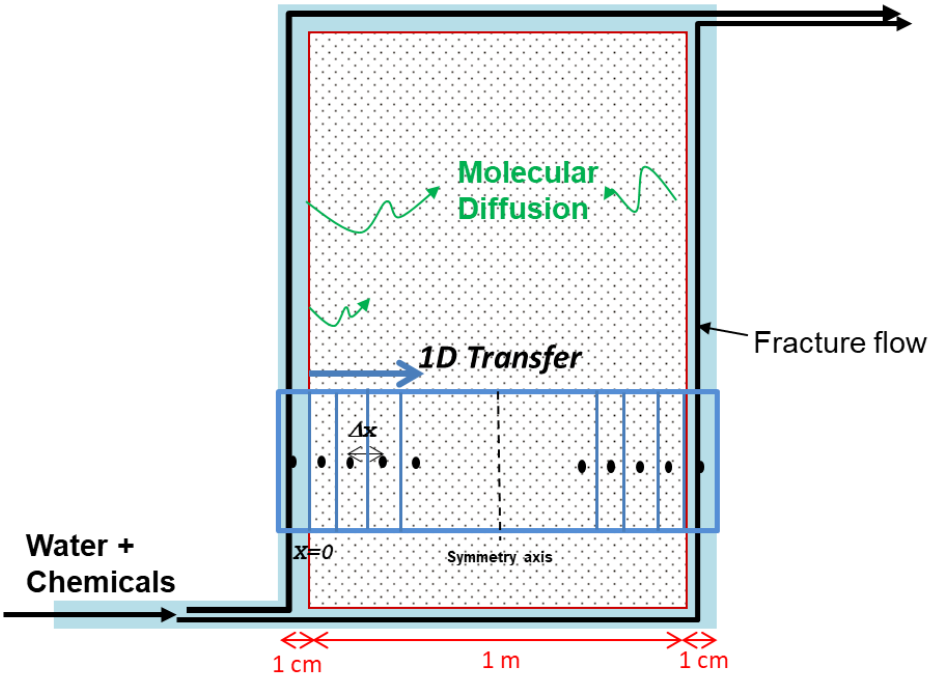


Figure 2-9 Schematic of molecular diffusion in a matrix block surrounded by fracture. The solution is in one-dimension for analytical and numerical fine-grid calculation (discretized *1m* rectangle in *x*-direction) with a symmetry axis at the middle of the block.

Figure 2-10 compares the analytical profiles with the fine-grid solution for diffusion phenomena. This will help us to visualize the time scale and Infinite Acting Flow regime. The fine-grid simulation presents the same pressure profiles and predicts a similar duration of transient transfer. The molecular diffusion produces a similar plot with normalized concentration profiles as Figure 2-10.

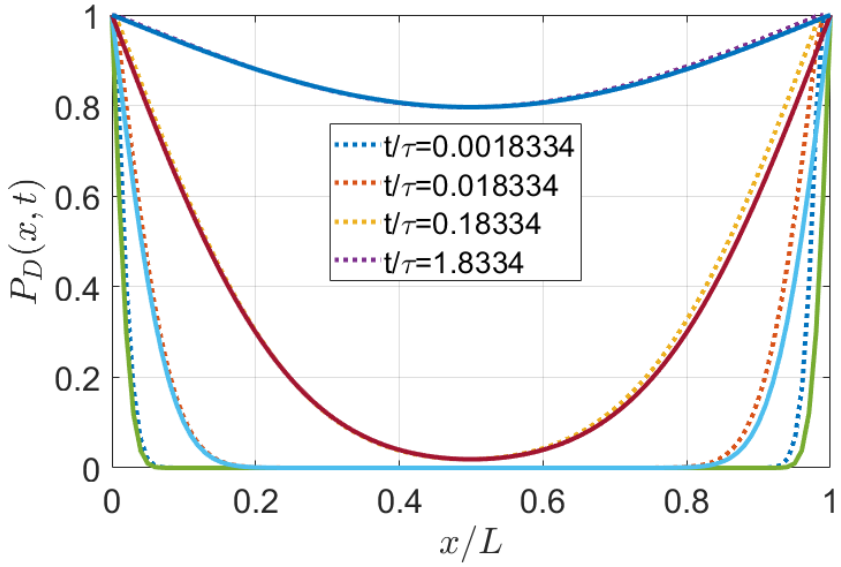


Figure 2-10 Comparison between the numerical simulation (dashed line) and the exact solution (solid line) for a one-dimensional linear diffusion from fracture to matrix block with Dirichlet boundary condition (see Figure 2-9). Corresponding time scale is characterized by τ.

The dual-medium model has not any profile distribution of the desired unknown at the Darcy-scale and the matrix pressure or concentration is represented by an up-scaled (averaged) single value. This evaluation of this value can be compared with an average value from analytical and fine-grid numerical models. Figure 2-11 compares the evolution versus time of the average pressure/concentration in the matrix block, as predicted by the dual porosity model, with the reference analytical (full series expansion) and numerical fine-grids predictions. As already observed, the fine-grid model prediction of average concentration is quasi equal to the analytical solution. On the opposite, the dual-medium model, with Kazemi constant shape factor, largely underestimates matrix-fracture transfers. This difference results from the averaging assumption (Kazemi constant shape factor).

In the coming subsection, this limitation of dual-porosity modeling approach is discussed further and approaches to overcome it, are presented. Next, a procedure to best calibrate the dual-porosity model from a reference solution(s) is applied to the diffusion case under consideration.

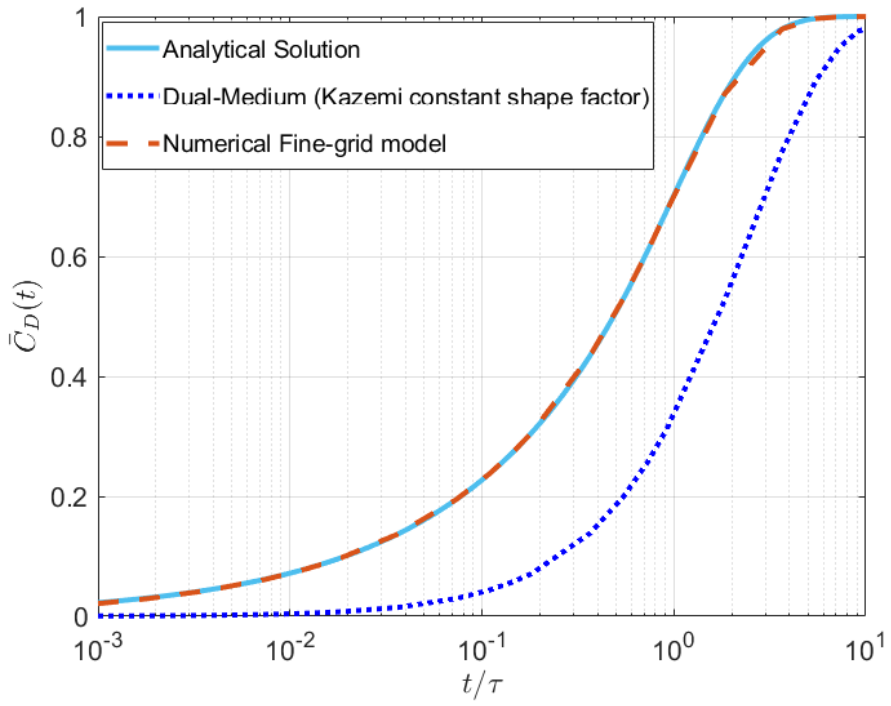


Figure 2-11 Linear diffusion solution with analytical solution (solid line), numerical fine-grid (dashed line) and numerical dual-medium model (dotted line) in dimensionless time with $\tau = \frac{1}{D^*}\left(\frac{l}{\pi}\right)^2$. The classical dual-medium model underestimates the matrix-fracture transfer.

2.7 Methodology to improve/up-scale transient diffusion transfer in dual-medium model

Based on the results above, dual-medium model can be tuned. The dual-porosity simulators, like PumaFlow, include a pseudo-steady state representation of basic mechanisms of matrix-fracture transfer, i.e. a constant shape factor whose value differs from one simulator to another. PumaFlow adopts the Kazemi's value of 4 (for our model of 1D transfer) as a shape factor constant (i.e. pre-factor or dimensionless shape factor), which is not a very good estimate as shown in our study (see Figure 2-11), but the code offers the possibility to input a multiplier for this value.

Regarding the analytical approach, $\bar{P}_m(t)$ in the formulation Eq. 2-10 can be calculated from a full series expansion (produces the purple dashed line in Figure 2-6) or can be estimated by series approximation in early and late times. Similarly, the time derivation of matrix average pressure with early time approximation gives:

$$\Phi_{mf}(t) = \phi_m\, c_m \frac{\partial \bar{P}_m}{\partial t} =$$

$$= \frac{8\phi_m\, c_m}{\pi^2 \tau}(P_i - P_f)\sum_0^\infty e^{-\frac{(2n+1)^2 t}{\tau}} \approx \begin{cases} \dfrac{2\phi_m\, c_m (P_f - P_i)}{\pi^{3/2}\tau}\sqrt{\dfrac{\tau}{t}} & \text{for } t/\tau \ll 1 \\ \dfrac{8\phi_m\, c_m (P_f - P_i)}{\pi^2 \tau} e^{-t/\tau} & \text{for } t/\tau \gg 1 \end{cases} . \qquad \text{Eq. 2-23}$$

Based on Eq. 2-23 the matrix-fracture flux can be estimated for early- and late- times with two different time dependencies where two different regimes appear in a log-log and semi-log plots in Figure 2-12. Molecular diffusion transfer gives the same estimation just with substituting $\bar{P}_m$ with $\bar{C}_m$. Therefore, the time dependency of the matrix-fracture flux is controlled by the flow regime (early- or late-times) conditions. The characteristic time for transition time from the early time transient flow to a late time approximation becomes crucial. A similar value of the characteristic time of the early time period has been determined by many authors, at least for diffusive physical mechanisms of transfer, although the corresponding real time duration (t) may or may not be neglected, depending on the diffusivity coefficient and block size (included in parameter τ). This characteristic time is more complicated in the case of pure imbibition, i.e., a non-linear diffusion problem, which is the objective of the next chapter.

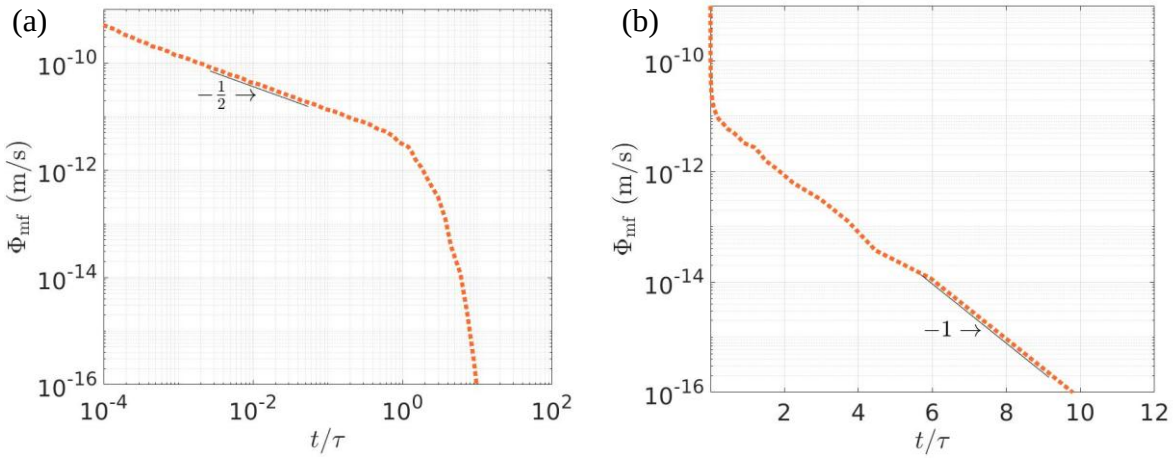


Figure 2-12 Matrix-fracture diffusion flux calculation with fine-grid numerical model in (a) log-log and (b) semi-logarithmic scale in dimensionless time with $\tau = \frac{1}{D^*}\left(\frac{l}{\pi}\right)^2$. Two distinguished flow behaviour can be observed in both plots.

A common engineering method to improve the dual-medium models (in comparison with the exact solution in Figure 2-11) is adjusting the classical shape factor with multipliers. Our dual-porosity model underestimates transfer rates at early times as expected but also at late times because the Kazemi shape factor (pre-factor equal to 4 for 1D transfer) is used in the simulator instead of the exact asymptotic value (π^2) that is 2.5 times the Kazemi value 4. The dual-porosity model can then be adjusted at late times by using a multiplier equal to 2.5, as shown in Figure 2-13. But then, prediction at early times remains unsatisfactory as expected: it would require adopting a higher value of the multiplier but such an adjustment would then lead to overestimated concentrations at late times. In addition, the flow rate decreases at late times and consequently, the effect of actual values of the shape factor decreases. In other words, matching a dual-medium model based on a constant shape factor equation cannot describe the whole transfer that is transient by essence.

It has already been observed in the literature that a correction larger than 2.5 gives a better approximation, i.e., a lower norm of the difference between actual and predicted average pressures. If one wants to minimize the error at any time, several options are available. A time convolution with closure would provide an exact solution. Another option is the use of a time dependent shape factor, with the drawback that this is only acceptable if one solves the same initial boundary value problem. To avoid such a hindrance, it is possible to introduce a non-linear variation of the shape factor with the average fields, as described below.

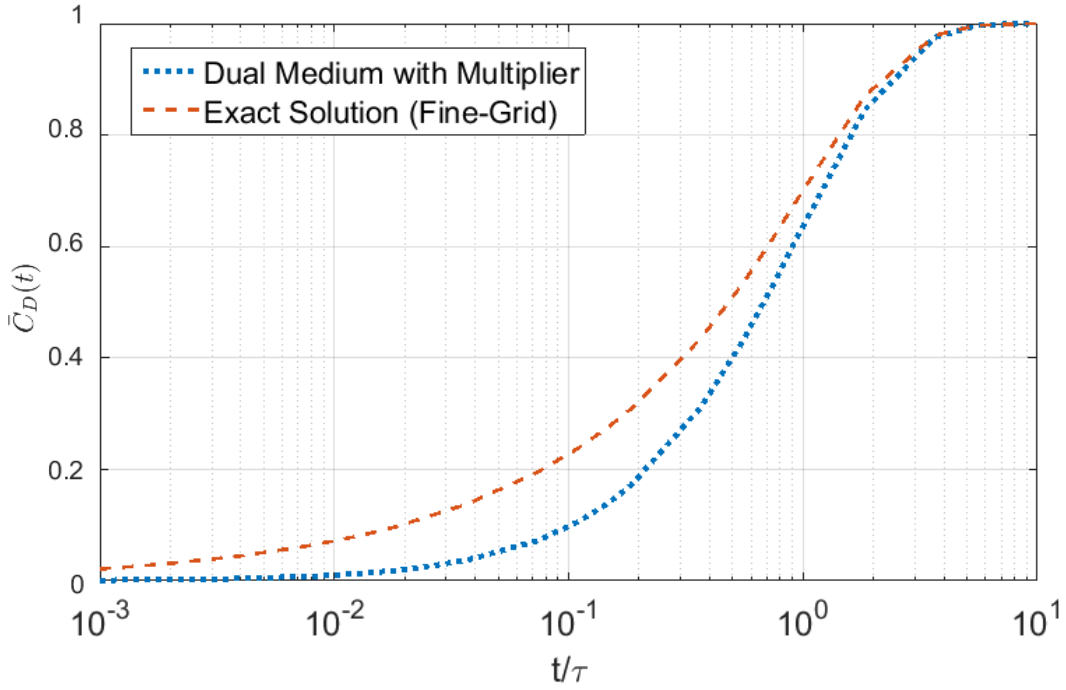


Figure 2-13 Comparison of modified dual-medium model with a multiplier (late time asymptotic correction $\frac{\pi^2}{4} = 2.5$) with the exact solution (analytical solution or fine-grid simulation). A convergence toward the exact solution is observed, a better modification based on non-linear early time dependency is required.

A more predictive transfer model from the dual-porosity method could consist of a multiplier function ($\Psi(t)$) (to be multiplied to the shape factor constant) from early times to late times for any case. This multiplier is the ratio of the actual (transient) transfer rate (Φ_{tr}) to the transfer rate calculated by the dual-medium model under pseudo-steady state assumption (Φ_{PSS}). It can be determined from the analytical solution or from fine-grid simulation results:

$$\frac{\Phi_{tr}}{\Phi_{PSS}} = \Psi(t). \qquad \text{Eq. 2-24}$$

This ratio, for the constant fracture boundary problem, could be calculated using a similar study by (Bourbiaux & Ding, 2016; Zimmerman et al., 1993) to determine pressure-dependent shape factor for transient matrix-fracture transfers. Regarding the diffusion mechanism studied herein, that methodology would be applicable, for example, for a constant fracture concentration boundary condition.

The late time ($t/\tau \gg 1$) transfer rate can be expressed by Eq. 2-16 for concentration (substituting P by C) as the diffusive unknown with a constant shape factor as:

$$\Phi_{PSS}(t) \approx \left(\frac{\pi}{l}\right)^2 \phi_m \frac{D}{\tau_s} \left(\bar{C}_m(t) - C_f\right). \qquad \text{Eq. 2-25}$$

The early time ($t/\tau \ll 1$) transfer rate is estimated using Eq. 2-23 as:

$$\Phi_{tr}(t) \approx \phi_m \frac{2\left(C_f - C_i\right)}{\pi^{3/2}\tau} \sqrt{\frac{\tau}{t}}. \qquad \text{Eq. 2-26}$$

Also, using those approximations of the previous chapter, we can recall the dimensionless parameter as:

$$\bar{C}_D(t) = \frac{\bar{C}_m(t) - C_i}{C_f - C_i} \approx \begin{cases} \dfrac{4}{\pi^{3/2}} \sqrt{\dfrac{t}{\tau}} & for\ t/\tau \ll 1 \\ 1 - \dfrac{8}{\pi^2} e^{-t/\tau} & for\ t/\tau \gg 1 \end{cases}. \qquad \text{Eq. 2-27}$$

Dividing Eq. 2-26 and Eq. 2-25 and combining the early time estimation of Eq. 2-27 yields:

$$\frac{\Phi_{tr}}{\Phi_{PSS}} = \Psi\left(\bar{C}_D(t)\right) = \frac{8}{\pi^3} \frac{\left(C_f - C_i\right)^2}{\left(C_f - \bar{C}_m(t)\right)\left(\bar{C}_m(t) - C_i\right)}. \qquad \text{Eq. 2-28}$$

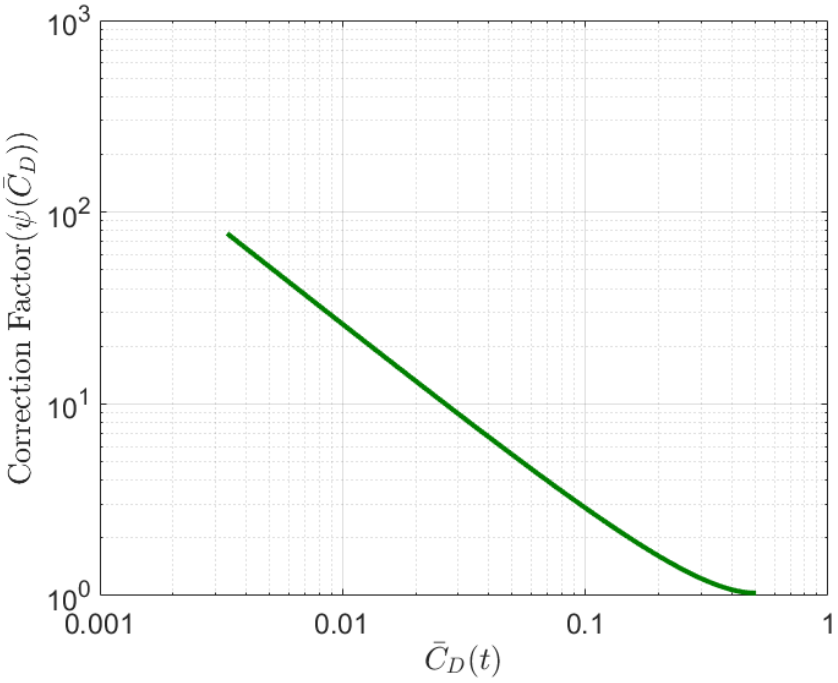


Figure 2-14 Dual-medium shape factor correction versus average concentration of matrix block for a linear diffusion transfer with constant fracture boundary condition. The correction function is based on variable of interest (concentration) and is valid only for early times.

This correction factor would enable the user to input a concentration-dependent (or pressure dependent) shape factor to correct the full-time PSS transfers calculated by conventional dual-porosity simulators and is worthwhile as it is based on the matrix concentration and not time. The valid range of concentration for this relationship is the valid early time approximation of $\bar{C}_D(t)$ that is $t/\tau \ll 1$. In terms of matrix dimensionless concentration, the correction is valid up to $\bar{C}_D \approx \frac{1}{2}$, which corresponds to the minimum value of the correction factor. Figure 2-14 shows the correction factor that can be applied for different matrix concentration values.

Finally, Figure 2-15 compares the exact fine-grid model with dual-medium model that contains the correction factor of Eq. 2-28 as multipliers for early time transient flow, and a full-time multiplier of 2.5 derived in this section. The accuracy of match in early times depends on the sampling of $\bar{C}_D(t)$ from exact analytical or fine-grid numerical solution, which is 16 correction factors in the matching process of Figure 2-15.

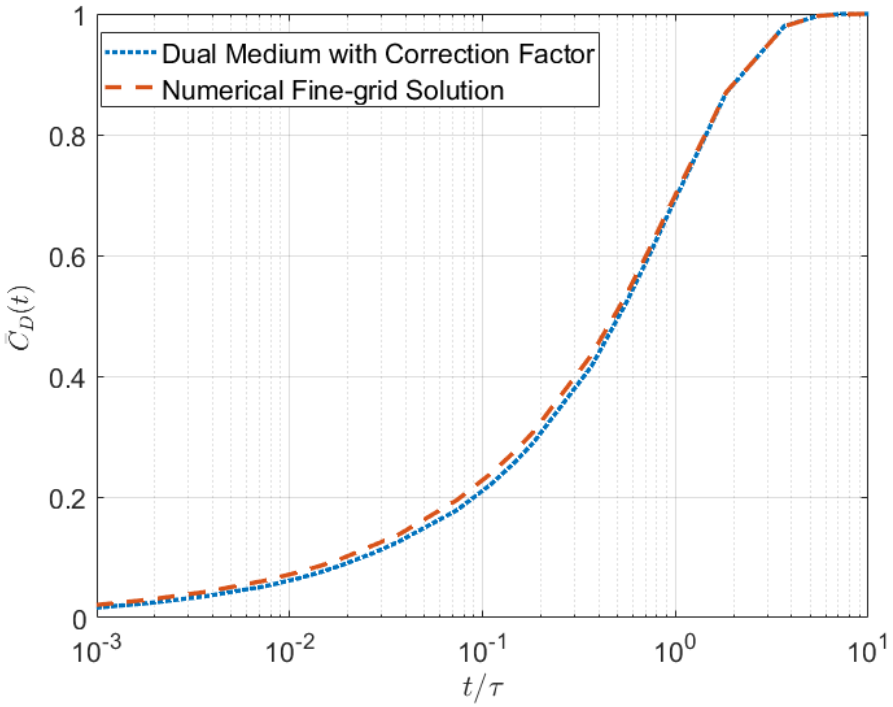


Figure 2-15 Matching the dual-medium model with the fine-grid model (or exact solution) using dynamic correction factors (Eq. 2-28) for early times ($t/\tau \ll 1$) and a asymptotic multiplier (2.5) for full period of the transfer.

2.8 Discussion

References from the abundant literature on fractured reservoir modeling enlightened the basis of the dual-medium modeling concept, underlying assumptions, and implementation issues with dual porosity numerical simulators. Industrial dual-porosity simulators include a pseudo-steady state representation of basic mechanisms of matrix-fracture transfer, i.e., a constant shape factor whose value differs from one simulator to another. The literature review shows there are different approaches to obtaining a constant shape factor.

Single-phase diffusive transfer is developed for viscous flow and molecular diffusion which, both models can be essential in recovery from fractured porous media. However, molecular diffusion is slower by several orders of magnitude in comparison with pressure diffusion transfer. A specific boundary condition is considered to find an analytical solution for those linear partial differential equations. We showed that the matrix-fracture transfer is transient by essence and cannot be modeled by a constant shape factor approach in many cases. Dimensionless formulations enabled us to find some consensus between reported studies: for instance, the transition between early-time and-late time behaviors is found to occur about the characteristic diffusion time (τ) depending on the diffusion coefficient value and block length.

Several authors expressed that the shape factor is not just dependent on the matrix block shape but the transfer mechanism and the conditions. However, the difficulty concerns the more complex transfer mechanisms involved in multiphase transfers, as underlined by (Bourbiaux et al., 1999) who studied single- and two-phase transfers separately. One has to be aware that shape factor formulation should consider the fracture boundary condition and this treatment would be applicable only for a constant fracture boundary condition problem. If the fracture concentration changes with time, the transfer flux must be expressed as a time superposition of fixed fracture concentration responses that is a more general solution and can be calculated by using the convolution principle. Such a treatment was performed by (Zimmerman et al., 1993).

The proposed method requires also further investigation to be applicable to multiphase transfers involving several physical mechanisms. Multiphase flow conditions introduce more difficulties in the solutions to deal with previous issues (as does also the compressibility of fluids and/or porous medium). The next chapter aims to up-scale the matrix-fracture transfer for a two-phases recovery process where capillary diffusion becomes crucial among different physical transfer mechanisms.

To finish the discussion, we have assumed a simple one-dimensional block to derive an analytical approximation of the shape factor, while the real multi-dimensional systems (e.g., a distribution of different matrix block sizes and shapes) demand more effort to obtain an approximation of the inter-porosity flux.

2.9 References

Bourbiaux, B., & Ding, D. (2016). Simulation of Transient Matrix-Fracture Transfers of Compressible Fluids. *Transport in Porous Media*, *114*(3), 695–717. https://doi.org/10.1007/s11242-016-0740-9

Bourbiaux, B., Fourno, A., Nguyen, Q.‐L., Narrant, F., Robin, M., Rosenberg Elisabeth, & Argillier Jean-Francois (2016). Experimental and Numerical Assessment of Chemical Enhanced Oil Recovery in Oil-Wet Naturally Fractured Reservoirs. *SPE Journal*, *21*(3), Article SPE-169140-PA.

Bourbiaux, B., S. Granet, P. Landereau, B. Noetinger, S. Sarda, & J.C. Sabathier (Eds.) (1999). *Scaling Up Matrix-Fracture Transfers in Dual-Porosity Models: Theory and Application*. : *SPE 56557*.

Carslaw, H. S., & Jaeger, J. C. (1959). *Conduction of Heat in Solids* (Second edition). Oxford University Press.

Coats, K. H. (Ed.) (1989). *Implicit Compositional Simulation of Single- Porosity and Dual-Porosity Reservoirs*.

Crank, J. (1975). *The Mathematics of Diffusion* (Second Edition). Oxford University Press.

Fick, A. (1855). Ueber Diffusion, *170*(1), 59–86. https://doi.org/10.1002/andp.18551700105

Firoozabadi, A., & Thomas, L. K. (1990). Sixth SPE Comparative Solution Project: Dual-Porosity Simulators. *Journal of Petroleum Technology*, *42*, 710–715.

Ghanbarian, B., Hunt, A. G., Ewing, R. P., & Sahimi, M. (2013). Tortuosity in Porous Media: A Critical Review. *Soil Science Society of America Journal*, *77*(5), 1461–1477. https://doi.org/10.2136/sssaj2012.0435

Hassanzadeh, H., & Pooladi-Darvish, M. (2006). Effects of Fracture Boundary Conditions on Matrix-fracture Transfer Shape Factor. *Transport in Porous Media*, *64*(1), 51–71. https://doi.org/10.1007/s11242-005-1398-x

Hassanzadeh, H., Pooladi-Darvish, M., & Atabay, S. (2009). Shape factor in the drawdown solution for well testing of dual-porosity systems. *Advances in Water Resources*, *32*(11), 1652–1663. https://doi.org/10.1016/j.advwatres.2009.08.006

He, Y., Chen, X., Zhang, Y., & Yu, W. (2017). Modeling interporosity flow functions and shape factors in low-permeability naturally fractured reservoir. *Journal of Petroleum Science and Engineering*, *156*, 110–117. https://doi.org/10.1016/j.petrol.2017.05.006

Kazemi, H., Gilman, J. R., & Elsharkawy, A. M. (1992). Analytical and Numerical Solution of Oil Recovery From Fractured Reservoirs With Empirical Transfer Functions. *SPE Reservoir Engineering*, *7*(2), Article SPE-19849-PA, 219–227.

Kazemi, H., Merrill, L. S., & Zeman, P. A. (1976). Numerical Simulation of Water-Oil Flow in Naturally Fractured Reservoirs. *SPE Journal*, *16*(6), Article 5719, 317–326.

Lim, K. T., & Aziz, K. (1995). Matrix-Fracture Transfer Shape Factors for Dual-Porosity Simulators. *Journal of Petroleum Science and Engineering*, *13*, 169–178.

Mora, C. A., & Wattenbarger, R. A. (2009). Analysis and Verification of Dual Porosity and CBM Shape Factors. *Journal of Canadian Petroleum Technology*, *48*(2), 17–21.

Noetinger, B., & Estebnet, T. (2000). Up-scaling of double porosity fractured media using continuous-time random walks methods. *Transport in Porous Media*, *39*(3), 315–337.

Penuela, G., Hughes, R., Civan, F., & et al. (Eds.) (2002). *Time-dependent shape factors for secondary recovery in naturally fractured reservoirs*. : *SPE-75234-MS*.

Pisani, L. (2011). Simple Expression for the Tortuosity of Porous Media. *Transport in Porous Media*, *88*(2), 193–203. https://doi.org/10.1007/s11242-011-9734-9

Quintard, M., & Whitaker, S. (1996). Transport in Chemically and Mechanically Heterogeneous Porous Media I: Theoretical Development of Region-Averaged Equations for Slightly Compressible Single-Phase Flow. *Advances in Water Resources*, *19*, Article 0309-1708(95)00023-C, 29–47.

Reis, R. A., Oliveira, J. V., & Nobrega, R. (2001). Diffusion coefficients in polymer-solvent systems for highly concentrated polymer solutions. *Braz. J. Chem. Eng.*, 18. https://doi.org/10.1590/S0104-66322001000400003

Rostami, P., Sharifi, M., & Dejam, M. (2020). Shape factor for regular and irregular matrix blocks in fractured porous media. *Petroleum Science*, *17*(1), 136–152. https://doi.org/10.1007/s12182-019-00399-9

Sarda, S., Jeannin, L., Basquet, R., & Bourbiaux, B. (2002). Hydraulic Characterization of Fractured Reservoirs: Simulation on Discrete Fracture Models. *SPE Reservoir Evaluation & Engineering*, *5*(02), 154–162. https://doi.org/10.2118/77300-PA

Sarma, P., & Aziz, K. (Eds.) (2004). *New transfer functions for simulation of naturally fractured reservoirs with dual porosity models*.

Swaan O., A. de (1976). Analytic Solutions for Determining Naturally Fractured Reservoir Properties by Well Testing. *SPE Journal*, *16*(03), 117–122. https://doi.org/10.2118/5346-PA

Ueda, Y., Murata, S., Watanabe, Y., & Funatsu, K. (Eds.) (1989). *Investigation of the Shape Factor Used in the Dual-Porosity Reservoir Simulator*.

Warren, J. E., & Root, P. J. (1963). The Behavior of Naturally Fractured Reservoirs. *SPE Journal*, *3*, 245–255. https://doi.org/10.2118/426-PA

Weissberg, H. L. (1963). Effective Diffusion Coefficient in Porous Media. *Journal of Applied Physics*, *34*(9), 2636–2639. https://doi.org/10.1063/1.1729783

Zimmerman, R. W., Chen, G., Hadgu, T., & Bodvarsonn, G. S. (1993). A numerical dual-porosity model with semianalytical treatment of fracture/matrix flow. *Water Resources Research*, *29*(7), 2127–2137.

3 Non-linear Diffusion Transfer in Fractured Porous Media

Studying non-linear diffusion phenomena in fractured porous media is a generic problem which is often encountered in applications involving displacement of NAPL by water. In this chapter, we investigate the two-phase flow in a finite size matrix block approximated by a layer of length L embedded in a fracture network of high conductivity, including the mechanism counter-current capillary imbibition. The two-phase condition brings up the new mechanisms as capillary imbibition and gravity force. In many situations of practical interest, capillarity is the dominant driving force. This mechanism, as will be shown, is a non-linear diffusion. We revisit the problem by presenting two exact asymptotic solutions valid for early and late times, under the assumption that the conductivity vanishes as a power-law of both phase saturations at the extreme values of the fluid saturation. Also, the numerical calculation of the full problem is compared with available solutions. The analytical solution is in very good agreement with results of numerical simulations involving various realistic sets of input transport parameters. The late time solution is generelized to any two- or three-dimensional domain of arbitrary shape.

As it was shown in single-phase diffusion, the flux calculation may be represented as a non-linear exchange term involving the average block saturation, weighted by a shape factor. The findings in this chapter permit to set-up an analytical formulation generalizing linear single-phase representation of matrix-to-fracture exchange term. This formulation accounts for the non-linearity of the local flow equations using the power-law dependence of the conductivity for low NAPL saturation. To finish with, we set up a spatially averaged macroscopic dual-porosity representation of the imbibition process and demonstrate its accuracy in reproducing the two dynamical imbibition regimes.

3.1 Introduction

In many situations, fluid transport processes in complex systems may be described by the solution of a non-linear diffusion equation with a diffusion coefficient that depends on the local concentration or saturation of the phase of interest. In the geosciences context, this can be the case when considering non-aqueous phase liquids (NAPL) displacement by water in

aquifers (Brusseau, 1992; Brutsaert & Weisman, 1970; Philip, 1955b), hydrocarbon recovery in rock matrix (Kashchiev & Firoozabadi, 2003; Morrow & G. Mason, 2001; Silin & Patzek, 2004), steam migration in high enthalpy geothermal systems, or CO_2 storage by capillary trapping. Other systems may receive similar descriptions ranging from astrophysics to filtration, including compressible gas flows, granular media flows. So that quite generic problem was investigated using several approaches (Bruce & Klute, 1956a; Hansen et al., 2020; Heaslet & Alksne, 1961).

The non-linearity of the driving diffusion equation implies that most of standard methods based on superposition properties such as Green's functions and Fourier decomposition fail down and there is no general and exact analytical solution. In addition, the popular assumption that the diffusion coefficient vanishes at the limiting saturations, sharing a power-law dependence with the saturation adds a mathematical difficulty (explained by (Babu & Van Genuuchten M. T., 1979, April)). In particular, singular behaviors are to be expected close to the forcing boundaries where the diffusion coefficient may vanish.

In the geoscience context, such a generic problem arises when considering a spontaneous counter-current capillary imbibition process on a finite size matrix block. Spontaneous imbibition (SI) is the process by which a wetting fluid (like water or brine) spontaneously enters a porous medium and displaces a non-wetting fluid (like NAPL, oil, air, or CO_2). As mentioned in the first chapter, it is the main recovery mechanism in many fractured oil reservoirs, especially water-wet to intermediate wettability reservoirs developed by water injection. The spontaneous counter-current imposes no overall advection flow, so the water transport is controlled by such a diffusion equation. Also, as discussed in chapter 2, in fractured media context, most authors attempted to get an effective equation driving flow in the fracture domain only by adopting a suitable dual-porosity description with a lumped description of the flow inside the matrix blocks. That description implies determining a matrix to fracture mass flux related to average matrix quantity by means of some closure that avoids the knowledge of the spatial details of the concentration distribution inside the matrix.

Dual-porosity models involving a linear closure (local inter-porosity flux proportional to pressure/saturation/concentration difference) imply an exponential relaxation of the average quantity of interest, i.e., a single relaxation time. The associated characteristic time corresponds to the diffusion time over the matrix size ($\tau_0 = L^2/D_0$), is defined using some representative diffusion coefficient (D_0), and a representative matrix block size (L). At short times, a self-

similar (boundary-layer) behavior is observed and can be estimated using the standard Boltzmann transformation, leading to a matrix to fracture flux varying as $t^{-1/2}$ (Hansen et al., 2020; L. Li et al., 2020). This regime may be observed while the diffusion distance remains lower than the typical size of the matrix block. Fewer results may be found regarding the late-time regime description occurring when water invaded most of the pore volume of the rock. Using an overall dual-porosity description with a linear closure leads to first order differential equations, the solution of which implies an exponential relaxation of the NAPL saturation at long times. That is reminiscent of the dual-porosity solutions obtained while interpreting pumping tests in fractured formations. The associated relaxation time still involves a characteristic diffusion time τ_0 conveniently weighted by a dimensionless shape factor that characterizes the overall matrix block geometrical shape (Landereau et al., 2001).

This chapter is organized as follows: first the phenomena and the governing equation with the generic problem to be solved are presented in Section 3.2. Then in section 3.3, we investigate several popular solutions to capillary imbibition problem to show the need for more consistent solution for both early- and late-times. The results of semi-analytical short-time analysis using Boltzmann transformation are widely reviewed and are adapted to our particular non-linear function in section 3.4. Our original late-time asymptotic solution is presented in section 3.5. The spatial dependence of which can be fully determined analytically, still in the case of a one-dimensional matrix geometry. Those two solutions are compared with numerical simulations carried out at both early- and late-times. in last part, the time variation of the overall flux at the matrix boundary is studied. That allows to set-up a formulation of the exchange term accounting for the non-linearity.

3.2 Driving equations

As briefly mentioned in section 1.1.2, the presence of two or more immiscible fluids in contact with rock introduces new concepts in porous media. Here, we present those principals to derive a mathematical model for counter-current capillary imbibition.

Wettability is defined as the tendency of one fluid to spread on or adhere to a solid surface in the presence of other immiscible fluids. The wettability of the reservoir rock is one of the parameters that controls the distribution of aqueous and non-aqueous phases and affects their movement through pore spaces. Wettability alteration is a process to modify the wettability

and capillary pressure distribution of reservoir rocks to enhance oil production as a tertiary recovery mechanism.

Capillary pressure (P_c) is the pressure difference across the interface between two immiscible fluids arising from the capillary forces. These capillary forces are because of surface tension (the tendency of liquid surfaces at rest to shrink into the minimum surface area possible) and interfacial tension (γ). In continuum scale modeling of immiscible two-phase flow in porous media, the capillary pressure is the difference between the pressure in the non-wetting phase and the pressure in the wetting phase and depends on the saturation. It is defined as:

$$P_c(S) = P_{nw\varphi} - P_{w\varphi} = P_o - P_w, \qquad \text{Eq. 3-1}$$

where, $P_{nw\varphi}$ is the pressure in non-wetting phase and $P_{w\varphi}$ is the pressure in wetting phase. Normally, we assume oil as non-wetting phase and water as wetting in our calculations. S represents mobile aqueous phase saturation that is normalized by irreducible saturations as

$$S(\mathbf{x}, t) = \frac{S_w(\boldsymbol{x}, t) - S_{wi}}{1 - S_{wi} - S_{or}}, \qquad \text{Eq. 3-2}$$

in which, S is the mobile aqueous phase saturation, S_w is total (mobile + immobile) aqueous saturation, S_{wi} is the connate (immobile) aqueous phase saturation, S_{or} is the residual (immobile) non-aqueous phase saturation.

Capillary pressure correlation and wettability variation are very crucial in the modeling of fluid flow in transition zones of fractured reservoirs. Many different experimental or analytical correlations demonstrate the transition zone behavior in different wettability states of the reservoir. However, a simple capillary pressure model presents is represented by Brooks-Corey correlation (Brooks & Corey, 1966):

$$P_c(S) = \frac{P_e}{S^{\frac{1}{m}}}, \qquad \text{Eq. 3-3}$$

in which, P_e is the entry pressure of the porous medium under consideration, and m is a positive exponent represents the pore size distribution index. A simple capillary pressure curve is plotted in Figure 3-1.

Relative Permeability ($k_{r\varphi}$) is the ratio of the permeability to a given fluid phase φ in the presence of other fluid phases to the absolute permeability. While absolute permeability is a constant property of a porous medium related to a single phase flowing, the effective permeability will be strongly tied to phase saturation and the wettability of the medium. Here, $\varphi = w, o$ denote the aqueous and the non-aqueous phase respectively.

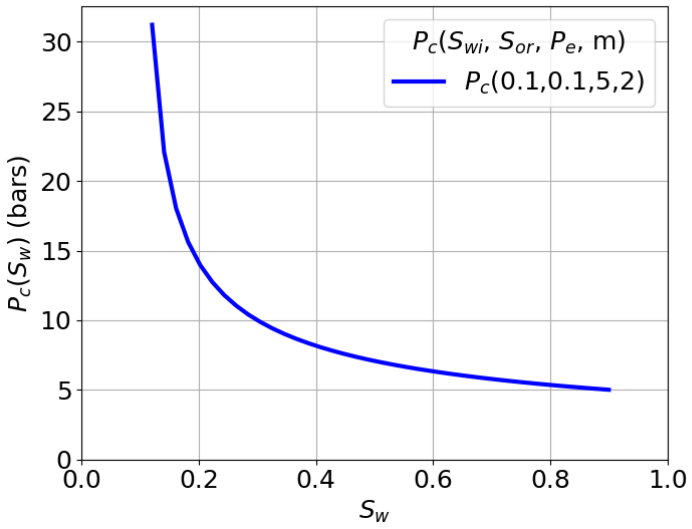


Figure 3-1 A simple example for capillary pressure curve using Corey correlation (Eq. 3-3) with $S_{wi} = 0.1$, $S_{or} = 0.1$, $P_e = 5$ bars, and $m = 2$.

Among all physical parameters and correlations, relative permeability is perhaps the most important constitutive relation that characterizes two-phase flow and displacement processes in porous media. Since no general theoretical expression is available for the relative permeability function, two-phase relative permeabilities are modeled based on another empirical power law model, also known as Brooks-Corey (Brooks & Corey, 1966):

$$k_{rw}(S) = \kappa_w S^p, \qquad \text{Eq. 3-4}$$

$$k_{ro}(S) = \kappa_o (1 - S)^q, \qquad \text{Eq. 3-5}$$

which κ_φ is the maximum relative permeability to phase φ, and p, q are positive exponents (Corey exponents) for the relative permeability curve. For a water-wet system, the oil relative permeability is characterized by an irreducible water saturation S_{wi} of 30% or higher, a Corey exponent q around 2-3 and an end-point relative permeability κ_o around 0.6-0.8. The corresponding water relative permeability is characterized by a residual oil saturation S_{or} of some 10%, a large Corey exponent p around 4-6 and an end-point relative permeability κ_w

around 0.1-0.4. For an oil-wet system water and oil exchange places. Several relative permeability forms with different saturation exponents are presented in this chapter. Figure 3-2 shows an example of the relative permeability values based on S_w.

While specifying relative permeabilities and capillary pressure, saturation dependence is certainly a restriction, it should be noted that Brooks and Corey relationships are widely used for many rock types.

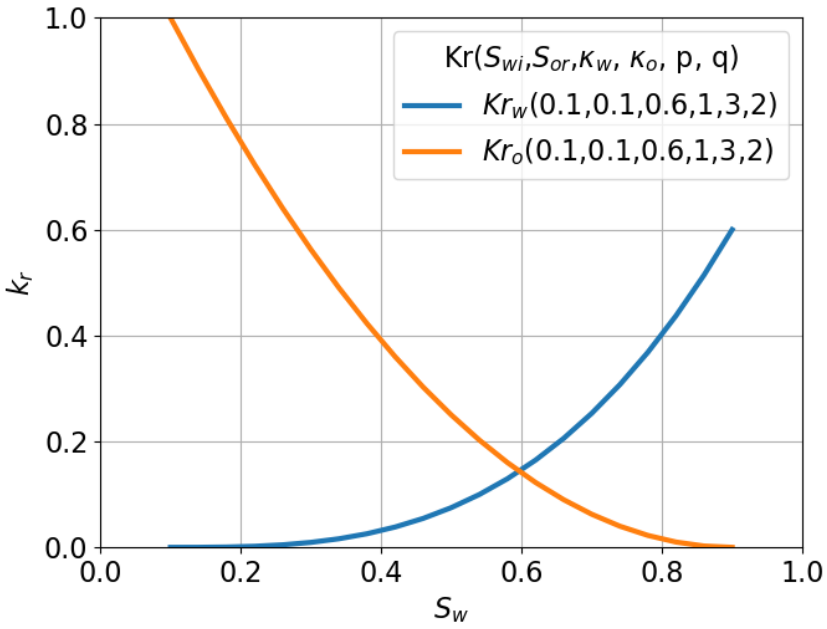


Figure 3-2 Example of Relative Permeability curve with $S_{wi} = 0.1$, $S_{or} = 0.1$, $\kappa_w = 0.6$, $\kappa_o = 1$, $p = 3$, $q = 2$.

In the next sections, we derive a mathematical model for a counter-current capillary imbibition using the properties above in the general three-dimensional form and in simplified one-dimensional condition. Then, we discuss the behavior of the non-linear diffusion coefficient. Finally, we suggest a numerical scheme to solve this non-linear problem for comparison with our analytical solutions.

3.2.1 Driving forces involved in matrix-fracture transfers to consider capillary imbibition

In a fracture network of fractured porous media where flow is taking place, the exchange interaction with the matrix blocks delineated by the fracture network, as sketched in Figure 1-2, involves four forces: gravity, viscous forces, capillarity and molecular diffusion. In the

following (modelling of capillary imbibition transfer), we will assume on the one hand that the molecular diffusion flux, which are by far the weakest, are negligible. On the other hand, we consider such a high permeability contrast between the fractures and the matrix that the overall pressure gradient $\frac{\Delta P}{L}$ acting on one matrix block through the fracture is very low. The capillary number (Ca) is the ratio of the typical viscous force to the typical capillary force can be expressed as $Ca = \frac{\left(\frac{\Delta P}{L}\right)_m k_m}{\gamma\, cos\theta}$, among many propositions (Guo et al., 2022; Lake, 1989), where γ is the interfacial tension between water and NAPL, θ is the contact angle. Assuming $\left(\frac{\Delta P}{L}\right)_m \sim 10^5 \frac{N}{m^3}$, $\gamma = 3 - 4 \times 10^{-2} \frac{N}{m}$, $\theta = \pi/3$ and $k_m = 10\, md$ results in a very low value of $Ca \ll 10^{-5}$, which indicates viscous forces inside the matrix block are negligible. This leaves capillarity and gravity as dominant forces.

The capillary length is defined as the length beyond which gravity becomes important (Gennes et al., 2004). in porous media, it can be estimated by comparing the Laplace pressure $(2\gamma\, cos\theta)/R$, where R is the characteristic capillary tube radius of the equivalent porous medium represented as a bundle of capillary tubes, to the gravity-driven hydrostatic pressure $\Delta\rho g h$, where $\Delta\rho = \rho_w - \rho_o$ is the density difference between water and NAPL, h denotes the matrix block height and g the gravity acceleration. Equating these two pressures, setting $R = \sqrt{8k_m/\phi_m}$, defines the capillary length

$$l_{cap} = \frac{2\gamma\, cos\theta}{\Delta\rho g R} = \frac{\gamma\, cos\theta\, \sqrt{\phi_m}}{\Delta\rho g \sqrt{2k_m}}. \qquad \text{Eq. 3-6}$$

This capillary length, which corresponds to a block height such that gravity and capillary forces are balanced, i.e., a unit Bond number

$$\text{Bo} = \frac{\Delta\rho g h R}{2\gamma\, cos\theta} = \frac{\Delta\rho g h \sqrt{2k_m}}{\gamma\, cos\theta\, \sqrt{\phi_m}} = \frac{h}{l_{cap}}, \qquad \text{Eq. 3-7}$$

defines two regimes depending on whether $\text{Bo} > 1$ or $Bo < 1$. Gravity is negligible for block height $h \ll l_{cap}$ ($Bo \ll 1$). When this condition is met, it is as if the fluid is in a zero- gravity environment and capillary effect dominate. The opposite case, when $h \gg l_{cap}$ is referred to as the gravity regime ($Bo \gg 1$).

In what follows we consider only the capillary regime, that is rock-fluid configurations such that the block height is much lower than the capillary length, $h \ll l_{cap}$. For instance, assuming NAPL is a light oil, $\phi_m = 0.2$, $k_m = 10\ md$, and $\theta = \pi/3$, one gets a capillary length of about $l_{cap} \approx 6 - 12\ m$ depending on temperature and pressure conditions. Basically, we are considering blocks of small height of the order of a few tens of centimeters to one meter.

3.2.2 Counter-current imbibition in the three-dimensional incompressible two-phase flow case without gravity

To derive spontaneous capillary imbibition in porous media, we start with general consideration about three-dimensional, two-phase flow of incompressible fluids without gravity. It is useful to introduce the concept of global pressure P_t that depends implicitly on position **x** and time t introduced by (Guy Chavent & Jerome Jaffre, 1986):

$$P_t = P_w + \int_{S_i}^{S} \frac{\lambda_o}{\lambda_t} \frac{dP_c}{dS'}\, dS', \qquad \text{Eq. 3-8}$$

where $\lambda_\varphi(S) = k_{r\varphi}(S)/\mu_\varphi$ is the phase φ mobility and $\lambda_t = \lambda_w + \lambda_o$ is the total mobility.

The global pressure is defined up to an arbitrary constant which is accounted for by choosing S_i that is an arbitrary saturation value in [0,1]. Following the generalized two-phase Darcy's laws from (Barenblatt et al., 1990), with some algebraic manipulation, the driving equations of 2-2 to 2-5 and above can be transformed as:

$$\nabla \cdot \boldsymbol{u}_t = 0, \qquad \text{Eq. 3-9}$$

$$\boldsymbol{u}_t = -k\lambda_t \nabla P_t, \qquad \text{Eq. 3-10}$$

$$\phi \frac{\partial S_w}{\partial t} + \nabla \cdot \left(\frac{\lambda_w}{\lambda_t} \boldsymbol{u}_t + k \frac{\lambda_w \lambda_o}{\lambda_t} \nabla P_c \right) = 0, \qquad \text{Eq. 3-11}$$

where $\boldsymbol{u}_t = \boldsymbol{u}_w + \boldsymbol{u}_o$ denotes the total Darcy velocity, with $\boldsymbol{u}_\varphi = -k\lambda_\varphi \nabla P_\varphi$ and $\varphi = w, o$. It can be noticed that $\lambda_t \nabla P_t = \lambda_w \nabla P_w + \lambda_o \nabla P_o$. The global pressure may be interpreted as a pressure which would give, for a fictitious fluid with mobility λ_t equal to the sum of the mobilities of aqueous and non-aqueous phases, a flux equal to the sum of the flux of the aqueous and non-aqueous phases.

The above algebraic manipulation for water–oil two-phase system includes two pressure equations obtained after substitution of Darcy's velocity of each fluid phase into the individual mass balance equations. This pressure-pressure system of equations can be transformed into a pressure–saturation form by using the relationship between the capillary pressure which is the difference between the phase pressures and the saturation. The pressure of the second phase can then be removed by expressing it in terms of the saturation and pressure of the other phase. This latter approach is useful when phase disappearance occurs, and the saturation of that phase becomes zero. We will see that the system of partial differential equations describing two-phase flow is highly nonlinear due to the nature of the permeability and capillary pressure functions.

Combining Eq. 3-9 and Eq. 3-10, one is led to solve a quasi-Laplace equation that reads: $\nabla \cdot (k\lambda_t \nabla P_t) = 0$ to be solved on the matrix domain with given boundary conditions. Imposing the rather general block counter-current capillary imbibition boundary conditions at the boundaries of the block, i.e., uniform pressure and saturation, we obtain that the global pressure P_t is uniform at the block boundaries. Thus, it can be shown that the unique solution of the quasi-Laplace equation fulfilling these boundary conditions is a constant: P_t does not depend on position. Therefore, the total velocity vanishes: $\boldsymbol{u}_t = 0$. This result requires the absence of gravity effects, incompressible fluids, and the matrix permeability k may be heterogeneous.

Generally, one can assume two types of spontaneous imbibition: co-current and counter-current. In counter-current flow, in contrast, the matrix is initially surrounded by water and oil can only be displaced by moving in the opposite direction; the total velocity is zero. In co-current flow case, the imbibing phase (water) enters the inlet and pushes the non-wetting phase (oil) to escape from the opposite end. In fact, both co- and counter- current happen in different ratio during the process. Note that in experimental studies, one introduces a semi-permeable membrane, permeable only to the wetting water phase, at the inlet controlling the backflow of oil. The counter-current imbibition attracted far more attention than co-current imbibition because experiments with the boundary condition of matrix block fully covered by water is easier to carry out (Mason and Morrow, 2013). When the matrix blocks are fully covered by water, oil can only be produced by counter-current imbibition and when the matrix blocks are partially covered by water, oil can be produced by combining co- and counter-current imbibition (Hatiboglu & Babadagli, 2010);(Pooladi-Darvish & Firoozabadi, 2000).

Setting $\boldsymbol{u}_t = 0$ in Eq. 3-11 imposes that the saturation is driven by the following non-linear diffusion equation:

$$\phi \frac{\partial S_w}{\partial t} + \nabla \cdot \left(\frac{k \lambda_w \lambda_o}{\lambda_t} \nabla P_c \right) = 0, \qquad \text{Eq. 3-12}$$

based on the chain rule, we can simplify to:

$$\frac{\partial S}{\partial t} = \nabla \cdot [D(S) \nabla S], \qquad \text{Eq. 3-13}$$

with

$$D(S) = -\frac{k}{\phi(1 - S_{wi} - S_{or})} \frac{\lambda_w(S) \lambda_o(S)}{\lambda_t(S)} \frac{dP_c(S)}{dS} \qquad \text{Eq. 3-14}$$

That result shows that counter-current imbibition is not restricted to one-dimensional cases. Up to our knowledge, that result as well as its direct derivation introducing the global pressure for 2D or 3D situations under quite general conditions appear to be original and shows this non-linear diffusion equation is likely to describe the water saturation evolution in many situations of interest.

3.2.3 Driving equations in the one-dimensional case

Spontaneous counter-current capillary imbibition of a one-dimensional matricial porous medium block of size L initially saturated with a non-aqueous phase that is drowned in water can be described, neglecting gravity and assuming the two phases are incompressible, as the non-linear diffusion Eq. 3-14 for the normalized mobile aqueous phase saturation.

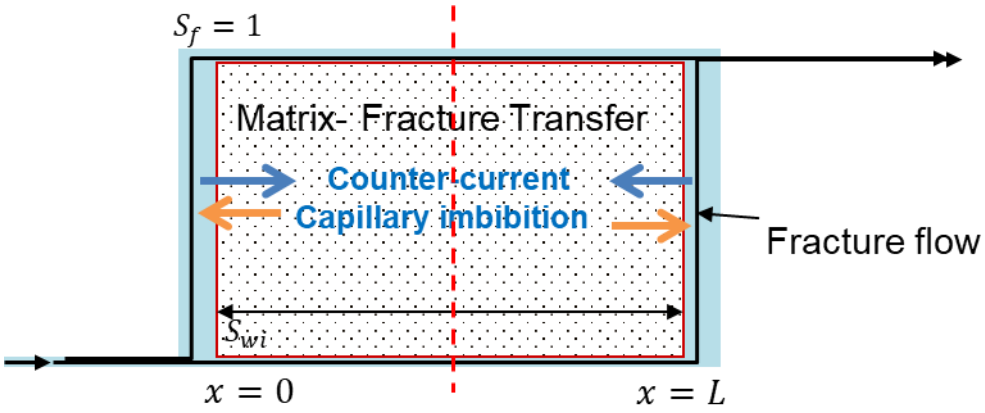


Figure 3-3 Schematic of the simple matrix block surrounded by the fracture saturated by two immiscible phases. Pure spontaneous capillary imbibition in the *x*-direction is considered for matrix-fracture transfer. A symmetry at the middle of block when the flow happens at $x = 0$ and $x = L$ with a same boundary condition.

As shown in Figure 3-3, we introduce initial and boundary conditions as:

$$\begin{cases} S(x,t) = S_f = 1 & (x = 0,\ t > 0) \\ S(x,t) = S_f = 1 & (x = L,\ t > 0), \\ S(x,t) = 0 & (0 < x < L,\ t = 0) \end{cases} \quad \text{Eq. 3-15}$$

where again S_f is the mobile water saturation in the fracture. Because of the symmetry in the assumed block, we can also model half of the block by considering a no flow boundary at $x = L/2$.

3.2.4 Analyzing the non-linear diffusion coefficient of counter-current capillary imbibition transfer

In order to analyze the early- and late-time behaviors, we express $D(S)$ (in Eq. 3-14), the **capillary dispersivity**, as a function of the mobile aqueous phase saturation S (mobile non-aqueous phase's saturation being $1 - S$) setting the relative permeabilities to the aqueous and non-aqueous phases and the capillary pressure as Brooks-Corey saturation power laws. Th obtained $D(S)$ is a nonlinear function of water saturation and usually has a skewed bell-shape curve. The bell-shaped diffusivity has a value of zero at $S = 0$ and $S = 1$ and takes its maximum value somewhere between the end points. The kinetics is proportional to the value of a "capillary" diffusion coefficient. Also, note that the maximum values of this coefficient $\sim 10^{-7}$ to 10^{-6} is four to five orders of magnitude larger than the molecular diffusion coefficient in the single-phase transfer. Figure 3-4 presents several $D(S)$ corresponding to the capillary pressure and relative permeability formulations above without immobile phase saturations. The exponents change the curvature of the plot, and parameters present values of the diffusion while the mobility ratio controls the symmetry of the curve.

Note that, it does not matter what the choice of P_c and $k_{r\varphi}$ is as long as a power-law behavior is obtained at long times for $S \to 1$ (this last statement is less true regarding the early-time regime, which is not the major contribution of this study, as it is discussed later). We highlight this by making a more versatile choice, later at the end of this section.

The diffusion coefficient given in Eq. 3-14 then rewrites:

$$D(S) = D_0 \frac{S^r (1-S)^q}{MS^p + (1-S)^q} = D_1 \frac{S^r (1-S)^q}{S^p + \frac{1}{M}(1-S)^q}, \quad \text{Eq. 3-16}$$

with,

$$D_0 = \frac{k\kappa_w P_e}{m\phi\mu_w(1-S_{wi}-S_{or})}, \quad D_1 = \frac{D_0}{M}, \quad M = \frac{\lambda_w(S=1)}{\lambda_o(S=0)} = \frac{\kappa_w\mu_o}{\kappa_o\mu_w}, \quad r = p - \frac{m+1}{m}, \qquad \text{Eq. 3-17}$$

where M denotes the end-point mobility ratio between the aqueous and the non-aqueous phases, defined as the maximum aqueous phase mobility k_{rw}/μ_w, taken at $S = 1$, and the maximum non-aqueous phase mobility k_{ro}/μ_o, taken at $S = 0$.

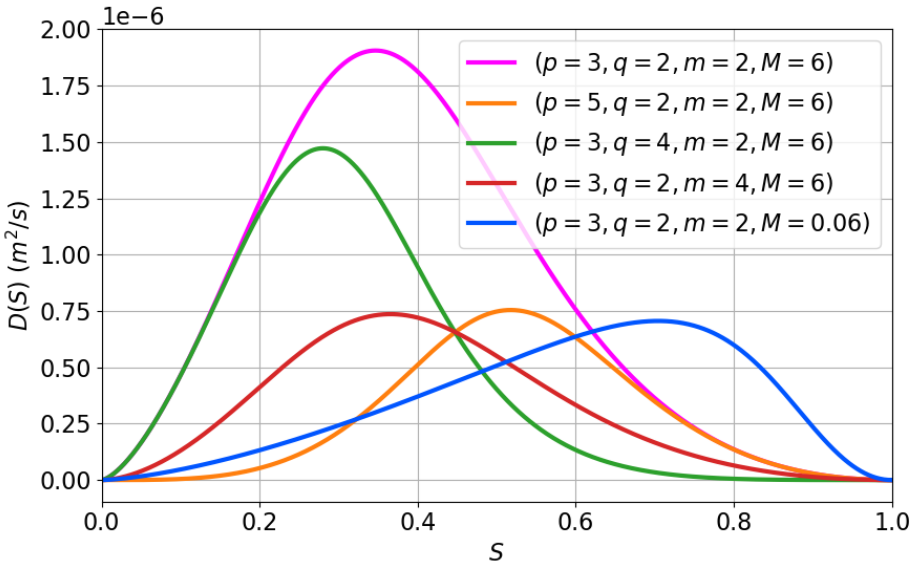


Figure 3-4 Several examples of $D(S)$ given by Eq. 3-14 with $k = 10$ md, $\phi = 0.25$, $P_e = 5$ bar, $S_{wi} = S_{orw} = 0$, and different exponents and mobility ratios mentioned in the legend. The diffusivity is very low at very low and very high saturation and the relative permeability and capillary pressure exponent can control the diffusion transfer.

It is worth noting that Eq. 3-13 is of singular type for $r > 0$ or $q > 0$ because $D(S)$ cancels with either the aqueous phase mobility for $S = 0$ or the non-aqueous phase mobility for $S = 1$. It means that mathematical singularities can be expected near the boundary where $D \to 0$ for $S \to 0$, as well as in the long-time limit inside the rock for which $D \to 0$ for $S \to 1$. A singular regime can be expected at very short times too, due to the sharp jump of the water saturation from 1 to 0 near the boundary.

Clearly, the balance of forces at play that lies in a capillary pressure difference between the fracture (where $P_c = 0$) and the matrix (where $P_c \neq 0$) media commands that a flow is established and terminates when the equilibrium condition $P_c(S) = 0$ is reached, i.e. $S(x,t) = 0$ or $S_w(x,t) = 1 - S_{orw}$. Note that, a non-zero solution of Eq. 3-13 should satisfy the boundary condition $(\partial S/\partial x)_{x=0} = -\infty$ and therefore present a vertical asymptote at the front face of the

porous medium. Indeed, this is a necessary condition to get a non-zero fracture-to-matrix flux $(D(S)\,\partial S/\partial x)_{x=0}$ while D cancels at the boundary.

Thereafter, two limiting cases are particularly useful to consider: on the one hand the case where $S \to 0$, which corresponds to the early-time counter-current spontaneous imbibition of the non-aqueous-phase-saturated block by an aqueous phase, and on the other hand the case where $S \to 1$, which corresponds to the late-time imbibition of the same type. For two the limiting saturations, $D(S)$ behaves asymptotically as:

$$D(S) \approx \begin{cases} D_0 S^{\alpha_0} & with\ \alpha_0 = r,\ for\ S \to 0 \\ D_1 (1-S)^{\alpha_1} & with\ \alpha_1 = q, for\ S \to 1 \end{cases}. \qquad \text{Eq. 3-18}$$

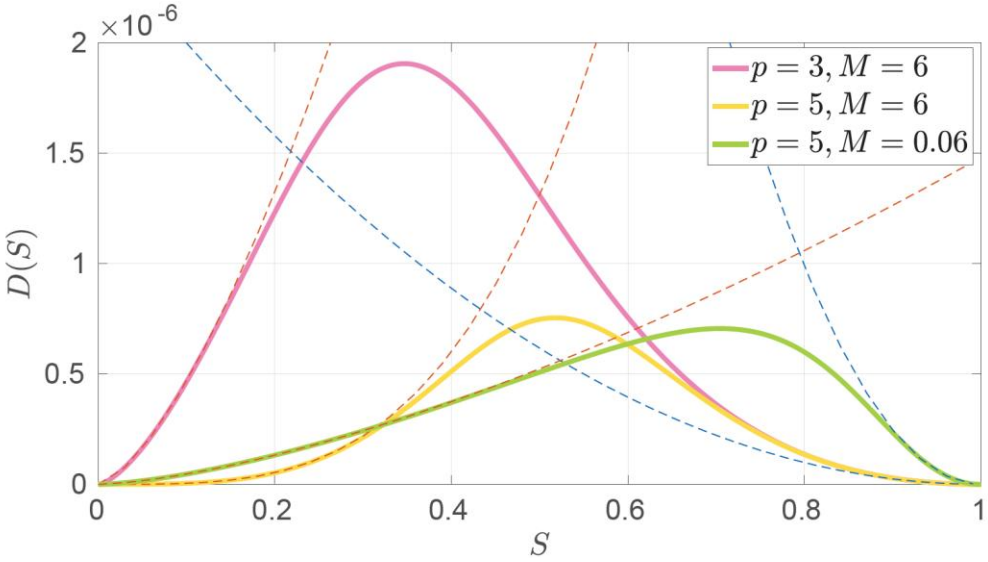


Figure 3-5 Several $D(S)$ given by Eq. 3-14 for $p = 3$, 5 and $M = 6$, 0.06 with $q = 2$, $m = 2$, $k = 10$ mD, $P_e = 5$ bar, $\phi = 0.25$, $S_{wi} = S_{orw} = 0$. Asymptotic power laws for the extreme saturations given by Eq. 3-18 are reported as dashed lines.

Thus, each of these two limiting cases reduces to a non-linear diffusion equation of the singular type with a power law $D(S)$. Specifically, one gets for $S \to 0$

$$\frac{\partial S}{\partial t} = \frac{\partial}{\partial x}\left(D_0 S^{\alpha_0} \frac{\partial S}{\partial x}\right), \qquad \text{Eq. 3-19}$$

and for $S \to 1$

$$\frac{\partial (1-S)}{\partial t} = \frac{\partial}{\partial x}\left[D_1 (1-S)^{\alpha_1} \frac{\partial (1-S)}{\partial x}\right], \qquad \text{Eq. 3-20}$$

where $D_{0,1}$ and $\alpha_{0,1}$ are given in Eq. 3-16 to Eq. 3-18. Here, some examples of full diffusion function and power law limiting cases for extreme saturations are presented in Figure 3-5. The accuracy of these power law simplification to model a capillary imbibition transfer in early and late times is a crucial question to be answered in this chapter.

Coming back to the general case, considering a matrix block Ω of boundary $\partial\Omega$ with initial boundary value problem $S(x,t) = 0$ in Ω for $t = 0$ and $S(x,t) = 1$ on $\partial\Omega$ for all $t \geq 0$, Eq. 3-19 and Eq. 3-20 read respectively

$$\frac{\partial S}{\partial t} = \nabla \cdot (D_0 S^{\alpha_0} \nabla S), \qquad \text{Eq. 3-21}$$

$$\frac{\partial (1-S)}{\partial t} = \nabla \cdot [D_1 (1-S)^{\alpha_1} \nabla (1-S)]. \qquad \text{Eq. 3-22}$$

Given the initial boundary value problem under investigation, the late-time regime has an obvious true limit $S \to 1$ when $t \to \infty$, the early-time regime has a more subtle behavior since the initial condition corresponds to a jump at $x = 0$ because of the boundary condition $S = 1$ and the initial condition $S = 0$. As a consequence, any series solution will feature a full spectrum of saturation functions. We come back to this point later on.

To finish with, it is worth noting that relationships Eq. 3-18 to Eq. 3-20 still hold when considering more versatile relative permeabilities such as

$$k_{rw}(S) = \kappa_w \frac{S^p}{S^p + \beta(1-S)^u}, \qquad \text{Eq. 3-23}$$

$$k_{ro}(S) = \kappa_o \frac{(1-S)^q}{(1-S)^q + \gamma S^v}. \qquad \text{Eq. 3-24}$$

In this case one gets

$$D(S) = D_0 \frac{S^{p-\frac{m+1}{m}}(1-S)^q}{MS^p[(1-S)^q + \gamma S^v] + (1-S)^q[S^p + \beta(1-S)^u]}, \qquad \text{Eq. 3-25}$$

hence, $D(S) \sim D_0 S^{p-\frac{m+1}{m}}/\beta$ for $S \to 0$ and $D(S) \sim D_0(1-S)^q/(M\gamma)$ for $S \to 1$, which is precisely Eq. 3-18 up to the dimensionless constants β and γ. Although this type of correlation has no physical basis, unlike power-law relative permeabilities Eq. 3-4 and Eq. 3-5 which can

be derived by analogy with a bundle of capillary tubes (Burdine, 1953; Purcell, 1949; Rose; Standing, 1975; Wyllie & Gardner, 1958b, 1958a; Wyllie & Rose, 1950; Wyllie & Spangler, 1952), it can nevertheless be useful when considering natural porous media for which power laws are not good enough to match measurements. Also, the capillary pressure with the initial form of Eq. 3-3 is very simple and generic. We can assume a more realistic form of capillary pressure for our model to include different types of rock/fluid properties. However, our starting point (the simple forms of capillary pressure and relative permeability) is thus relatively general and is valid as long as an asymptotic power-law behaviour is obtained at the extreme saturations, independently of any detail at intermediate saturation values and regardless of any empirical correlation used.

3.2.5 Numerical fine-grid simulations

In order to verify analytical and experimental solutions and to check our findings in this chapter, we have developed numerical simulations that will be later validated using our analytical solutions. More details about the discretization of the singular non-linear problem given in Eq. 3-13 to Eq. 3-17 are provided in Annex C.

The numerical model is developed for one-dimensional, two dimensional quadrangle and cylinder and three-dimensional sphere. The physical one-dimensional domain is the interval $[0, L]$ discretized with about one thousand cells, to be sure that solution is very accurate (a convergence study similar to single-phase and not detailed here has been performed). The boundary conditions read $S(x = 0, t) = S(x = L, t) = 1$ for all $t \geq 0$. Due to the symmetry of the problem at hands $x = L/2$, we consider half the domain $[0, L/2]$ with boundary conditions $S(x = 0, t) = 1$ and $(\partial S/\partial x)(x = L/2, t) = 0$ for all $t \geq 0$. Annex C provides more details on higher dimension models.

Before developing our analytical approximation to this problem, we try to give some of the solutions available in the literature for this problem in section 3.3, and we compare some of them with available numerical results.

3.3 Some previous solutions to the capillary imbibition problem

Spontaneous counter-current imbibition is mathematically described by a non-linear diffusion equation (Eq. 3-13). Finding analytical solutions that are valid at early and late times

has been an open challenge for many years. Meanwhile, previous studies have presented different solution methodologies based on different types of simplification.

3.3.1 Specific form of capillary diffusion coefficient

The idea of using a constant diffusion coefficient (called equivalent diffusivity constant, D_e) for a counter-current capillary imbibition was mentioned by (Bekner et al., 1987) where they validated the method based on (Kleppe & Morse, 1974) experimental system. If D_e is assumed as a constant value, then analytical solutions of the diffusion equation (Eq. 3-13) are very similar to the pressure diffusivity solutions, presented in chapter 2. Beckner carried numerical simulations with constant capillary diffusion coefficient and fine-grid exact solution comparing to a specific reported experiment of injected capillary imbibition.

(Bech et al., 1991) tried the concept of taking a constant D_e and claimed that using a constant diffusivity equal to the maximum of $D(S)$ is sufficient to match results of fine-grid simulations and the experimental data of (Bourbiaux & Kalaydjian, 1990). However, that method was not generalized for other cases or to any arbitrary non-linear diffusion coefficient.

Later, (Saboorian-Jooybari et al., 2012) developed a transient (i.e. time–dependent) shape factor similar to Eq. 2-16 for the counter-current capillary imbibition from an analytical solution of the corresponding diffusion equation that describes the mechanism. This was possible thanks to the adoption of a constant D_e instead of the variable capillary diffusion coefficient in Eq. 3-13. However, (Chevalier et al., 2019) experimentally showed that the assumption of a constant equivalent diffusion coefficient is a significant simplification and demands further examination.

We have investigated the technique of constant equivalent value of capillary diffusion with our numerical case studies. These numerical solutions are applied to the convergence study and are benchmarked against very early/late times solutions later in this study. The constant diffusion coefficient we can obtain from the first case in Figure 3-5 ($p = 3, q = 2, M = 6$) are 1.9×10^{-6} and 7.94×10^{-7} for maximum and average of $D(S)$ respectively. That assumption gives a good early times approximation in specific cases, particularly with intermediate wettability. However, as it is shown in Figure 3-6, the analytical solution (Eq. 2-10) with an equivalent constant diffusion coefficient is not valid at late-times for most non-linear cases.

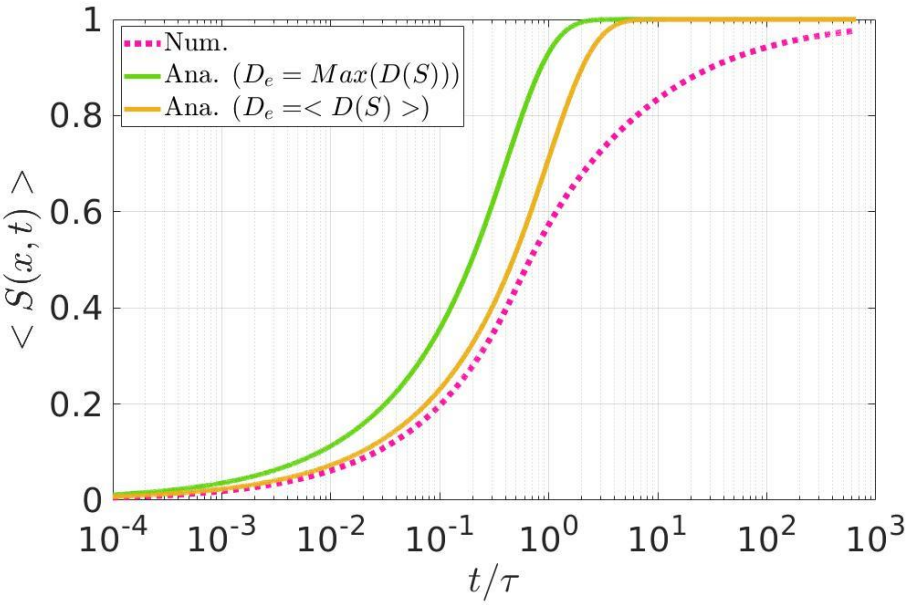


Figure 3-6 Comparison between analytical solution of a capillary imbibition diffusion problem with constant equivalent diffusion coefficients (solid lines calculated from Eq.2-10) and numerical solution of full non-linear diffusion problem (dashed line), the time is scaled by $\tau = L^2/(4D_{Max})$.

Several other studies tried to simplify or re-formulate $D(S)$ rather than over-simplifying to a constant value. For example, (Bluman & Kumei, 1980) presented an analytical solution to the diffusion equation assuming $D(S) = a(S+b)^{-2}$, with a and b as two arbitrary constants. But, this form of the diffusion coefficient is not realistic. Another diffusion problem assumes that D, has a power law dependence on local concentration (Heaslet & Alksne, 1961) and will be more discussed in the next part.

(Kashchiev & Firoozabadi, 2003) tried to fit the actual diffusion function to another specific form of $D(S) = D_0 S^m \exp(-cS^n)$, in which m and n are two free positive parameters, while D_0 and c are related to maximum diffusion and saturation. However, the explicit approximation of $S(x,t)$ is derived and compared to numerical calculation; only for a particular case.

Also, these solutions depend on expressing the functions of the capillary pressure and relative permeabilities on saturation in specific forms; consequently, the equations that are solved are approximations to the equations that apply to the original problem.

3.3.2 Semi-infinite solutions

(McWhorter & Sunada, 1990) proposed an integral solution of (Buckley & Leverett, 1942) fractional flow under arbitrary capillary functions in linear and radial systems. Unlike other solutions that assume specific functional forms of the relative permeabilities and capillary pressures, the saturation-dependent functions in the McWhorter and Sunada solution are completely arbitrary. However, a numerical computation was applied to obtain the final integration. The main assumption in the McWhorter and Sunada solution is that the imbibition rate, for both co- and counter-current flow, is inversely proportional to the square root of time. They expressed the solutions to the diffusion type imbibition as **self-similar behavior** or **Boundary layer behavior**. The well-known similarity solution was firstly introduced by (Boltzmann, 1894), (Klute, 1952), and (Philip, 1955a). When the driving force is simply the capillary pressure, which remains fixed for a given saturation, the saturation profile must simply stretch along the x-direction with time. The distance traveled by a given saturation value is proportional to $\sqrt{t}$. Then a very common change of variable for self-similar behavior in infinite acting is $\propto \frac{x}{\sqrt{t}}$. We use this change of variable in our infinite acting flow solution at early times in the next section. Some drawbacks of the McWhorter and Sunada solution is discussed by (Z.-X. Chen et al., 1992); (J. Chen et al., 1995).

Likewise, (Ruth et al., 2007) presented an iterative, series solution of an integral-differential equation to describe the counter-current imbibition process with arbitrary capillary pressure and relative permeability, and constant boundary saturation. Their calculations showed rather good agreement with numerical and experimental results. Again, this similarity solution is valid for early times with self-similar behavior with specific assumption and approximations. (Alyafei et al., 2016; Blunt, 2017; Nooruddin & Blunt, 2016; Schmid et al., 2016) among all, worked on this **semi-analytical** solution.

Scaling (characteristic) groups are expressions of parameters that characterize the effect of key parameters on capillary imbibition transfer time. For example, they are a central tool for normalization or interpretation of laboratory data and up-scaling them to field conditions. There are two ways to derive scaling groups for Capillary Imbibition in porous media. Either a curve fitting applied on a large body of experimental data (presented in next section 3.3.3) or simplifying assumptions on the form of the hydraulic diffusivity function in Darcy's equation (Schmid et al., 2011). (Schmid & Geiger, 2012) proposed a universal scaling

group that incorporates the influence of all parameters on Spontaneous Imbibition that are present in the two-phase Darcy model. This solution imposes McWhorter boundary condition (McWhorter & Sunada, 1990) that specifies the inflow as $F_w(x=0,t)=\frac{A}{\sqrt{t}}$, where A is a constant that shows how fast water spontaneously imbibes and depends on the rock/fluid properties. This scaling group is presented in Table 3-1.

These semi-analytical solutions were based on a transient flow assumption at early times. As the wetting front reaches the boundary of the block (mid-block in Figure 3-3), a late-time behavior appears that is mostly characterized experimentally.

3.3.3 Scaling with experimental analysis

Several studies tried to model and rescale the imbibition flow rate or recovery from different sets of laboratory experiments on small rock samples and, to give a normalization parameter (such as characteristic time, t/τ) to obtain a type-curve for different sets of properties. (Mason & Morrow, 2013) claimed that nearly all advances in understanding and quantifying spontaneous imbibition have resulted from experiments.

(Aronofsky et al., 1958) defined an exponential recovery trend for a complete transfer in a single matrix block:

$$R(t)=1-e^{-\lambda t}, \qquad \text{Eq. 3-26}$$

where, $R(t)$ is the normalized recovery function. The difficulty in the use of this equation is to define the time constant (λ) that controls the rate of recovery.

Several recent studies divided the exponential fitting function into multiple exponential functions with two or three parameters (λ_1, λ_2,…) for early and late times. (Babadagli et al., 2009; Swaan & Ramirez-Villa, 1993; Tavassoli et al., 2005a) among all developed new exponential functions to fit a spontaneous capillary imbibition transfer from matrix to fracture.

Back to scaling group strategy, (Mattax C. C. & Kyte J. R., 1962) performed one-dimensional and three-dimensional imbibition experiments to examine their scaling relations. They showed that the imbibition time of different block size/shape and different fluid properties could be normalized using a dimensionless time (t/τ) mentioned in Table 3-1.

Table 3-1 from (Schmid & Geiger, 2012) summarizes different scaling groups for spontaneous capillary imbibition in porous media. (Abd & Alyafei, 2018) compared and numerically validated the scaling groups suggested in this table. We will propose a new characteristic (dimensionless time scaling) for a non-linear capillary imbibition process in the next section that is obtained from an exact analytical solution. Here, L_c has the physical interpretation of quantifying the average length which a wetting front can travel without meeting a boundary or another imbibition front. The calculation similar to Eq. 2-18 for L_c is explained in (Ma et al., 1997). J is the Leverett function (Leverett, 1941). Obviously, using only wetting phase viscosity is not enough to characterize all cases and other researchers tried to present a more universal expression.

Table 3-1 Some of dimensionless time scaling for the capillary imbibition process [(Schmid & Geiger, 2012)]. More details about the choice of properties can be found in related references.

Author	Dimensionless Time (t/τ)
(Lucas, 1918), (Washburn, 1921)	$\frac{1}{2}\frac{1}{L_c^2} r \frac{\sigma}{\mu_w} t$
(Rapoport, 1955), (Mattax C. C. & Kyte J. R., 1962)	$\frac{1}{L_c^2}\sqrt{\frac{k}{\phi}}\frac{\sigma}{\mu_w} t$
(Ma et al., 1997)	$\frac{1}{L_c^2}\sqrt{\frac{k}{\phi}}\frac{\sigma}{\sqrt{\mu_w \mu_{nw}}} t$
(Zhou et al., 2002)	$\frac{1}{L_c^2}\sqrt{\frac{k}{\phi}}\sigma\left(\frac{\lambda_w \lambda_o}{\lambda_w + \lambda_o}\right) t$
(Tavassoli et al., 2005a)	$\frac{1}{L_c^2}\sqrt{\frac{k}{\phi}}\sigma\left(\frac{\lambda_w \lambda_o}{\lambda_w + \lambda_o}\right) J'.t$
(Kewen Li et al., 2006)	$\frac{1}{L_c^2}\sqrt{\frac{k}{\phi}}\sigma\left(\frac{\lambda_w \lambda_o}{\lambda_w + \lambda_o}\right) J'.(S_{BC} - S_{wi})t$
(Schmid & Geiger, 2012)	$\left(\frac{2A_0^*}{\phi L_c}\right)^2 t$
A_0^* is the early time flux pre-factor: $\Phi_{mf} = A_0/\sqrt{t}$ (when $t \to 0$)	

The idea of combining an early-time expression based on a semi-analytical solution with a late-time expression based on the exponential approximation was suggested by (J. Chen et al., 1995) and later in (Tavassoli et al., 2005a). Both authors assumed that the transition between early and late time occurs when the semi-analytical solution ceases to be valid. That is, when the wetting phase front reaches the no-flow boundary of the domain (mid-block in our model). (March et al., 2016) worked on combining two different solutions for early times and late times.

They emphasized that the time until which the imbibed volume scales with $\sqrt{t}$ (early-times solution) is significantly **longer** than the time it takes until the imbibition front reaches the model boundary. Combining both solutions require a proper characterization of the transition between the two regimes.

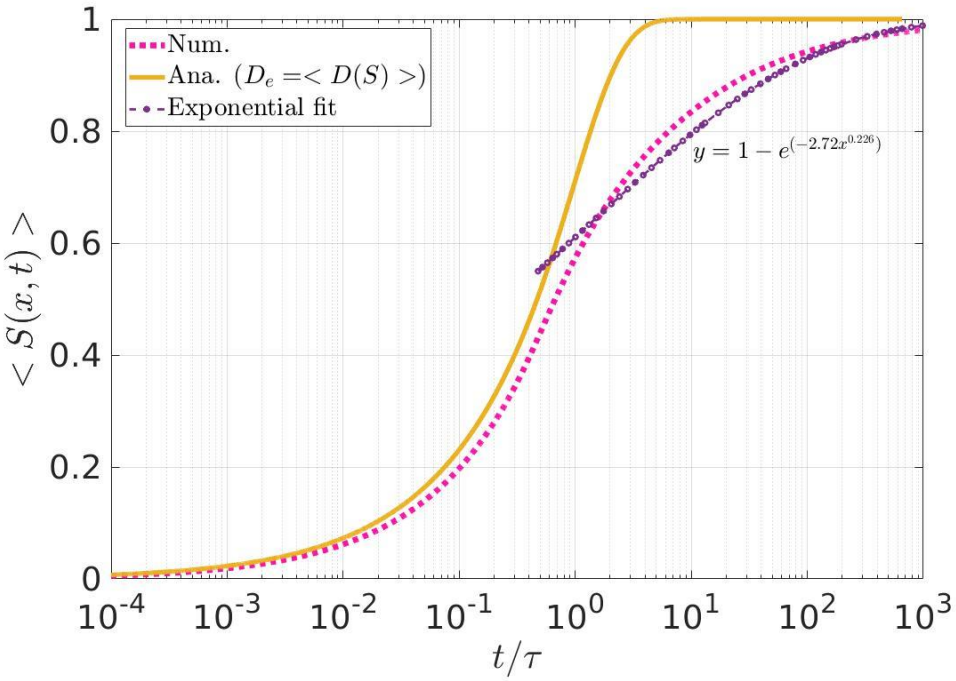


Figure 3-7 Comparison between numerical solution (dashed line) and a hybrid model including analytical solution with constant equivalent diffusion (solid line) for early times plus exponential fit (circle line) for late times, the time is scaled by $\tau = L^2/(4D_{Max})$.

In Figure 3-7, we have used an exponential fit for the late time recovery to suggest a hybrid model beside the early time prediction with constant equivalent diffusion coefficient.

Also, experimental analysis can investigate the role of many other parameters such as block size and shape, boundary condition etc. (Rangel-German & Kovscek, 2006) developed an improved formulation of matrix-fracture transfers driven by filling fracture water imbibition in partly immersed matrix blocks. Their experimental results from CT-scan images have shown that the "filling-fracture" regime has a linear relationship with time, whereas the "instantly-filled fracture" regime has a linear relationship with the square root of time. This can develop our constant fracture boundary condition that is explained in the coming section.

3.4 Early time solution

As mentioned before, the early time flow or transient condition is when the state of the system changes with time. In our problem, it is specified by the period before the front flow reaches the boundary of the block. The literature is very abundant on the short time scale regime that can be assimilated to flow in a semi-infinite medium. We recall some outstanding works of (Heaslet & Alksne, 1961) and (J.-Y. Parlange et al., 1984) that are relatively little cited nowadays, whereas they give very accurate fudge-factor-free solutions and we investigate the best solution for our specific non-linear diffusion coefficient.

In the early-time regime, following the references therein, the idea is to consider that the overall size of the block may be ignored, leading to considering a semi-infinite medium. That suggests using the self-similar behavior and Boltzmann variable $\xi = \frac{x}{\sqrt{4D_0 t}}$ in Eq. 3-13 and yiels the following equation

$$2\xi \frac{dS}{d\xi} + \frac{d}{d\xi}\left(\frac{D(S)}{D_0}\frac{dS}{d\xi}\right) = 0, \qquad \text{Eq. 3-27}$$

with the boundary condition of

$$\begin{cases} S(0) = 1 \\ D(S(\infty))\dfrac{\mathrm{d}S}{\mathrm{d}\xi}(\infty) = S(\infty) = 0 \end{cases}. \qquad \text{Eq. 3-28}$$

A remarkable fact, observed by many authors, (Bruce & Klute, 1956b; Brutsaert, 1968; Brutsaert & Weisman, 1970; Heaslet & Alksne, 1961; J.-Y. Parlange et al., 1984; M. B. Parlange et al., 1992) among all, is that the solution of this equation has a finite toe (which gives flow front indication and can be seen later in the plots) introduced as ξ_0 that depends on the input parameters of the equation.

3.4.1 Power law diffusion function

In this simple case, we assume the extreme behavior of diffusion function at early-times such that $D(S) = D_0\, S^{\alpha_0}$, and $\alpha_0 > 0$. Eq. 3-19 reads:

$$2\xi \frac{dS}{d\xi} + \frac{d^2}{d\xi^2}\left(\frac{S^{\alpha_0+1}}{\alpha_0+1}\right) = 0, \qquad \text{Eq. 3-29}$$

with boundary conditions of

$$\begin{cases} S(0) = 1 \\ S^{\alpha_0}(\infty)\dfrac{\mathrm{d}S}{\mathrm{d}\xi}(\infty) = S(\infty) = 0 \end{cases}. \qquad \text{Eq. 3-30}$$

In the paper of (Heaslet & Alksne, 1961) a complete analytical solution was obtained, that may be expressed under the form:

$$S(\xi) = \begin{cases} [2\alpha_0\xi_0(\xi_0 - \xi)]^{\frac{1}{\alpha_0}} f\left(\dfrac{\xi}{\xi_0}\right) & \text{if } \xi \in [0, \xi_0] \\ 0 & \text{if } \xi > \xi_0 \end{cases}. \qquad \text{Eq. 3-31}$$

Here, the function $f\left(\frac{\xi}{\xi_0}\right)$ is a regular function that may be expressed as the power series below involving the exponent α_0 as a parameter.

$$f\left(\frac{\xi}{\xi_0}\right) = 1 + \sum_{n=1}^{\infty} A_n(\alpha_0)\left(1 - \frac{\xi}{\xi_0}\right)^n. \qquad \text{Eq. 3-32}$$

As mentioned, the solution has the particularity that saturation and flux vanish at a finite critical point of $\xi = \xi_0(\alpha_0)$ and are zero for $\xi \in (\xi_0(\alpha_0), \infty)$. Determination of ξ_0 (toe for front flow solution) follows from the boundary condition $S(\xi = 0) = 1$ which yields:

$$\xi_0 = \frac{1}{\sqrt{2\alpha_0}\left(1 + \sum_{n=1}^{\infty} A_n(\alpha_0)\right)^{\frac{\alpha_0}{2}}} \qquad \text{Eq. 3-33}$$

Heaslet-Alksne solved the nonlinear diffusion equation using a series expansion around the wetting front (ξ_0) for power law diffusivities. The series coefficient $A_n(\alpha_0)$ may be determined systematically with a term by term expansion about front point (ξ_0), and the first four terms are derived as (Heaslet & Alksne, 1961):

$$\begin{aligned} A_1(\alpha_0) &= -\frac{1}{2\alpha_0(\alpha_0 + 1)} \\ A_2(\alpha_0) &= \frac{-2\alpha_0^2 + 3\alpha_0 + 3}{6(2\alpha_0)^2(\alpha_0 + 1)^2(2\alpha_0 + 1)} \\ A_3(\alpha_0) &= \frac{2\alpha_0^3 + 4\alpha_0^2 - \alpha_0 - 1}{6(2\alpha_0)^3(\alpha_0 + 1)^2(2\alpha_0 + 1)(3\alpha_0 + 1)} \\ A_4(\alpha_0) &= \frac{1152\alpha_0^7 + 2056\alpha_0^6 + 588\alpha_0^5 - 994\alpha_0^4 - 735\alpha_0^3 - 45\alpha_0^2 + 75\alpha_0 + 15}{360(2\alpha_0)^4(\alpha_0 + 1)^4(2\alpha_0 + 1)^2(3\alpha_0 + 1)(4\alpha_0 + 1)}. \end{aligned} \qquad \text{Eq. 3-34}$$

Their singular analytical dependence for $\alpha_0 \to 0$ confirms the singular character of the problem at hand. That means that some mathematical difficulties are to be expected close to the limit problem of a standard constant diffusion coefficient case. Coming back to the initial problem, it can be expected that as soon as the toe front is smaller than half medium size, that solution remains valid for finite times.

(Brutsaert, 1968; Brutsaert & Weisman, 1970) proposed an approximation to Eq. 3-31 and mathematical simplification to Heaslet-Alksne solution. The first approximation was derived considering the diffusivities exactly around $S = 1$, which is near the complete saturation, expressed as:

$$S(\xi) \approx \left(1 - 2\xi \left[\frac{(\alpha_0 + 1)^2}{2(\alpha_0 + 2)}\right]^{\frac{1}{2}}\right)^{\frac{1}{\alpha_0 + 1}}. \qquad \text{Eq. 3-35}$$

Also, the second approximation was obtained by solving Eq. 3-29 considering front conditions (Eq. 3-30) and in the neighborhood of $S = 0$ ($\xi = \xi_0$). This is a simplification of Heaslet solution by neglecting the series function in the second squared bracket. Thus, the critical point is estimated as $\xi_0 = (2/\alpha_0)^{1/2}$ and the saturation writes:

$$S(\xi) \approx \left[1 - 2\xi \left(\frac{\alpha_0}{2}\right)^{\frac{1}{2}}\right]^{\frac{1}{\alpha_0}}. \qquad \text{Eq. 3-36}$$

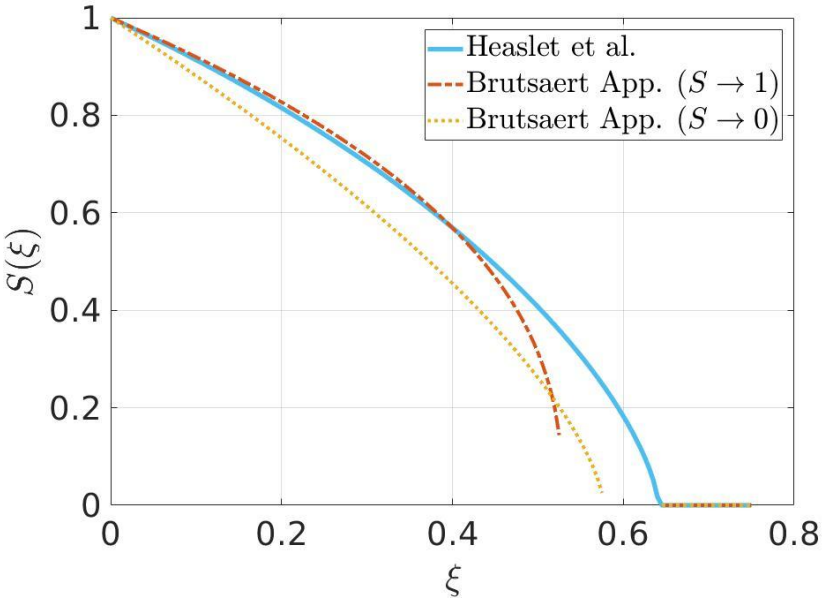


Figure 3-8 Comparison analytical solution and two approximations of non-linear ODE (Eq. 3-29) with power law diffusion function of $D(S) = 1.48 \times 10^{-5} S^{1.5}$

Figure 3-8 shows Heaslet-Alksne analytical solution and two approximations to the power-law diffusivity ODE of Eq. 3-29. Heaslet-Alksne is an exact solution for the power-law diffusion ODE. However, the approximations are not very accurate solutions for a full range of ξ.

(Hristov, 2015, 2016) solved the power-law diffusion equation of 3.4.1 with the integral balance approaches and has benchmarked his solution with Heaslet series solutions (Brutsaert, 1968; Brutsaert & Weisman, 1970; Heaslet & Alksne, 1961) as the references.

We note that the capillary imbibition transfer is not driven by a power law diffusivity equation because in contrary with a simple power law diffusion function, the capillary pressure values decrease to very small values at high saturations. We implemented the numerical solution for the full non-linear diffusion to compare it with the exact analytical solution of a power law problem. Figure 3-9 presents the difference between the exact solution of a power law non-linear diffusion equation and the numerical solution of the bell-shaped capillary imbibition diffusion equation. The comparison indicates that (M. A. Heaslet & A. Alksne, 1961) assumption cannot be implemented for counter-current capillary imbibition transfer and that demands further investigation of possible solution or approximation to the full capillary imbibition diffusion function in the next section.

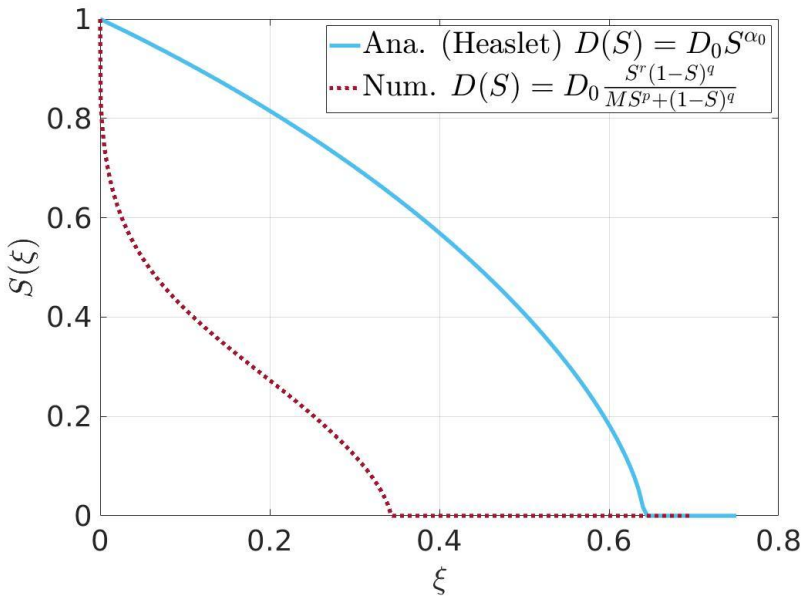


Figure 3-9 Comparison between analytical solution (solid line) of power-law diffusion (Eq. 3-29) and numerical solution (dotted line) of full non-linear diffusion (Eq. 3-13) at early times (semi-infinite flow behavior) with $p = 3$ ($\alpha_0 = 1.5$), $q = 2$, $M = 6$, $= 10$ mD, $P_e = 5$ bar, $\phi = 0.25$, $S_{wi} = S_{orw} = 0$.

3.4.2 General non-linear diffusion function (Parlange extension to Heaslet technique)

The difference between the power-law diffusion function and the bell-shape capillary diffusion function encouraged us to find a better approximation of our problem with more general form of $D(S) = D_0 f(S)$. In order to go further, the saturation dependence of $D(S)$ suggests expressing ξ as a function of S. A further transformation allows us to treat the case of a $D(S)$ function given by Eq. 3-14. (Bruce & Klute, 1956b) described the non-linear diffusion Eq. 3-27 with an implicit equation by integrating with respect to ξ and simplifying.

$$D(S) = -2D_0 \frac{d\xi}{dS} \int_0^S \xi \, dS. \qquad \text{Eq. 3-37}$$

Also, this form assumes the existence of a finite front ξ_0 for which the saturation and the flux, proportional to $D(S)\,\mathrm{d}S/\mathrm{d}\xi$, cancel out.

An iterative sequence of approximations can be built by approximating the right-hand-side Eq. 3-37 integral of which yields, at the **lowest order approximation**:

$$J(S) = \frac{1}{2D_0} \int_0^S \frac{D(S')}{S'} \, dS' \approx \xi_0(\xi_0 - \xi) \qquad \text{Eq. 3-38}$$

(J.-Y. Parlange et al., 1984) reformulated Bruce and Klute expression at the wetting front and developed the first term of a series expansion of the integral expression $\int D(S)/S \; dS$ as the **higher order approximation**. This solution is based on the observation that even though the non-linear diffusivity is a difficult function, its integral is easier to handle. The final implicit form of the solution is obtained as:

$$J(S) = \frac{1}{D_0} \int_0^S \frac{D(U)}{U} dU \approx 2\xi_0(\xi_0 - \xi) - A(\xi_0 - \xi)^2, \qquad \text{Eq. 3-39}$$

with ξ_0 evaluated using the boundary condition $S(\xi = 0) = 1$:

$$\xi_0 = \sqrt{\frac{J(1)}{2 - A}}, \qquad \text{Eq. 3-40}$$

with the coefficient A, defined by:

$$A = \frac{\int_0^{S_0} \frac{(S_0 - V)D(V)}{V} \mathrm{d}V}{S_0 \int_0^{S_0} \frac{D(V)}{V} \mathrm{d}V}. \qquad \text{Eq. 3-41}$$

A is presented like a constant but in fact, is a function of the arbitrary saturation $S_0 \in (0, S]$. Any non-linear function of $D(S)$ can be plugged into Eq. 3-39 and Eq. 3-41. In the case of $D(S) = D_0\, S^{\alpha_0}$, Parlange indicates that $A = 1/(\alpha_0 + 1)$. They claimed this coefficient can be taken as a constant in most cases as one of the steps of the derivation. The coefficient A is not constant for the full $D(S)$, but only for a limited saturation range is equal to $1/(\alpha_0 + 1)$. This is where the full bell-shaped diffusion coefficient could be approximated by power-law function. This saturation range for $A = 1/(\alpha_0 + 1)$ extends as r increases (see Figure 3-10). However, for the general case of Eq. 3-14, A is not a constant and depends on the value of $S_0 \in (0,1]$. Figure 3-10 shows the value of A for different exponent values. The higher is the exponent r ($\alpha_0 = r$), the better is the approximation for Eq. 3-41. Figure 3-10 shows the relation between the coefficient of higher order analytical approximation for two different non-linear diffusion functions: power law $D(S)$ and full bell-shape $D(S)$.

Note that we can consider different values for A as the minimum A_{min} (power-law base value), or its maximum value, A_{Max}, as was done in the original paper (J.-Y. Parlange et al., 1984), or any intermediate value (e.g. average A_{avg}). However, they have chosen a constant A at $x = 0$ where $S_0 = 1$.

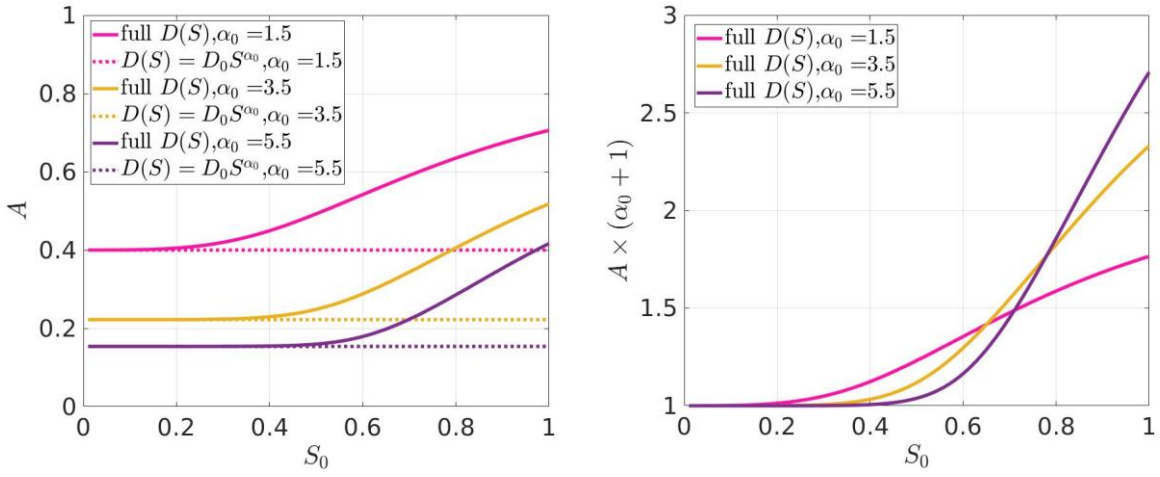


Figure 3-10 Evaluation of A values (the coefficient of higher order approximation of analytical solution of Eq. 3-39) based on Eq. 3-41 for power-law (dotted lines) and general forms (solid lines) of non-linear diffusion function for different values of $p = 3,5,7$ and with $q = 2$, $M = 6$, $= 10$ mD, $P_e = 5$ bar, $\phi = 0.25$, $S_{wi} = S_{orw} = 0$.

Later, (M. B. Parlange et al., 1992) extended Heaslet solution (series expansion around the wetting front) for an arbitrary diffusivity considering only the two first terms of their series expansion. A was obtained as:

$$A = \frac{\left(\frac{\int_0^1 \frac{D}{S} dS}{\int_0^1 D dS}\right)^{1/2} - 1}{\left(\frac{\int_0^1 \frac{D}{S} dS}{\int_0^1 D dS}\right)^{1/2} - \frac{1}{2}}. \qquad \text{Eq. 3-42}$$

They claimed the result with Eq. 3-42 is slightly more accurate than the earlier on of A_{Max} (J.-Y. Parlange et al., 1984) at a constant S (x=0, S=1). Figure 3-11 presents our comparison between the numerical calculation and analytical solution of early times non-linear diffusion with Parlange higher order approximations for the general diffusion function. It compares different proposals of coefficient A to find the best formulation based on our problem. The assumption of the constant A at inlet boundary (A_{Max}) is not the best choice for our problem. We have shown it is more convenient to approximate A at the flow front where the saturation is small and $D(S)$ can be approximated by the power-law function of $D(S) = D_0\, S^{\alpha_0}$. In that case A is simply equal to $A_{1984,min} = 1/(a_0 + 1)$.

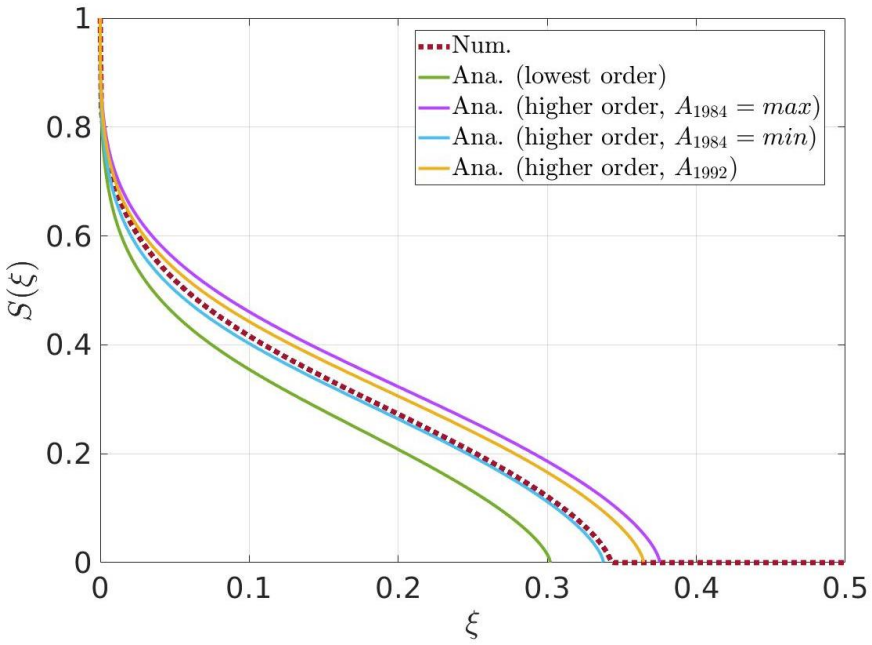


Figure 3-11 Comparison between analytical solution of lowest order approximation and higher order approximations (solid lines) with different choices of coefficient A and numerical solution (dotted line) for non-linear diffusion Eq. 3-13 with $p = 3$ ($\alpha_0 = 1.5$), $q = 2$, $M = 6$, $= 10$ mD, $P_e = 5$ bar, $\phi = 0.25$, $S_{wi} = S_{orw} = 0$.

The solution with two different order of approximation writes as:

$$\frac{1}{2D_0}\int_0^S \frac{D(S')}{S'}dS' \approx \begin{cases} \xi_0(\xi_0-\xi) & (lowest\ order\ approximation) \\ \xi_0(\xi_0-\xi)-\frac{A}{2}(\xi_0-\xi)^2 & (higher\ order\ approximation). \end{cases} \quad \text{Eq. 3-43}$$

The complete early-time diffusion profile thus may be estimated analytically with an excellent accuracy, as reported in Figure 3-12. This plot compares, for a few configurations (of $D(S)$ in Figure 3-5), solution above obtained by setting $A_{1984,min}$ with the numerical calculation obtained with the numerical scheme described. Although the general solution (Eq. 3-43) is not closed form, it requires only straightforward numerical integration of well-defined functions to achieve numerical results. Also, considering the power-law case, the solutions proposed by Parlange et al. are consistent with the findings of Heaslet.

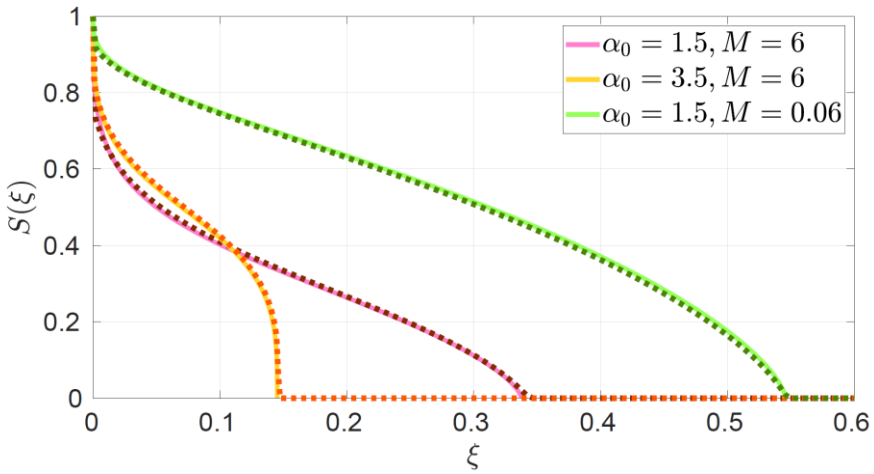


Figure 3-12 Comparison of early-time analytical solution given in Eq. 3-43 (solid lines) with the simulated one (dotted lines) for $\alpha_0 = 1.5, 3.5$ (p = 3, 5) and M = 6, 0.06 with q = 2, m = 2, k = 10 mD, $P_e = 5$ bar, $\phi = 0.25$, $S_{wi} = S_{orw} = 0$.

Saturation presents a vertical asymptote at the boundary face of the porous medium for $x = \xi = 0$ because a non-zero fracture-to-matrix flux $D(S)\,\partial S/\partial x = (D(S)/\sqrt{4D_0 t})\,\mathrm{d}S/\mathrm{d}\xi$ while $D(S) = 0$ for $S = 1$ at the boundary is only possible if $\partial S/\partial x = \mathrm{d}S/\mathrm{d}\xi = -\infty$. Flux vanishes as well at the toe position ($\xi = \xi_0$) where $\mathrm{d}S/\mathrm{d}\xi = -2\xi_0[2\alpha_0\xi_0(\xi_0-\xi)]^{(1-\alpha_0)/\alpha_0} \sim 1/(\xi_0-\xi)^{(\alpha_0-1)/\alpha_0}$, therefore the larger α_0 the sharper the front as can be seen in Figure 3-12. The new general approximation captures better the capillary imbibition diffusion problem. However, finding more terms of series expansion will result in more accurate solution. To finish with, dimensional analysis suggests normalizing the timescale by the diffusion time $\tau_0 = L^2/(4D_0)$. Following our work objective, expressions for the matrix-to-fracture exchange term

are investigated in Section 3.6. Before that, we have to look at late-times where the wetting phase is saturated in the block matrix.

3.5 Late time solution

Now, we focus on the late-time regime solution, for which the medium can no longer be assumed to be semi-infinite, and for which we have not found, to their best knowledge, any published exact solution. This solution is generalized to two- and three-dimensions.

The behavior at late times shows an **asymptotic solution** as well where the saturation profiles being dumped by a power function of time. An asymptotic solution for large t is sought using the Ansatz:

$$1 - S(x,t) = y(x)/t^{\beta}. \qquad \text{Eq. 3-44}$$

Inserting this solution into Eq. 3-20 shows that this may be possible if the following condition is satisfied:

$$\beta = \frac{1}{\alpha_1}. \qquad \text{Eq. 3-45}$$

Consequently, the asymptotic solution of Eq. 3-20 writes:

$$1 - S(x,t) = \frac{y(x)}{t^{1/\alpha_1}}, \qquad \text{Eq. 3-46}$$

where $y(x)$ is a solution of the ordinary differential equation $\frac{\mathrm{d}}{\mathrm{d}x}\left(y^{\alpha_1}\frac{\mathrm{d}y}{\mathrm{d}x}\right) = -\frac{1}{\alpha_1 D_1}\, y$, which we shall rewrite:

$$\frac{d^2}{dx^2}\left(y^{\alpha_1+1}\right) = -\frac{\alpha_1+1}{\alpha_1 D_1}\, y. \qquad \text{Eq. 3-47}$$

Further transformations $g = y^{\alpha_1+1}$ and $h = \lambda g$ with λ a constant yield:

$$\frac{d^2h}{dx^2} = -\lambda^{\frac{\alpha_1}{\alpha_1+1}}\,\frac{\alpha_1+1}{\alpha_1 D_1}\, h^{\frac{1}{\alpha_1+1}}, \qquad \text{Eq. 3-48}$$

where, choosing $\lambda = \left(\frac{\alpha_1 D_1}{\alpha_1+1}\right)^{\frac{\alpha_1+1}{\alpha_1}}$, Eq. 3-48 may be written under the following form:

$$\frac{d^2h}{dx^2} = -h^{\frac{1}{\alpha_1+1}}, \qquad \text{Eq. 3-49}$$

$$h = \lambda g = \lambda y^{\alpha_1+1} = \left(\frac{\alpha_1 D_1}{\alpha_1+1}\right)^{\frac{\alpha_1+1}{\alpha_1}} y^{\alpha_1+1}, \qquad \text{Eq. 3-50}$$

for $x \in [0, L]$, and with the following boundary condition:

$$\begin{cases} 1 - S(x,t) = 0 \ \rightarrow y(0) = 0 & (x = 0,\ t > 0) \\ 1 - S(x,t) = 0 \ \rightarrow y(L) = 0 & \left(x = L,\ t > 0\right). \end{cases} \qquad \text{Eq. 3-51}$$

The solution sought is symmetric (even) around $x = \frac{L}{2}$, one must have $\frac{\mathrm{d}y}{\mathrm{d}x} > 0$ for $x \in [0, \frac{L}{2}]$ and $\frac{\mathrm{d}y}{\mathrm{d}x} < 0$ for $x \in [\frac{L}{2}, L]$. Therefore the condition $\frac{\mathrm{d}y}{\mathrm{d}x}\left(\frac{L}{2}\right) = 0$ must hold.

Before going further it is worth noting that when exponent α_1 is very large, Eq. 3-49 can be simplified to:

$$\frac{d^2h}{dx^2} = -1, \qquad \text{Eq. 3-52}$$

whose solution is the parabola $h(x) = \frac{1}{2}x(L - x)$ such that $h(L/2) = L^2/8$.

Coming back to the general case, it can be remarked that multiplying each member of Eq. 3-49 by $\frac{\mathrm{d}h}{\mathrm{d}x}$, the equation can be integrated once to yield

$$\frac{1}{2}\left(\frac{dh}{dx}\right)^2 = \frac{\alpha_1+1}{\alpha_1+2}\left(h^{\frac{\alpha_1+2}{\alpha_1+1}}\left(\frac{L}{2}\right) - h^{\frac{\alpha_1+2}{\alpha_1+1}}\right), \qquad \text{Eq. 3-53}$$

where the right hand side $\frac{\alpha_1+1}{\alpha_1+2}\ h^{\frac{\alpha_1+2}{\alpha_1+1}}\left(\frac{L}{2}\right)$ is an integration constant that is determined by the condition $\frac{\mathrm{d}h}{\mathrm{d}x}\left(\frac{L}{2}\right) = 0$. For $x \in [0, L/2]$, this last form integrates into

$$\begin{aligned} x \quad &= \sqrt{\frac{\alpha_1+2}{2(\alpha_1+1)}} \int_0^h \frac{dh}{\sqrt{h^{\frac{\alpha_1+2}{\alpha_1+1}}\left(\frac{L}{2}\right) - h^{\frac{\alpha_1+2}{\alpha_1+1}}}} \\ &= \sqrt{\frac{(\alpha_1+1)h^{\frac{\alpha_1}{\alpha_1+1}}\left(\frac{L}{2}\right)}{2(\alpha_1+2)}} \int_0^{[h/h\left(\frac{L}{2}\right)]^{\frac{\alpha_1+2}{\alpha_1+1}}} \frac{t^{\frac{\alpha_1+1}{\alpha_1+2}-1}}{\sqrt{1-t}}\ dt, \end{aligned} \qquad \text{Eq. 3-54}$$

setting $t = [h/h\left(\frac{L}{2}\right)]^{\frac{\alpha_1+2}{\alpha_1+1}}$. This relationship set with $x = \frac{L}{2}$ yields $h\left(\frac{L}{2}\right)$ in implicit form:

$$\frac{L}{2} = \sqrt{\frac{(\alpha_1+1)h^{\frac{\alpha_1}{\alpha_1+2}}\left(\frac{L}{2}\right)}{2(\alpha_1+2)}} \int_0^1 \frac{t^{\frac{\alpha_1+1}{\alpha_1+2}-1}}{\sqrt{1-t}}\, dt. \qquad \text{Eq. 3-55}$$

Using Euler incomplete beta and gamma[1] functions, the solution rewrites as

$$x = \sqrt{\frac{(\alpha_1+1)h^{\frac{\alpha_1}{\alpha_1+1}}\left(\frac{L}{2}\right)}{2(\alpha_1+2)}}\, B\left(\left[\frac{h}{h\left(\frac{L}{2}\right)}\right]^{\frac{\alpha_1+2}{\alpha_1+1}}; \frac{\alpha_1+1}{\alpha_1+2}, \frac{1}{2}\right), \qquad \text{Eq. 3-56}$$

with $h(\frac{L}{2})$given by:

$$h\left(\frac{L}{2}\right) = \left(\frac{L}{2\sqrt{2\pi}} \frac{\alpha_1}{\sqrt{(\alpha_1+1)(\alpha_1+2)}} \frac{\Gamma\left(\frac{\alpha_1}{2(\alpha_1+2)}\right)}{\Gamma\left(\frac{\alpha_1+1}{\alpha_1+2}\right)}\right)^{\frac{2(\alpha_1+1)}{\alpha_1}}. \qquad \text{Eq. 3-57}$$

Noteworthy, this solution converges for $\alpha_1 \to \infty$ to the parabola that was previously obtained by direct calculation in the specific case of a very large α_1 exponent, which writes implicitly $x = L/2 - \sqrt{(L/2)^2 - 2h}$ with $h(L/2) = L^2/8$.

Going back to the main unknown y, related to h by Eq. 3-50, the following implicit expression that fulfills all the boundary conditions may be obtained:

$$x = \sqrt{\frac{\alpha_1 D_1\, y^{\alpha_1}\left(\frac{L}{2}\right)}{2(\alpha_1+2)}}\, B\left(\left[\frac{y}{y\left(\frac{L}{2}\right)}\right]^{\alpha_1+2}; \frac{\alpha_1+1}{\alpha_1+2}, \frac{1}{2}\right), \qquad \text{Eq. 3-58}$$

with $y\left(\frac{L}{2}\right)$ given by:

$$y\left(\frac{L}{2}\right) = \left(\frac{L}{2}\sqrt{\frac{\alpha_1}{2\pi(\alpha_1+2)D_1}} \frac{\Gamma\left(\frac{\alpha_1}{2(\alpha_1+2)}\right)}{\Gamma\left(\frac{\alpha_1+1}{\alpha_1+2}\right)}\right)^{\frac{2}{\alpha_1}}. \qquad \text{Eq. 3-59}$$

[1] Incomplete beta, beta and gamma function are respectively defined as $B(x;a,b) = \int_0^x t^{a-1}(1-t)^{b-1}\,\mathrm{d}t$, $B(x,y) = \int_0^1 t^{x-1}(1-t)^{y-1}\,\mathrm{d}t = \frac{\Gamma(x)\Gamma(y)}{\Gamma(x+y)}$ and $\Gamma(z) = \int_0^\infty t^{z-1}e^{-t}\,\mathrm{d}t$ [Abramowitz and Stegun (1964)].

The solution for $y\left(\frac{L}{2}\right)$ and $y(x)/y\left(\frac{L}{2}\right)$ are reported in Figure 3-13(a) and (b). Unlike solution Eq. 3-43 obtained for the early-time regime by assuming the porous block to be semi-infinite, the late-time asymptotic solution Eq. 3-58 derived on a finite-size domain involves a characteristic length which is the block length L. Contrary to the early-time solution, in the late-time regime the water saturation is close to unity at every location in the matrix, therefore the power-law assumption given in Eq. 3-20 is automatically satisfied. A good agreement can be expected for the long time asymptotic behaviour independently of the details of $D(S)$ over the whole range of saturations, as reported in Figure 3-13(c)-(d) where the timescale is normalized by the diffusion time $\tau_0 = L^2/(4D_0)$. With a value of $D_0 = 1.45 \times 10^{-5}\ \frac{m^2}{s}$ in base case ($\alpha_0 = 1.5, \alpha_1 = 2$), we get a characteristic time of $\tau_0 = 16900$ s that can be compared to molecular diffusion (10^3 s) and pressure diffusion (10^{10} s) cases.

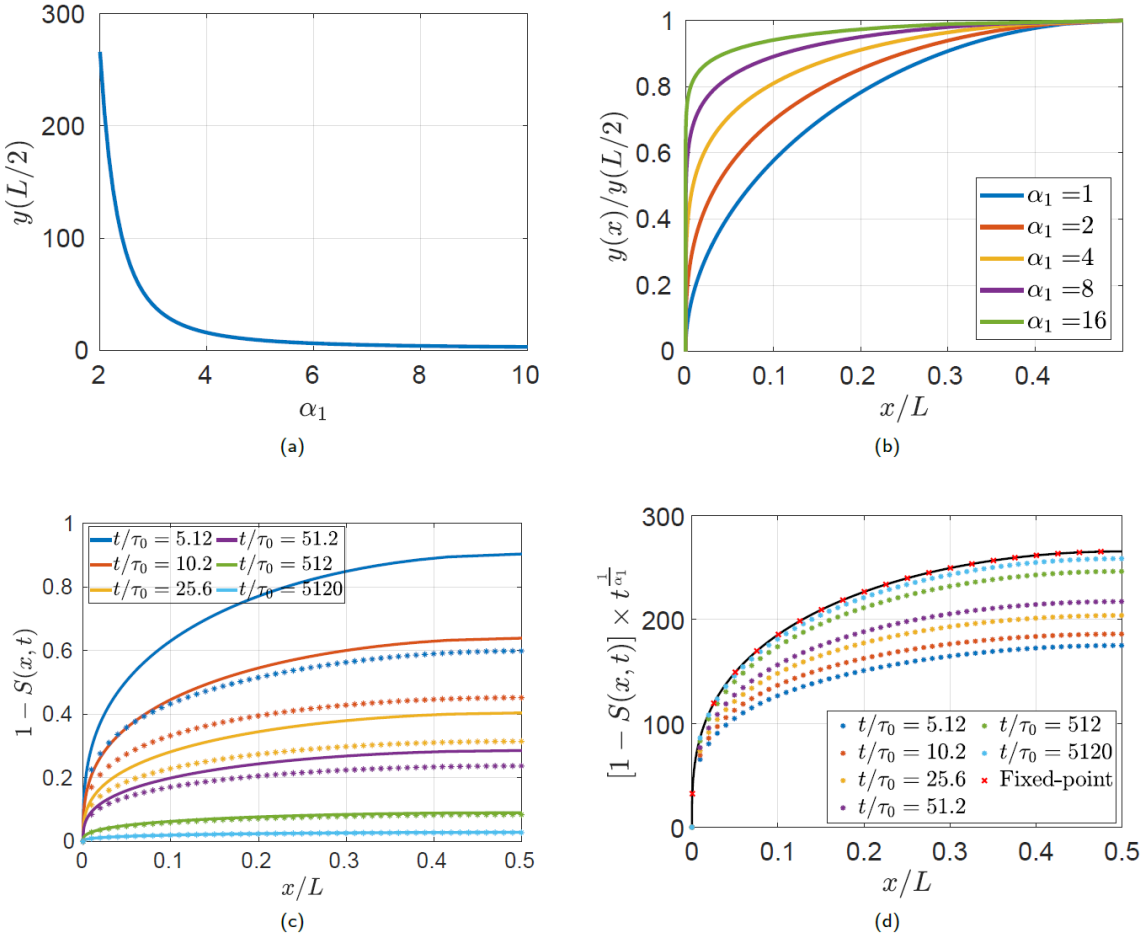


Figure 3-13 (a)-(b) Late-time analytical solution $y(x)$ given in Eq. 3-58 for several α_1 values. (c)-(d) Comparison of the late-time analytical solution $1 - S(x,t) = y(x)/t^{1/\alpha_1}$ and rescaled $y(x) = [1 - S(x,t)]t^{1/\alpha_1}$ (solid lines) given in Eq. 3-46 and Eq. 3-58 with the simulated one (symbols) for $\alpha_1 = 2$, $p = 3$, $M = 6$, $m = 2$, $k = 10$ mD, $P_e = 5$ bar, $\phi = 0.25$, $S_{wi} = S_{orw} = 0$. Timescale is normalized by the diffusion time $\tau_0 = L^2/(4D_0)$. Red crosses for the fixed-point solution (detailed in section 3.7.3) indicated in (d) correspond to a direct numerical solution of the asymptotic ansatz.

In the displayed example, the time convergence of the numerical solution to the asymptotic one given in Eq. 3-46 and Eq. 3-58 is pretty slow. That can be accurately quantified by comparing the time evolution of the numerical solution $1-S$ or $(1-S)t^{1/\alpha_1}$ with the asymptotic one for fixed x/L values. Specifically, the numerical solution time convergence to the asymptotic one is slower than the asymptotic solution $1/\sqrt{t}$ trend for $\alpha_1 = 2$ and intermediate t/τ_0 values. The reader may wish to consult Figure 3-14 given later in Section 3.6, which reports the time evolution of the matrix-to-fracture flux, to spot the transition between the early- and the late-time regimes that occurs around $t^*/\tau_0 = 40\text{-}50$ in the example displayed in Figure 3-13(c)-(d).

Ultimately, the numerical solution time evolution matches the asymptotic solution one as Fig. 3-13(c)-(d) indicate about 6 and 2% relative difference between numerical and asymptotic solutions, $|S_\infty - S_{\text{num}}|/(1-S_\infty)$, for $t/\tau_0 = 512$ and 5120, respectively. The larger the exponent α_1, the slower this convergence. This is consistent with the typical behaviour of a porous medium that is preferentially wettable to the non-aqueous phase, for which the exponent $q = \alpha_1$ of the relative permeability to the non-aqueous phase, assuming a power-law saturation dependency Eq. 3-3 to Eq. 3-5, is generally large, for it imbibes more slowly than a water-wet porous medium.

To conclude this section, unlike the early-time regime, in the late-time regime, the low NAPL assumption $S(t) \approx 1$ becomes more and more valid as time increases. The asymptotic solution is likely to be independent on the details of $D(S)$ once $D(S) \approx D_1(1-S)^{\alpha_1}$ as $S \to 1$.

These early and late time solution from this section can help to establish a model for matrix-fracture interporosity flux that can be used in a up-scaled dual-medium approach.

3.6 Non-linear closure for matrix-fracture flux

(Wolff, 1987) studied counter-current imbibition in a two-dimensional matrix block and concluded that the imbibition flux can be approximated by two power-function curves based on his numerical solutions. Wolff also presented the results of some sensitivity runs but no explicit relationships between parameters defining power-functions and petro-physical properties. In this section, we model the matrix-fracture flux based on our analytical solutions for counter-current capillary imbibition by separating the transfer process at early- and late-times.

When large discrete fracture networks embedded in a permeable porous matrix are considered, it is customary to adopt a dual-porosity framework in which the coupling with the matrix may be accounted for via a source term $\Phi_{\mathrm{mf}}(t)$ (Cherblanc et al., 2003; Landereau et al., 2001; Noetinger et al., 2001; Noetinger, 2015; Noetinger et al., 2016; Noetinger & Jarrige, 2012).

(K. Li & Zhao, 2012) investigated the spontaneous imbibition rate which is a power-law function of time and is widely reported as $\Phi_{\mathrm{mf}}(t) = At^{m_s}$. Also, A is a constant associated with rock/fluid properties such as porosity, permeability, viscosity, capillary pressure, and relative permeability, m_s is the exponent (its quantification will be discussed later), and *t* is the production time. Many studies showed the value of m_s is equal to 0.5 (Handy, 1960; Washburn, 1921; Zimmerman & Bodvarsson, 1991) among all. All the above models have theoretical bases, which are the mass balance and continuum equations. We use the semi-analytical solutions of two limiting cases to propose the flux formulation.

This source term $\Phi_{\mathrm{mf}}(t)$ corresponds to a volume average of the normal flux between matrix and fractures. In the case of linear local flow equations, the generic closure of $\Phi_{\mathrm{mf}}(t)$ appears as being a time convolution of the local variable $S(x,t)$ with a time-dependant kernel that may be evaluated solving a relaxation problem on a representative matrix block. In particular, focusing on the long time limit, when the relaxation of the block reaches its exponential decay, it can be shown that $\Phi_{\mathrm{mf}}(t) \approx -\frac{S(x,t)-S_{\mathrm{f}}(x,t)}{\tau_{\mathrm{m}}}$ with x the block centroid and S_{f} the surrounding fracture saturation. The relaxation time τ_{m} may be related to the block typical dimensions via the relation $\tau_{\mathrm{m}} \approx \sigma L^2/D_0$ where σ is the shape-factor of the matrix block as was described in detail in the previous chapter. In the more general case, it is a geometric quantity that is known for several block shapes, and that is related to the smallest eigenvalue of the Laplacian operator with Dirichlet boundary conditions on the block (Landereau et al., 2001).

Coming back to the non-linear case, at first sight, the convolution approach is useless, so another closure must be proposed, if any. In both short- and long-time regimes, the time variation of the matrix to fracture flux $\Phi_{\mathrm{mf}}(t) = (D(S)\,\partial S/\partial x)_{x=0}$ can be estimated using the previously presented solutions. In the short time case, using the Boltzmann variable, $\Phi_{\mathrm{mf}}(t)$ may be estimated directly as $\Phi_{\mathrm{mf}}(t) = (D(S)/\sqrt{4D_0 t})(\mathrm{d}S/\mathrm{d}\xi)_{\xi=0} \sim 1/\sqrt{t}$ up to a prefactor A_0. In the long time case, it is useful to introduce the spatial average of the matrix saturation

defined by $\langle S\rangle(t) = \frac{1}{L/2}\int_0^{L/2} S(x,t)\,\mathrm{d}x$. Averaging the diffusion equation Eq. 3-13 and swapping the time partial derivative and the spatial average, one gets $\frac{L}{2}\frac{\mathrm{d}\langle S\rangle}{\mathrm{d}t} = \int_0^{L/2} \frac{\partial}{\partial x}\left(D(S)\frac{\partial S}{\partial x}\right)\mathrm{d}x = -\left(D(S)\frac{\partial S}{\partial x}\right)_{x=0}$ hence $\Phi_{\mathrm{mf}}(t) = \frac{L}{2}\frac{\mathrm{d}\langle S\rangle}{\mathrm{d}t}$. In all the considered cases, similar results were obtained using the time derivative of the average saturation or the global flux at the boundary, so the former definition was retained. Inserting the late-time Ansatz in this expression, it may be shown that the matrix to fracture flux varies asymptotically as $\Phi_{\mathrm{mf}}(t) \sim 1/t^{(\alpha_1+1)/\alpha_1}$. The proportionality factor A_∞ can be evaluated using the analytical solution $y(x)$ starting from Eq. 3-53 and Eq. 3-57. The same algebraic decay was already discovered by (Tavassoli et al., 2005b) and (L. Li et al., 2020). In both papers, the authors selected the Ansatz dealing with the spatial variable valid close to the matrix/fracture boundary. Although that approach leads to analogous long time variations of the NAPL saturation, it does not provide a complete solution in the space domain, and it appears less general, especially in the multi-dimensional case.

Summarizing the results, we get:

$$\Phi_{mf}(t) \approx \begin{cases} A_0/\sqrt{t} & for\ t \to 0, \\ A_\infty/t^{\frac{\alpha_1+1}{\alpha_1}} & for\ t \to \infty. \end{cases} \qquad \text{Eq. 3-60}$$

Both constants A_0 and A_∞ encapsulate the spatial details of the corresponding asymptotic solutions and may be obtained manipulating the expressions Eq. 3-27 for A_0 and Eq. 3-50, Eq. 3-53, Eq. 3-56 and Eq. 3-57 to obtain A_∞, which gives the following expressions:

$$A_0 = \sqrt{D_0}\int_0^1 \xi(S)\,dS, \qquad \text{Eq. 3-61}$$

$$A_\infty = \frac{1}{\alpha_1}\left(\frac{\alpha_1+1}{\alpha_1 D_1}\right)^{\frac{1}{\alpha_1}}\sqrt{\frac{2(\alpha_1+1)}{\alpha_1+2}}\left(\frac{L}{2\sqrt{2\pi}}\frac{\alpha_1}{\sqrt{(\alpha_1+1)(\alpha_1+2)}}\frac{\Gamma\left(\frac{\alpha_1}{2(\alpha_1+2)}\right)}{\Gamma\left(\frac{\alpha_1+1}{\alpha_1+2}\right)}\right)^{\frac{\alpha_1+2}{\alpha_1}}. \qquad \text{Eq. 3-62}$$

If one plots $\Phi_{\mathrm{mf}}(t)$ using a log-log scale, two straight lines can be observed. The transition time from one regime to the other corresponds to a time t of $\xi_0\left(\frac{L}{2}\right)$. This is illustrated in Figure 3-14(a) which reports the time evolution of the matrix-to-fracture flux for a few $\alpha_{0,1}$ values. Simulated early- and late-time slopes are in excellent agreement with the early- and late-time predictions $\frac{1}{2}$ and $\frac{\alpha_1+1}{\alpha_1}$, respectively. The transition between the early- and late-time

regimes, which is observed for $t/\tau_0 = 5$-10 in Figure 3-14(a) and is very clear with a very tight and sharp cross-over, could be rescaled to $t/\tau = 1$ by considering not the characteristic time $\tau_0 = L^2/(4D_0)$ suggested by dimensional analysis but $\tau = L^2/(16\xi_0^2 D_0)$ derived from $\xi = x/\sqrt{4D_0 t}$ setting $\xi = \xi_0$ and $x = L/2$. It is worth noting the low influence of the early-time exponent α_0.

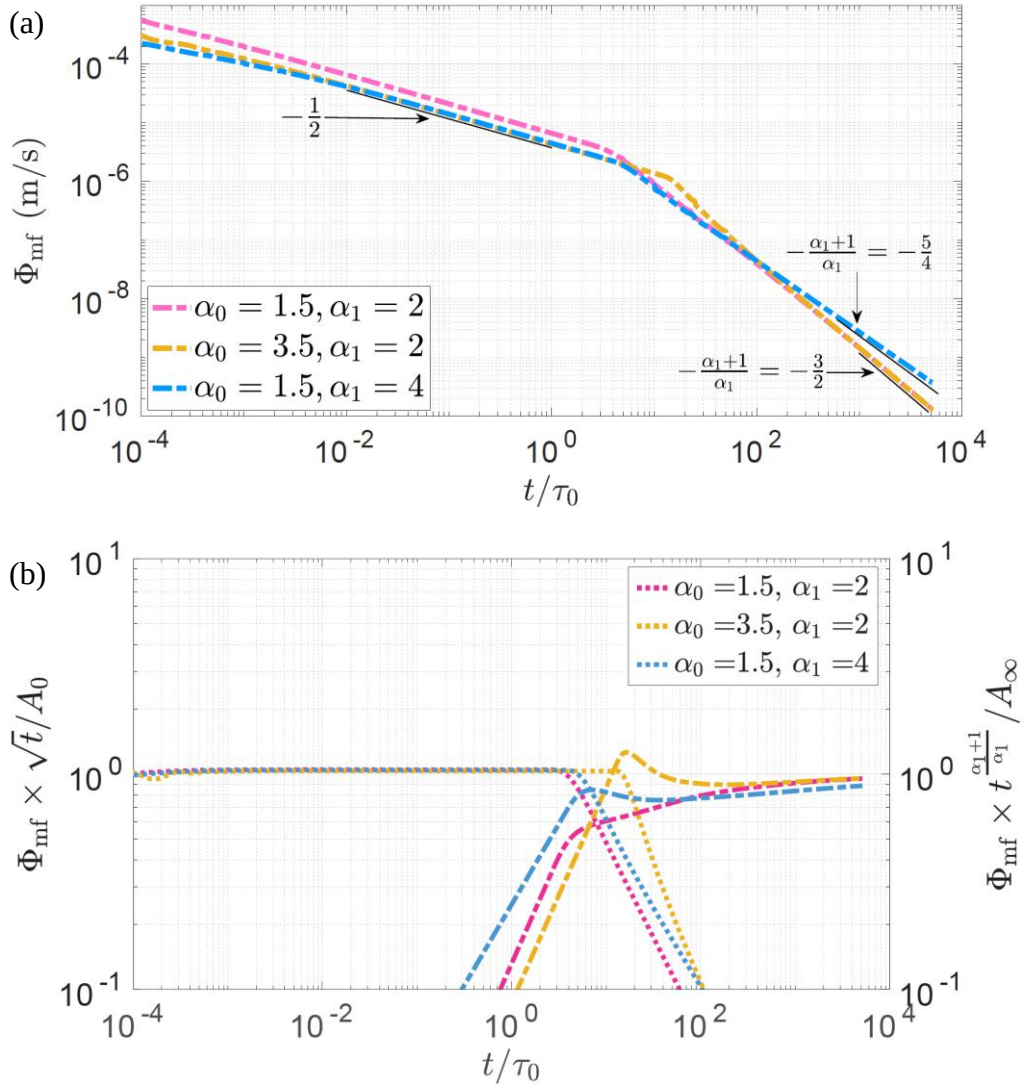


Figure 3-14 (a) Time evolution of the matrix-to-fracture flux for a few α_0 and α_1 exponents $\alpha_0 = 1.5$, 3.5 ($p = 3, 5$, $m = 2$) and $\alpha_1 = 2$, 4 with $M = 6$, $k = 10$ mD, $P_e = 5$ bar, $\phi = 0.25$ and $S_{wi} = S_{orw} = 0$. Simulated early- and late-time slopes $-\{0.48,0.46,0.44\}$ and $-\{1.45,1.48,1.21\}$, respectively, are in excellent agreement with the early- and late-time predictions (thin solid lines) $-\frac{1}{2}$ and $-\frac{\alpha_1+1}{\alpha_1} = -\frac{3}{2}$ and $-\frac{5}{4}$ for $\alpha_1 = 2$ and 4, respectively. The time scale is normalized by the diffusion time $\tau_0 = L^2/(4D_0)$. (b) Time evolution of the matrix-to-fracture flux multiplied by its asymptotic time dependencies (Eq. 3-60) and divided by its asymptotic prefactors A_0 and A_∞ (Eq. 3-61) and (Eq. 3-62) for the same α_0 and α_1 exponents.

Figure 3-14(b) reports the time evolution of the simulated fracture-to-matrix flux Φ_{mf} normalized by its asymptotic time dependencies and divided by its asymptotic prefactors A_0 and A_∞ Eq. 3-61 and Eq. 3-62 for the same α_0 and α_1 exponents as in Figure 3-14(a). Except for the cross-over between the short and long time regimes, the asymptotic Eq. 3-60 are found with excellent accuracy and dominate most of the exchange dynamics over several orders of magnitude.

It can be observed that using the long-time asymptotics $\langle 1-S\rangle \sim t^{-1/\alpha_1}$, one can write the matrix to fracture flux under the following form: $\Phi_{\mathrm{mf}}(t) \sim \langle 1-S\rangle^{\alpha_1+1}$. That non-linear closure between the local matrix to fracture flux and the average matrix saturation generalizes the usual linear closure relation that gives rise to most dual porosity models. The underlying proportionality factor may be obtained directly from the fixed point solution, and could be related to usual shape factors of the literature (Landereau et al., 2001).

To finish with, it can be remarked that using the relation $\Phi_{\mathrm{mf}}(t) = \frac{L}{2}\frac{\mathrm{d}\langle S\rangle}{\mathrm{d}t}$, if $\alpha_1 = 0$ is inserted in that formula, it provides a linear exponential relaxation of the matrix saturation. That is consistent with the corresponding findings of the constant diffusion case. In the non-linear case, a non-linear closure is obtained. Estimations of that closure for a whole range of time-scales accounting for both the short time and long time scales were proposed by (L. Li et al., 2020, Li et al.). However, a generalization to general three-dimensional condition is demanding.

3.7 Generalization to 2D and 3D blocks

We now generalize the results obtained in one dimension of space to any dimension of space for any matrix block geometry. Under the given boundary conditions, the porous medium still undergoes counter-current imbibition as demonstrated in Section 3.2.2 without the need for the matrix block to exhibit symmetries.

We first indicate in Sections 3.7.1 and 3.7.2 which quantitative features are preserved with respect to the one-dimensional early- and late-time asymptotic solutions and corresponding fluxes, and which are not and require additional investigation. Then, we show in Section 3.7.3 how the late-time asymptotic solution separate form Eq. 3-46 can be exploited to develop a simple and efficient fixed-point numerical solution method, which advantageously replaces the delicate solving of the initial nonlinear singular diffusion equation. Finally, we

demonstrate in Section 3.7.4, by considering some simple two-dimensional block geometries, that the full dynamics of capillary imbibition can be accurately and efficiently predicted. The matrix block imbibition still presents two regimes whose saturation and fracture-to-matrix flux can be computed: a diffusive early-time regime and an anomalous late-time regime that cross-over tightly. Eventually, residual points to investigate are discussed.

3.7.1 Early-time regime

In the general case of matrix blocks having arbitrary shapes, there is no simple approximation working yielding a detailed description of the short time regime. A generalization of Parlange's results might be worth investigating, although nothing simple is apparent at first sight. At very short time, keeping the Boltzmann assumption of a dependency on $\mathbf{x}/\sqrt{t}$ is equivalent to setting up a boundary layer approximation (Lamb, 1932; Landau & Lifshitz, 1987; Tritton, 1988). Physically it corresponds to considering that locally the block boundary can be assumed to be planar, and then to use the one-dimensional solution. Such an approximation can be assumed to be valid if the diffusion length $\sqrt{D_0 t}$ is much smaller than any characteristic lengthscale of the block. The occurrence of such a regime is confirmed once considering the matrix-to-fracture flux that is observed hereafter in Figure 3-21 of Section 3.7.4 to vary as $1/\sqrt{t}$ at short times for simple matrix block geometries. Then a transient regime leading to the long time asymptotic solution can be observed.

3.7.2 Late-time regime

As detailed in the next section, the late-time asymptotic solution in the separate form Eq. 3-46 remains valid for any dimension of space and any block shape, except that the function $y(x)$, whose analytical expression Eq. 3-58 has been derived in one dimension of space, and which we will henceforth denote $f(\mathbf{x})$, remains to be determined. Thus, except for this detail which we will show hereafter how to manage quickly and accurately numerically, the late-time asymptotic solution $1 - S(\mathbf{x}, t)$ preserves a time dependence in $1/t^{1/\alpha_1}$ and the corresponding asymptotic flux Eq. 3-60 still presents an algebraic anomalous decay that is proportional to $1/t^{(\alpha_1+1)/\alpha_1}$, whose prefactor A_∞ remains to be computed and no longer writes as in Eq. 3-62 as it obviously depends on the space solution $f(\mathbf{x})$.

3.7.3 Fixed-point algorithm

The late-time asymptotic approach Eq. 3-46 remains valid for any dimension of space and any block shape. The solution of Eq. 3-20 writes:

$$1 - S(x,t) = \frac{f(\mathbf{x})}{t^{\frac{1}{\alpha_1}}}, \qquad \text{Eq. 3-63}$$

where $f(\mathbf{x})$ satisfies $\nabla \cdot (f^{\alpha_1} \nabla f) = -f/(\alpha_1 D_1)$, which is rewritten as already done in Eq. 3-47 to Eq. 3-50:

$$\nabla^2 h = -h^{\frac{1}{\alpha_1+1}}, \qquad \text{Eq. 3-64}$$

$$h = \left(\frac{\alpha_1 D_1}{\alpha_1 + 1}\right)^{\frac{\alpha_1+1}{\alpha_1}} f^{\alpha_1+1}. \qquad \text{Eq. 3-65}$$

As already noted in Section 3.5, h satisfies $\nabla^2 h = -1$ when the exponent α_1 is very large, whose solution is a parabola in one dimension. This will serve as an initial guess to implement a fixed-point method to solve Eq. 3-64.

Thus we need to solve a Laplace equation in a domain Ω of boundary $\partial\Omega$ on which $h = 0$. Specifically, a sequence of functions $(h_k)_{k\geq 0}$ such that

$$\begin{aligned} \nabla^2 h_k &= -h_{k-1}^{\frac{1}{\alpha_1+1}} && in\ \Omega, \\ h_k &= 0 && on\ \partial\Omega, \end{aligned} \qquad \text{Eq. 3-66}$$

for all $k \geq 1$ is looked for with the following initial guess

$$\begin{aligned} \nabla^2 h_0 &= -1 && \text{in } \Omega, \\ h_0 &= 0 && \text{on } \partial\Omega. \end{aligned} \qquad \text{Eq. 3-67}$$

At each iteration of the algorithm, we solve the non-singular elliptic problems Eq. 3-66 and Eq. 3-67 using a finite element method provided by the FreeFEM++ open-source PDE solver (Hecht, 2012). In 2D, that code generated meshes with triangular elements and Lagrangian P1 basis functions. The iterative algorithm is performed until $\| h_k - h_{k-1} \|_\infty$ and $\| h_k - h_{k-1} \|_2$ are small enough. Residuals less than 10^{-12} have been imposed so that a few iterations (about 20) are enough to converge which makes the algorithm fast and allows the use of fine meshes to obtain very accurate solutions. Also, as the initial guess corresponds to the

solution of Eq. 3-67 with $\alpha_1 \to \infty$, a faster convergence is expected for higher values of α_1 for a given geometry.

3.7.4 Results

Running the algorithm in the one-dimensional case, gives an excellent agreement with the analytical solution as reported in Figure 3-13(d). A similar result has been obtained (but is not shown here as it does not bring much) by considering not the one-dimensional segment $[0, L]$ but a two-dimensional rectangle shown in Figure 3-3 with the same initial and boundary conditions, i.e. one pair of faces facing each other with imposed saturation and the other with zero flux.

Four two-dimensional geometries were considered in order to validate the fixed-point algorithm, considering the saturation imposed on the whole boundary of the matrix block, from the most to the least symmetrical, as shown in Figure 3-15:

- Disk of radius R,
- Square of side L,
- Rectangle of sides L_x and L_y,
- Quadrangle of medians L_x and L_y.

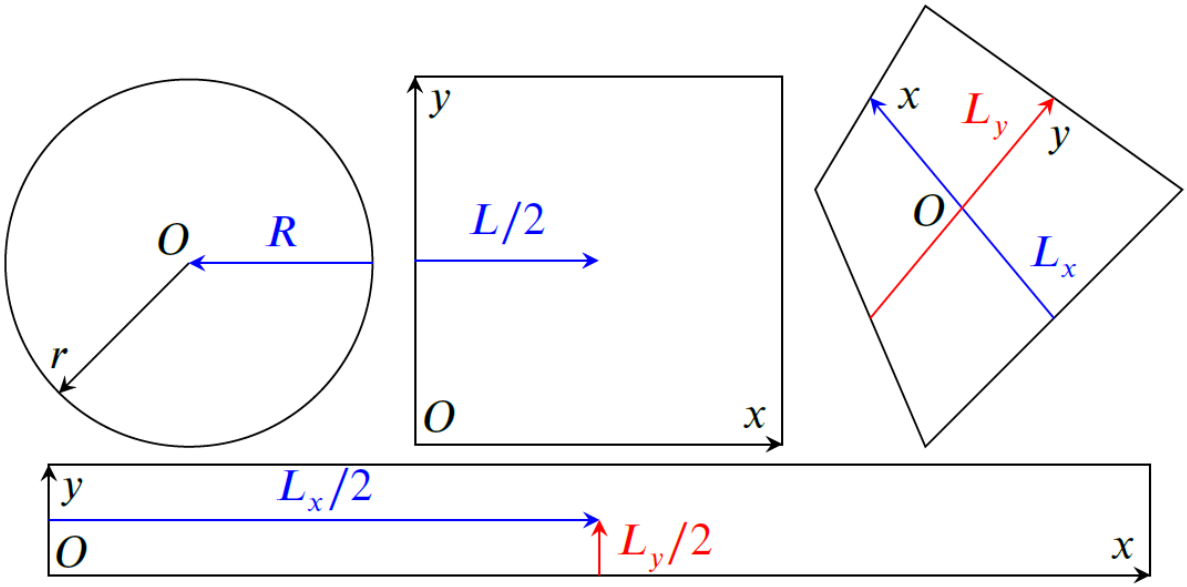


Figure 3-15 Two-dimensional geometries studied: disk, square, rectangle and quadrangle (all surfaces are to scale except the rectangle, magnified three times). The characteristic lengths as well as the paths on which the saturation field $1 - S(\mathbf{x}, t)$ is projected in plots below are indicated in blue and red (direction of the path is given by an arrow, coordinate system is shown in black).

For the record, the spherical geometry has also been treated but is not reported because except for some elementary algebra details it does not differ significantly from the cylindrical geometry shown hereafter (both are systems with one degree of freedom).

FreeFEM++ solves the partial differential Eq. 3-66 on domains of Figure 3-15 and a converged calculation for the distribution of $h(\mathbf{x})$ is shown in Figure 3-16. This result can be transformed to the saturation function at any time using the transformation Eq. 3-63 and Eq. 3-65.

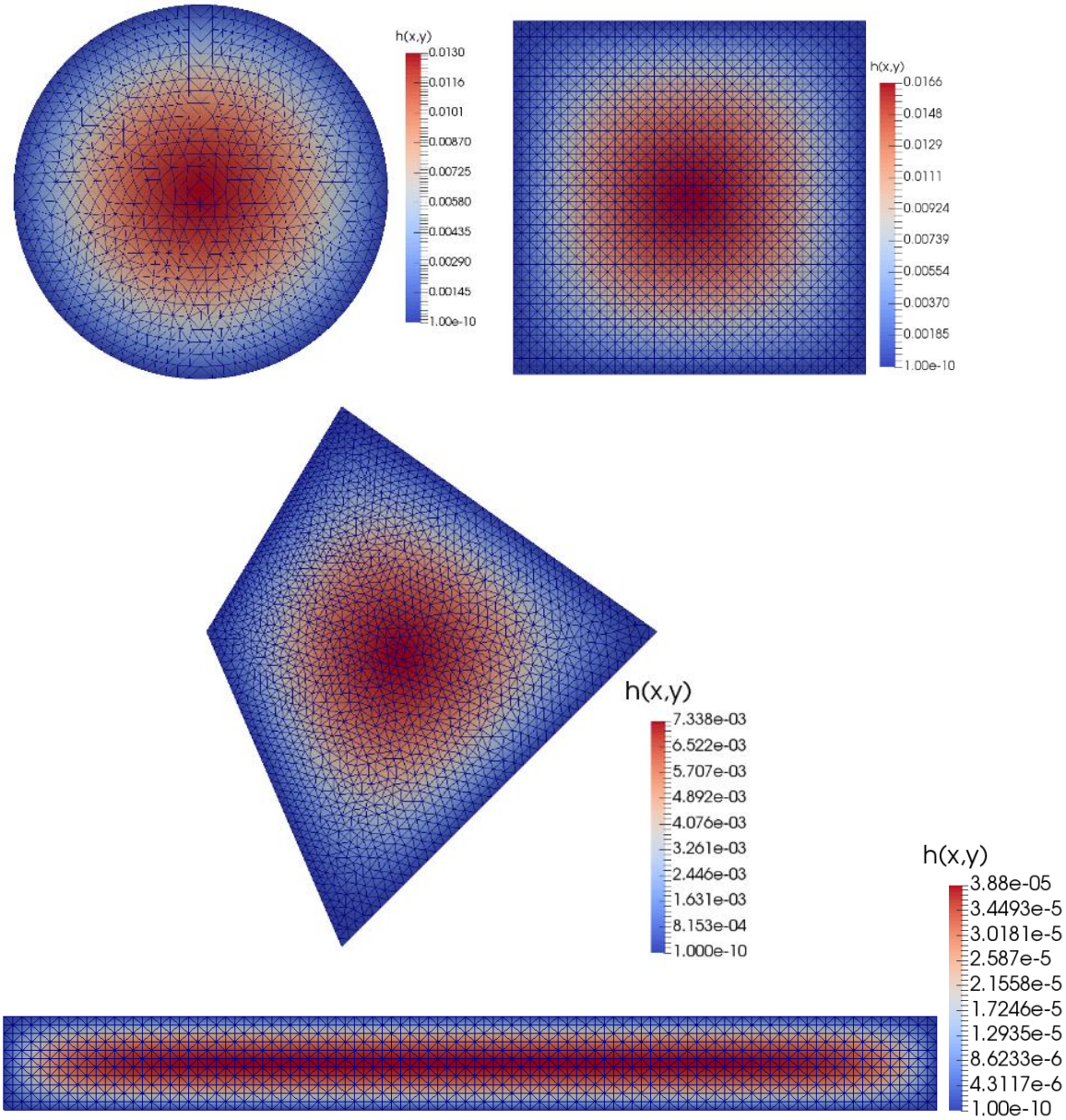


Figure 3-16 The solution map of Eq. 3-66 for the two-dimensional domains presented in Figure 3-15. The calculation is based on fixed-point algorithm conducted by FreeFEM software. The triangular mesh of the domains are coarser than the real meshes used for the results.

In each case, the diffusion time is characterized by $\tau_0 = L_c^2/(4D_0)$ where L_c is a characteristic length of the considered geometry. Here, we can assume $L_c = 2R$, L or L_x or L_y depending on whether the medium is a disk, square, rectangle or quadrangle. We will come back to this point later, which at this stage is more of a dimensional analysis but requires further analysis as we shall see when analyzing the fluxes. The considered flow configuration is one of those previously studied in previous sections such that $\alpha_1 = 2$, $p = 3$, $M = 6$, $m = 2$, $k = 10$ mD, $P_e = 5$ bar, $\phi = 0.25$ and $S_{wi} = S_{orw} = 0$.

Figure 3-17(a), Figure 3-18(a), Figure 3-19(a)-(b) and Figure 3-20(a)-(b) report the saturation profiles $1 - S(x,t)$ projected on the domain paths indicated in Figure 3-15 while Figure 3-17(b), Figure 3-18 (b), Figure 3-19(c)-(d) and Figure 3-20 (c)-(d) give the space dependence of the solution by plotting $[1 - S(x,t)]t^{1/\alpha_1}$. In all cases, an excellent agreement between the numerical and the fixed-point solution is observed for late times, specifically from $t/\tau_0 = 511$ for the disk, $t/\tau_0 = 511$ for the square, $t/\tau_0 = 5$ for the rectangle, and $t/\tau_0 = 838$ for the quadrangle.

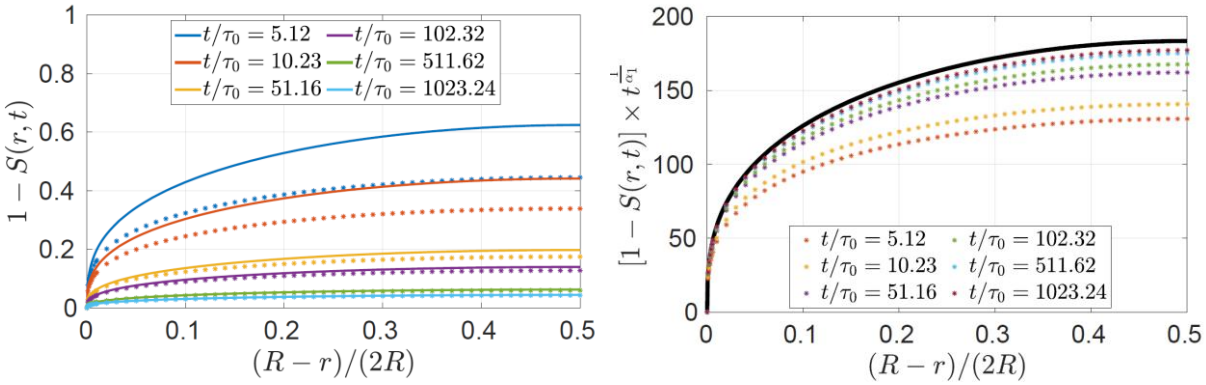


Figure 3-17 Disk — comparison of the fixed-point solution (solid lines, 1 654 elements) with the numerical solution (symbols, 500 nested rings). The time scale is normalized by the diffusion time $\tau_0 = L_c^2/(4D_0)$ with $L_c = 2R = 1$ m (see Figure 3-15).

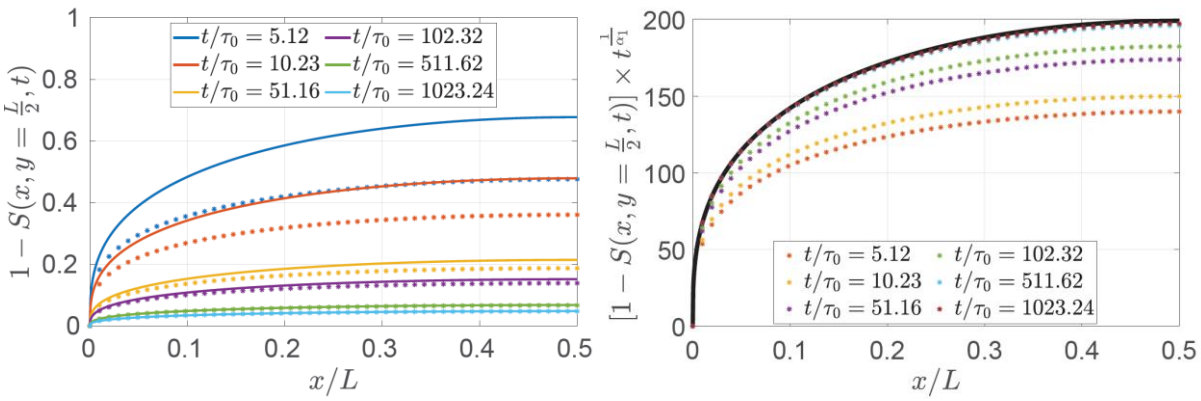


Figure 3-18 Square — comparison of the fixed-point solution (solid lines, 4 050 elements) with the numerical solution (symbols, $101 \times 101 = 10\,201$ cells). The time scale is normalized by the diffusion time $\tau_0 = L_c^2/(4D_0)$ with $L_c = L = 1$ m (see Figure 3-15).

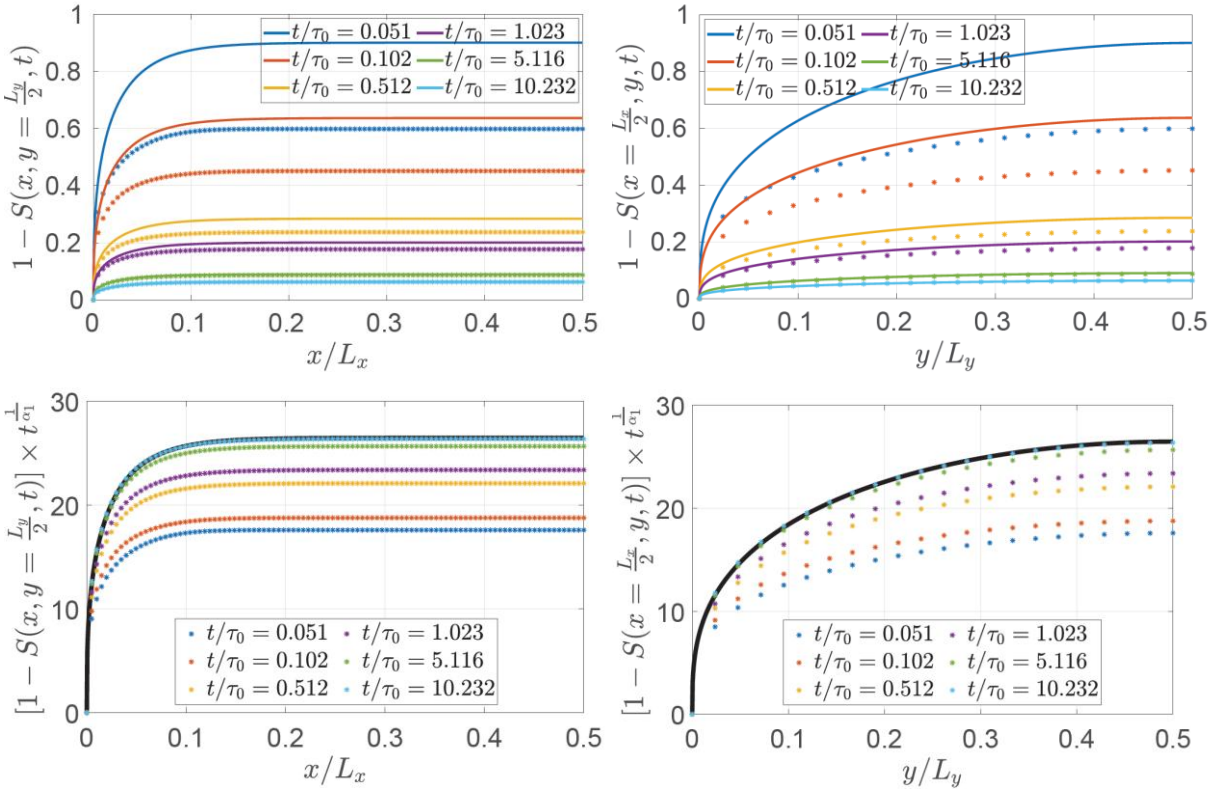


Figure 3-19 Rectangle — comparison of the fixed-point solution (solid lines, 2 222 elements) with the numerical solution (symbols, $201 \times 41 = 8\,241$ cells). The time scale is normalized by the diffusion time $\tau_0 = L_c^2/(4D_0)$ with $L_c = L_x = 10\ L_y = 1$ m (see Figure 3-15).

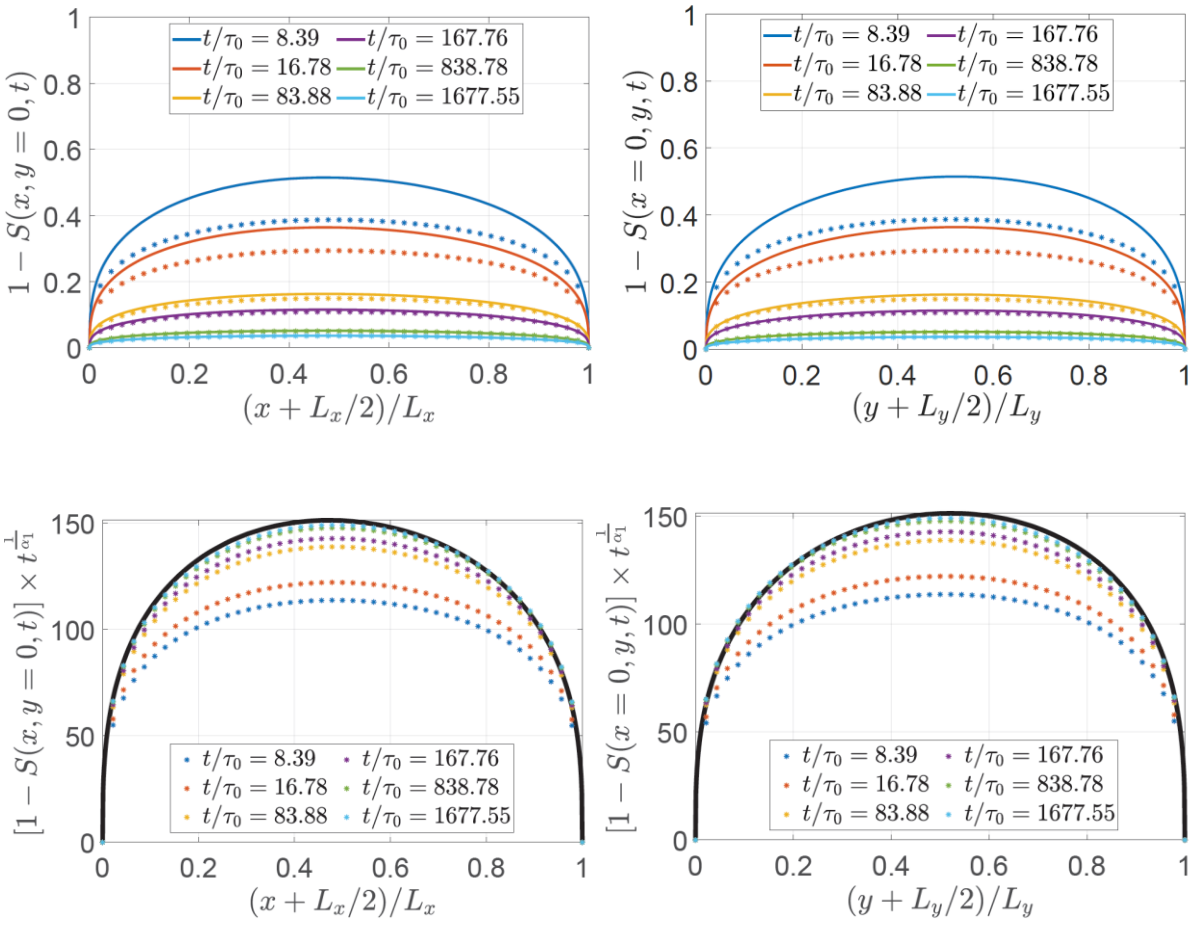


Figure 3-20 Quadrangle — comparison of the fixed-point solution (solid lines, 4 272 elements) with the numerical solution (symbols, $101 \times 101 = 10\,201$ cells). The time scale is normalized by the diffusion time $\tau_0 = L_c^2/(4D_0)$ with $L_c = L_x = L_y = 0.781$ m (see Figure 3-15).

Now let us look at the flux time evolution over the entire dynamic range. As already explained in Section 3.6, flux can be computed in two ways: either by the time derivative of the block's average saturation, or from the flux at the boundary. Indeed, integrating Eq. 3-13 on the considered domain Ω, defining the average saturation as $\langle S \rangle(t) = \frac{1}{|\Omega|}\int_\Omega S(x,t)\,\mathrm{d}x$ and using Stokes theorem, one gets a NAPL flux (of opposite sign to the water flux) of dimension $L^d T^{-1}$, where d is the space dimension, that reads

$$\Phi_{\mathrm{mf}}(\mathrm{t}) = -|\Omega|\frac{\mathrm{d}\langle \mathrm{S} \rangle(\mathrm{t})}{\mathrm{dt}} = -\int_{\partial\Omega} \mathrm{D}(\mathrm{S})\mathbf{n}\cdot\nabla \mathrm{S}\,\mathrm{d}\sigma \qquad \text{Eq. 3-68}$$

with **n** the ∂Ω outward normal unitary vector and |Ω| the measure of Ω. In two (three) space dimensions |Ω| is Ω area (volume), ∂Ω is its contour (surface) and dσ is an infinitesimal contour (surface) element of ∂Ω.

The flux time evolution that is more convenient to compute by the average saturation, but which we made sure does not depend on the mode of calculation (using the left or right hand side of Eq. 3-68, is reported in Figure 3-21 for all the tested geometries. Whatever the geometry considered, several points are worth noting:

- We observe once again, as in one dimension, an early-time diffusive regime that is characterized by a flux that varies proportionally to $1/\sqrt{t}$, and an anomalous late-time regime that is driven by a flux proportional to $1/t^{(\alpha_1+1)/\alpha_1}$.
- The flux's pre-factor A_∞ is no longer known analytically as in one dimension, following Eqs Eq. 3-61 and Eq. 3-62, but can be quickly obtained numerically from the fixed-point algorithm subject to having an accurate estimate of a finite value of $(t/\tau_0)_\infty$ for which the numerical solution has almost converged to the asymptotic solution for $t \to \infty$.

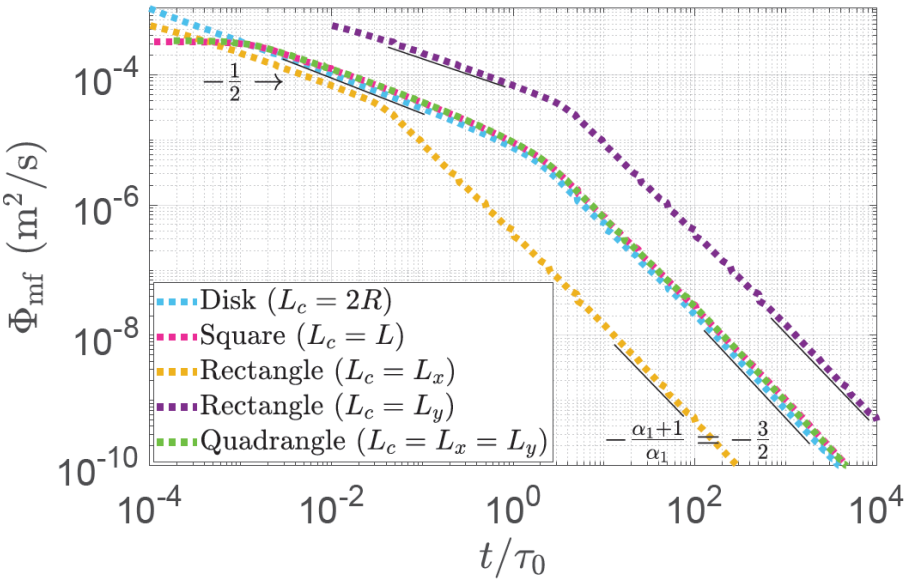


Figure 3-21 Time evolution of the simulated matrix-to-fracture flux for the considered two-dimensional geometries: disk, square, rectangle and quadrangle (see the text and Figs 2, 3, 4 and 5). Simulated early- and late-time slopes are in excellent agreement with the early- and late-time predictions (thin solid lines) $-\frac{1}{2}$ and $-\frac{\alpha_1+1}{\alpha_1} = -\frac{3}{2}$ for $\alpha_1 = 2$. The time scale is normalized by the diffusion time $\tau_0 = L_c^2/(4D_0)$ where the characteristic length L_c is set to 2R, L or L_x or L_y depending on whether the medium is a disk (of radius R), square (of side L), rectangle (of sides L_x and L_y) or quadrangle (of medians L_x and L_y). The tested flow configuration is such that $\alpha_1 = 2$, $p = 3$, $M = 6$, $m = 2$, $k = 10$ mD, $P_e = 5$ bar, $\phi = 0.25$ and $S_{wi} = S_{orw} = 0$.

- The cross-over between the early- and late-time regimes is very narrow. Therefore, the early- and late-time asymptotic solutions that dominate completely the fracture-to-

matrix dynamic exchange are sufficient to determine the flux over the whole exchange dynamics. In other words, if the asymptotic solutions are determined, then the whole dynamic response of the exchange is also determined to a very good approximation. This remains of course to be demonstrated in practice on more complex geometries than those tested.

– The flux's pre-factor A_∞ can be computed numerically by a spatial integration of the fixed-point solution. This being said, Figure 3-21 clearly shows that fluxes are all translated in time with respect to each other depending on the geometry considered. Rectangle flux in the current characteristic time is far from the other cases. This means that the relevant characteristic length L_c involved in the diffusion time $\tau_0 = L_c^2/(4D_0)$ remains to be found, instead of setting as we did $L_c = 2R$, L, L_x or L_y depending on whether the medium is a disk, square, rectangle or quadrangle. Once this one is found, if it exists, whatever the geometry considered, all the corresponding fluxes would be in phase and would superimpose if $\Phi_{\mathrm{mf}}(t)/A_\infty$ is considered for $t \to \infty$, following Eq. 3-60.

3.8 Ongoing work

If we consider the transition time as the time at which the flow front reaches the boundaries of flow then, we can consider $\tau = L_c^2/(16\xi_0^2 D_0)$ where, ξ_0 is estimated by Eq. 3-40 with $A_{1984,min} = 1/(\alpha_0 + 1)$ to characterize the transfers with different shapes and different non-linear capillary diffusion coefficients.

The characteristic length $L_c = f(L_x, L_y)$ in this scaling group can be defined using different proposals such as geometric average $L_c = \sqrt{L_x L_y}$ or the average flow length from each face to the center of the arbitrary shape $L_c = L_x L_y/\sqrt{L_x^2 + L_y^2}$ from Kazemi's formula (Eq. 2-17). This characteristic length in multi-dimensional cases demands more investigation. Note that the ξ_0 value is obtained only for a one dimensional condition and should be implemented by a single characteristic length. If we define L_c as the mean flow path reach to the center of the block from all faces, then we can implement the one-dimensional early time analytical solution to track the time needed to reach to characteristic length. Moreover, developing the early time solution to higher dimensions can help to characterize the transition time to late time condition.

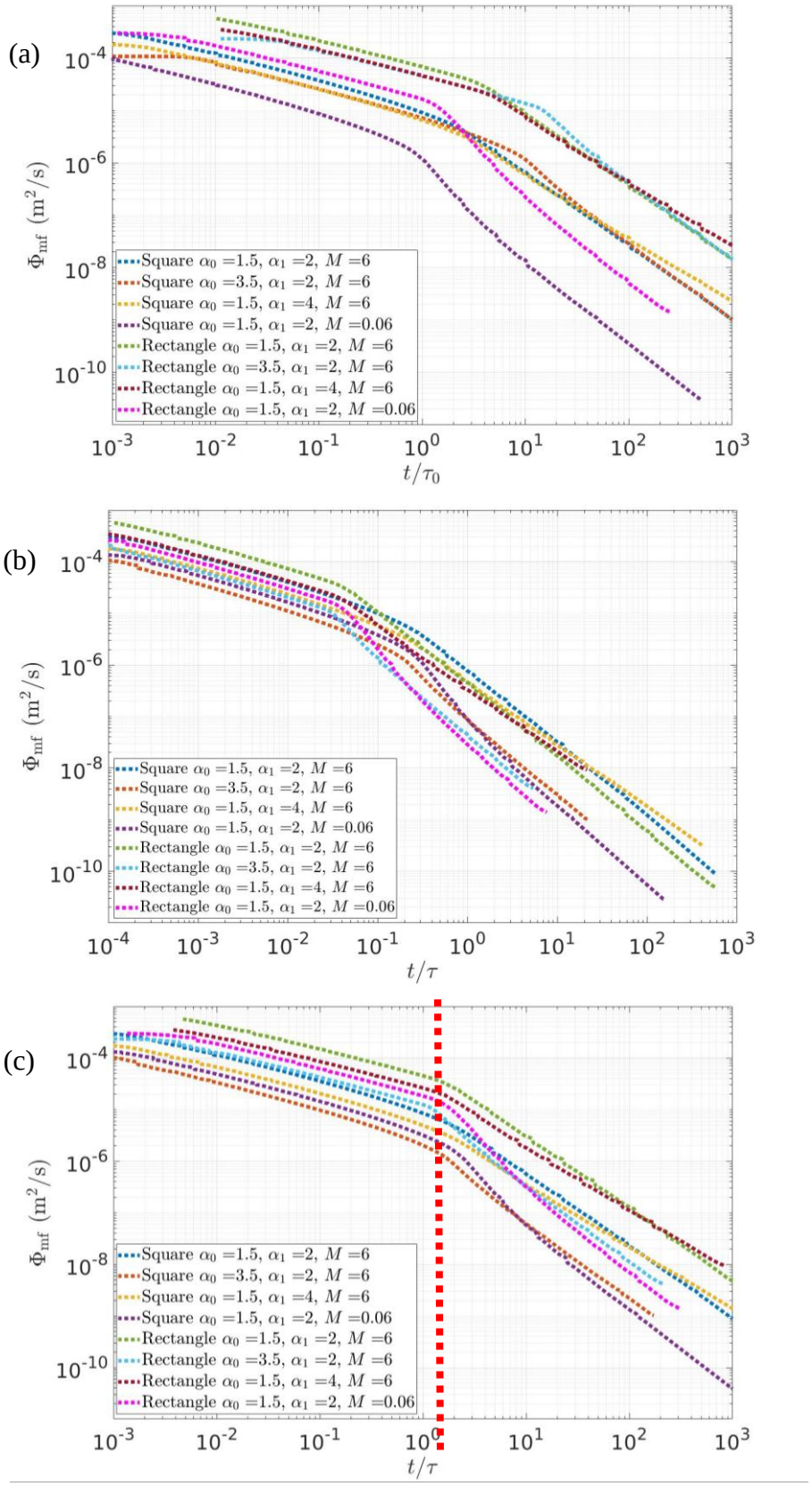


Figure 3-22 Time evolution of the simulated matrix-to-fracture flux for the square and rectangle (see Figure 3-15) with different diffusion coefficient configuration $\alpha_0 = 1.5, 3.5$ $\alpha_1 = 2,4$, $M = 6, 0.06$. The transition between early- and late-times tried to be scaled using three different dimensionless (a) t/τ_0 with $\tau_0 = L_c^2/(4D_0)$, $L_c = L_y$ and t/τ with $\tau = L_c^2/(16\xi_0^2 D_0)$,(b) $L_c = \sqrt{L_x L_y}$, (c) L_c from Eq. 2-18.

Figure 3-22 compares different scaling groups for counter-current capillary imbibition with different non-linear diffusivities in two different shapes of square and rectangle. Obviously, the scaling group including exact early solutions Figure 3-22 (b) and (c) are more accurate. Also, as we can see for those two different proposals of L_c, the characteristic length calculated from the average distance of all faces attempts to scale the transition to $t/\tau \approx 1$ and, gives a better time scaling of the process. However more investigation is demanding for more complex shapes and conditions.

To finish with, the constant flux that can be observed at very short times in Figure 3-21 for the square and the quadrangle should be discarded because they are artifacts related to the domain discretization, the exchange affecting the first row of cells near the domain boundary only. This was verified by further refining the mesh (the plateau shifts to even shorter times).

In summary, a promising very fast and accurate computational approach is emerging, which should eventually make it possible, after some additional efforts, to predict counter-current imbibition over a distribution of blocks of various shapes and sizes, which is more representative of natural porous media.

3.9 Discussion

Counter-current capillary imbibition problem is a highly nonlinear diffusion with singularities at extreme saturation. Taking the asymptotic behaviors at extreme saturation and separating the transfer to early- and late- times (similar to linear diffusion in chapter 2) helped to find some approximation of exact solutions.

An early-time analytical solution for the aqueous phase is adopted with semi-infinite flow conditions in one-dimension. The long-time relaxation of the NAPL saturation inside a matrix block in contact with a wetting fluid has a time dependency (of $\sim t^{-1/\alpha_1}$) in the case of counter-current imbibition in a one-dimensional block.

Firstly, the associated matrix-to-fracture flux term $\Phi_{\mathrm{mf}}(t)$ closure may be represented as being proportional to $\langle 1-S\rangle^{\alpha_1+1}$, the exponent α_1 describing the singularity of the diffusion coefficient with NAPL saturation. Characterization of the flux in both regimes and the transition time between two regimes leads to a full model of inter-porosity calculation. The transition from a Boltzmann square-root regime to an "anomalous" algebraic power-law decay was

confirmed qualitatively and quantitatively by numerical simulations. In the short-time regime, the semi-infinite assumption is quite robust, so the results may remain useful even considering the general fractured media response in that regime. On the other hand, the long-time decay exponent is directly related to input data combining capillary pressure and relative permeabilities features. As in the long-time regime, the NAPL saturation is uniformly small inside the matrix block, the power-law assumption may be expected to be quite robust, controlled by the low NAPL saturation transport properties. The transition between both regimes is sharp, occurring as soon as the toe of the short-time Boltzmann solution reaches half the block size.

Secondly, the same approach was followed for more general matrix blocks in 2 dimensions, under the same counter-current flow regime. The occurrence of such a regime appears to be quite general thanks to a derivation involving the global pressure concept. A similar Ansatz driving the long-time regime was proposed. It predicts a power law time dependency, and the spatial part can be determined using a fast fixed-point algorithm. These findings were confirmed by many comparisons with direct simulations.

Similar results are obtained for the corresponding matrix to fracture flux. A quite sharp transition between a Boltzmann regime involving a $1/\sqrt{t}$ diffusion and the anomalous regime driven by the exponent $1/\alpha_1$ can be observed. That transition corresponds to the interplay between the diffusion scale and the characteristic length scales of the matrix block. A more realistic scaling group of this study improves the characterization of the inter-porosity flux in multi-dimension condition.

3.10 References

Abd, A. S., & Alyafei, N. (2018). Numerical investigation on the effect of boundary conditions on the scaling of spontaneous imbibition. *Oil & Gas Science and Technology – Revue D'ifp Energies Nouvelles*, *73*, 71. https://doi.org/10.2516/ogst/2018060

Abramowitz, M., & Stegun, I. A. (1964). *Handbook of mathematical functions with formulas, graphs, and mathematical tables*. *Applied Mathematics Series*. National Bureau of Standards.

Alyafei, N., Al-Menhali, A., & Blunt, M. J. (2016). Experimental and Analytical Investigation of Spontaneous Imbibition in Water-Wet Carbonates. *Transport in Porous Media*, *115*(1), 189–207. https://doi.org/10.1007/s11242-016-0761-4

Aronofsky, J. S., Masse L., & Natanson S. G. (1958). A Model for the Mechanism of Oil Recovery from the Porous Matrix Due to Water Invasion in Fractured Reservoirs. *Trans.*, *213*(01), 17–19. https://doi.org/10.2118/932-G

Babadagli, T., Hatiboglu, C. U., & Hamida, T. (2009). Evaluation of Matrix-Fracture Transfer Functions for Counter-Current Capillary Imbibition. *Transport in Porous Media*, *80*(1), 17–56. https://doi.org/10.1007/s11242-009-9337-x

Babu, D. K., & Van Genuuchten M. T. (1979, April). A similarity solution to a nonlinear diffusion equation of the singular type: a uniformly valid solution by perturbations. *Quaterly of Applied Mathematics*, *37*, 11–21.

Barenblatt, G. I., Entov, V. M., & Ryzhik, V. M. (1990). *Theory of fluid flows through natural rocks*. Kluwer Academic Publisher.

Bech, N., Jensen, O. K., & Birger, N. (1991). Modeling of Gravity-Imbibition and Gravity-Drainage Processes: Analytic and Numerical Solutions. *SPE Reservoir Engineering*, *6*(01), 129–136. https://doi.org/10.2118/18428-PA

Bekner, B. L., Ishimoto, K., Yamaguchi, S., Firoozabadi, A., & Aziz, K. (Eds.) (1987). *Imbibition-dominated matrix-fracture fluid transfer in dual porosity simulators*. Society of Petroleum Engineers. https://doi.org/10.2118/16981-MS

Bluman, G., & Kumei, S. (1980). On the remarkable nonlinear diffusion equation (∂/∂x)[a (u+b)−2(∂u/∂x)]−(∂u/∂t)=0. *J. Math. Phys*, *21*(1019). https://doi.org/10.1063/1.524550

Blunt, M. J. (2017). *Multiphase Flow in Permeable Media: A Pore-Scale Perspective: Solutions to Equations for Multiphase Flow*. Cambridge University Press. https://doi.org/10.1017/9781316145098

Boltzmann, L. (1894). Zur Integration der Diffusionsgleichung bei variabeln Diffusionscoefficienten. *Annalen Der Physik*, *289*(13), 959–964. https://doi.org/10.1002/andp.18942891315

Bourbiaux, B., & Kalaydjian, F. J. (1990). Experimental Study of Cocurrent and Countercurrent Flows in Natural Porous Media. *SPE Reservoir Engineering*, *5*, 361–368. https://doi.org/10.2118/18283-PA

Brooks, R. H., & Corey, A. T. (1966). Properties of porous media affecting fluid flow. *Journal of the Irrigation and Drainage Division*, *92*(2), 61–90.

Bruce, R. R., & Klute, A. (1956a). The Measurement of Soil Moisture Diffusivity. *Soil Science Society of America Journal*, *20*(4), 458–462. https://doi.org/10.2136/sssaj1956.03615995002000040004x

Bruce, R. R., & Klute, A. (1956b). The Measurement of Soil Moisture Diffusivity. *Soil Science Society of America Journal*, *20*(4), 458–462. https://doi.org/10.2136/sssaj1956.03615995002000040004x

Brusseau, M. L. (1992). Rate- limited mass transfer and transport of organic solutes in porous media that contain immobile immiscible organic liquid. *Water Resources Research*, *28*(1), 33–45. doi:10.1029/91WR02498

Brutsaert, W. (1968). The Adaptability of an Exact Solution to Horizontal Infiltration. *Water Resources Research*, *4*(4), 785–789. https://doi.org/10.1029/WR004i004p00785

Brutsaert, W., & Weisman, R. N. (1970). Comparison of Solutions of a Nonlinear Diffusion Equation. *Water Resources Research*, *6*(2), 642–644. https://doi.org/10.1029/WR006i002p00642

Buckley, S. E., & Leverett, M. C. (1942). Mechanism of Fluid Displacement in Sands. *Trans.*, *146*(01), 107–116. https://doi.org/10.2118/942107-G

Burdine, N. T. (1953). Relative permeability calculations from pore size distribution data. *Petroleum Transactions AIME*, *198*, 71–78.

Chen, J., Miller, M. A., & Sepehrnoori, K. (Eds.) (1995). *Theoretical Investigation of Countercurrent Imbibition in Fractured Reservoir Matrix Blocks*. *SPE Reservoir Simulation Conference: All Days*.

Chen, Z.‐X., Bodvarsson, G. S., & Witherspoon, P. A. (1992). Comment on "Exact integral solutions for two-phase flow" by David B. McWhorter and Daniel K. Sunada. *Water Resources Research*, *28*(5), 1477–1478. https://doi.org/10.1029/92WR00473

Cherblanc, f., Ahmadi, A., & Quintard, M. (2003). Two-medium description of dispersion in heterogeneous porous media: calculation of macroscopic properties. *Water Resources Research*, *39*(6), 1154.

Chevalier, T., Labaume, J., Delbos, A., Clemens, T., Waeger, V. M., Bourbiaux, B., & Fleury, M. (2019). A Practical Methodology to Screen Oil Recovery Processes Involving Spontaneous Imbibition. *Transport in Porous Media*, *127*, 729–743. https://doi.org/10.1007/s11242-018-01229-z

Gennes, P. G. d., Brochard-Wyart, F., & Quéré, D. (2004). *Capillary and wetting phenomena: Drops, bubbles, perals, waves*. Springer-Verlag.

Guo, H., Song, K., & Hilfer, R. (2022). A Brief Review of Capillary Number and its Use in Capillary Desaturation Curves. *Transport in Porous Media*, *144*(1), 3–31. https://doi.org/10.1007/s11242-021-01743-7

Guy Chavent, & Jerome Jaffre (Eds.). (1986). *Studies in Mathematics and Its Applications*. *Mathematical Models and Finite Elements for Reservoir Simulation*. ELSEVIER.

Handy, L. L. (1960). Determination of Effective Capillary Pressures for Porous Media from Imbibition Data. *Trans.*, *219*(01), 75–80.

Hansen, A., Flekkøy, E. G., & Baldelli, B. (2020). Anomalous Diffusion in Systems with Concentration-Dependent Diffusivity: Exact Solutions and Particle Simulations. *Frontiers in Physics*, *8*, Article 519624. https://doi.org/10.3389/fphy.2020.519624

Hatiboglu, C. U., & Babadagli, T. (2010). Experimental and visual analysis of co- and counter-current spontaneous imbibition for different viscosity ratios, interfacial tensions, and wettabilities. *Journal of Petroleum Science and Engineering*, *70*(3), 214–228. https://doi.org/10.1016/j.petrol.2009.11.013

Heaslet, M. A., & Alksne, A. (1961). Diffusion from a fixed surface with a concentration-dependent coefficient. *Journal of Society for Industrial and Applied Mathematics*, *9*(4), 584–596.

Hecht, F. (2012). New development in FreeFem++. *J. Numer. Math.*, *20*(3-4, PAGES = 251-265). https://freefem.org/

Hristov, J. (2015). An approximate analytical (integral-balance) solution to a nonlinear heat diffusion equation. *Thermal Science*, *19*(2), 723–733. https://doi.org/10.2298/TSCI140326074H

Hristov, J. (2016). Integral solutions to transient nonlinear heat (mass) diffusion with a power-law diffusivity: a semi-infinite medium with fixed boundary conditions. *Heat and Mass Transfer*, *52*(3), 635–655. https://doi.org/10.1007/s00231-015-1579-2

Kashchiev, D., & Firoozabadi, A. (2003, December). Analytical Solutions for 1D Countercurrent Imbibition in Water-Wet Media. *SPE Journal*, 401–408.

Kewen Li, SPE, and Roland N. Horne, & Stanford U. (2006). Generalized Scaling Approach for Spontaneous Imbibition: An Analytical Model. *SPE Reservoir Evaluation & Engineering*, *9*(3), 251–258.

Kleppe, J., & Morse, R. A. (Eds.) (1974). *Oil Production from Fractured Reservoirs by Water Displacement*. *SPE Annual Technical Conference and Exhibition: All Days*.

Klute, A. (1952). A NUMERICAL METHOD FOR SOLVING THE FLOW EQUATION FOR WATER IN UNSATURATED MATERIALS. *Soil Science*, *73*(2), 105–116. https://journals.lww.com/soilsci/Fulltext/1952/02000/A_NUMERICAL_METHOD_FOR_SOLVING_THE_FLOW_EQUATION.3.aspx

Lake, L. W. (1989). *Enhanced Oil Recovery* (1st). Prentice Hall.

Lamb, H. (1932). *Hydrodynamics* (Sixth). Cambridge University Press.

Landau, L. D., & Lifshitz, E. M. (1987). *Fluid mechanics* (Second). Pergamon Press.

Landereau, P., Noetinger, B., & Quintard, M. (2001). Quasi-steady two-equation models for diffusive transport in fractured porous media: large-scale properties for densely fractured systems. *Advances in Water Resources*, *24*, 863–876.

Leverett, M. C. (1941). Capillary behaviour in porous solids. *Transactions of the AIME*, *142*, 159–172.

Li, K., & Zhao, H. (2012). Fractal Prediction Model of Spontaneous Imbibition Rate. *Transport in Porous Media*, *91*(2), 363–376. https://doi.org/10.1007/s11242-011-9848-0

Li, L., Wang, M., Shi, A.‐F., Liu, Z.‐F., & Wang, X.‐H. (2020). An approximate analytical solution for one-dimensional imbibition problem in low-permeability porous media. *Journal of Porous Media*, *23*(7), 683–694.

Lucas, R. (1918). Ueber das Zeitgesetz des kapillaren Aufstiegs von Flüssigkeiten. *Kolloid-Zeitschrift*, *23*(1), 15–22. https://doi.org/10.1007/BF01461107

M. A. Heaslet, & A. Alksne (1961). Diffusion from a fixed surface with a concentration-dependent coefficient. *J. Soc. Indust. Appl. Math.*, *9*(4), 584–596.

Ma, S., Morrow, N. R., & Zhang, X. (1997). Generalized scaling of spontaneous imbibition data for strongly water-wet systems. *Journal of Petroleum Science and Engineering*, *18*(3), 165–178. https://doi.org/10.1016/S0920-4105(97)00020-X

March, R., Doster, F., & Geiger, S. (2016). Accurate early- time and late- time modeling of countercurrent spontaneous imbibition. *Water Resources Research*, *52*(8), 6263–6276. https://doi.org/10.1002/2015WR018456

Mason, G., & Morrow, N. R. (2013). Developments in spontaneous imbibition and possibilities for future work. *Journal of Petroleum Science and Engineering*, *110*, 268–293. https://doi.org/10.1016/j.petrol.2013.08.018

Mattax C. C., & Kyte J. R. (1962). Imbibition Oil Recovery from Fractured, Water-Drive Reservoir. *SPE Journal*, *2*(02), 177–184. https://doi.org/10.2118/187-PA

McWhorter, D. B., & Sunada, D. K. (1990). Exact integral solutions for two- phase flow. *Water Resources Research*, *26*(3), 399–413. https://doi.org/10.1029/WR026i003p00399

Morrow, N. R., & G. Mason (2001). Recovery of oil by spontaneous imbibition. *Current Opinion in Colloid & Interface Science*, *6*(4), 321–337. doi:10.1016/S1359-0294(01)00100-

Noetinger, B. (2015). A quasi steady state method for solving transient Darcy flow in complex 3D fractured networks accounting for matrix to fracture flow. *Journal of Computational Physics*, *283*, 205–223.

Noetinger, B., Estebenet, T., & Landereau, P. (2001). A direct determination of the transient exchange term of fractured media using a continuous time random walk method. *Transport in Porous Media*, *44*(3), 539–557.

Noetinger, B., & Jarrige, N. (2012). A quasi steady state method for solving transient Darcy flow in complex 3D fractured networks. *Journal of Computational Physics*, *231*(1), 23–38.

Noetinger, B., Roubinet, D., Russian, A., Le Borgne, T., Delay, F., Dentz, M., Dreuzy, J.‐R. de, & Gouze, P. (2016). Random walk methods for modeling hydrodynamic transport in porous and fractured media from pore to reservoir scale. *Transport in Porous Media*, *115*(2), 345–385.

Nooruddin, H. A., & Blunt, M. J. (2016). Analytical and numerical investigations of spontaneous imbibition in porous media. *Water Resources Research*, *52*(9), 7284–7310. https://doi.org/10.1002/2015WR018451

Parlange, J.‐Y., Lisle, I. G., Prasad, S. N., & Romkens, M. J. M. (1984). Wetting Front Analysis of the Nonlinear Diffusion Equation. *Water Resources Research*, *20*(5), 636–638. https://doi.org/10.1029/WR020i005p00636

Parlange, M. B., Prasad, S. N., Parlange, J.‐Y., & Romkens, M. J. M. (1992). Extension of the HeasletAlksne Technique to arbitrary soil water diffusivities. *Water Resources Research*, *28*(10), 2793–2797. https://doi.org/10.1029/92WR01683

Philip, J. R. (1955a). Numerical solution of equations of the diffusion type with diffusivity concentration-dependent. *Trans. Faraday Soc.*, *51*(0), 885–892. https://doi.org/10.1039/TF9555100885

Philip, J. R. (1955b). Numerical solution of equations of the diffusion type with diffusivity concentration-dependent. *Transactions of the Faraday Society*, *51*, 885–892. DOI:10.1039/TF9555100885

Pooladi-Darvish, M., & Firoozabadi, A. (2000). Cocurrent and Countercurrent Imbibition in a Water-Wet Matrix Block. *SPE Journal*, *5*(01), 3–11. https://doi.org/10.2118/38443-PA

Purcell, W. R. (1949). Capillary pressure - - their measurement using mercury and the calculation of permeability therefrom. *Petroleum Transactions AIME*, 39–48.

Rangel-German, E. R., & Kovscek, A. R. (2006). Time-dependent matrix-fracture shape factors for partially and completely immersed fractures. *Journal of Petroleum Science and Engineering*, *54*, 149–163. https://doi.org/10.1016/j.petrol.2006.08.004

Rapoport, L. A. (1955). Scaling Laws for Use in Design and Operation of Water-Oil Flow Models. *Trans.*, *204*(01), 143–150.

Rose, W. D. Relative permeability ideas - - then and now (from Richards to Leverett to Yuster, and beyond. In

Ruth, D. W., Li, Y., Mason, G., & Morrow, N. (2007). An Approximate Analytical Solution for Counter-Current Spontaneous Imbibition. *Transport in Porous Media*, *66*(3), 373–390. https://doi.org/10.1007/s11242-006-0019-7

Saboorian-Jooybari, H., Ashoori, S., & Mowazi, G. (2012). Development of an Analytical Time-Dependent Matrix/Fracture Shape Factor for Countercurrent Imbibition in Simulation of Fractured Reservoirs. *Transport in Porous Media*, *92*(687-708). https://doi.org/10.1007/s11242-011-9928-1

Schmid, K. S., Alyafei, N., Geiger, S., & Blunt, M. J. (2016). Analytical Solutions for Spontaneous Imbibition: Fractional-Flow Theory and Experimental Analysis. *SPE Journal*, *21*(06), 2308–2316. https://doi.org/10.2118/184393-PA

Schmid, K. S., & Geiger, S. (2012). Universal scaling of spontaneous imbibition for water-wet systems. *Water Resources Research*, *48*(3). https://doi.org/10.1029/2011WR011566

Schmid, K. S., Geiger, S., & Sorbie, K. S. (2011). Semianalytical solutions for cocurrent and countercurrent imbibition and dispersion of solutes in immiscible two-phase flow. *Water Resources Research*, *47*(2). https://doi.org/10.1029/2010WR009686

Silin, D., & Patzek, T. (2004). On Barenblatt's Model of Spontaneous Countercurrent Imbibition. *Transport in Porous Media*, *54*(3), 297–322. https://doi.org/10.1023/B:TIPM.0000003678.85526.b1

Standing, M. B. (1975). *Notes on relative permeability relationships*.

Swaan, A. de, & Ramirez-Villa, M. (1993). Functions of flow from porous rock blocks. *Journal of Petroleum Science and Engineering*, *9*(1), 39–48. https://doi.org/10.1016/0920-4105(93)90027-C

Tavassoli, Z., Zimmerman, R. W., & Blunt, M. J. (2005a). Analysis of counter-current imbibition with gravity in weakly water-wet systems. *Journal of Petroleum Science and Engineering*, *48*(1-2), 94–104. https://doi.org/10.1016/j.petrol.2005.04.003

Tavassoli, Z., Zimmerman, R. W., & Blunt, M. J. (2005b). Analytical analysis for oil recovery during counter-current imbibition in strongly water-wet systems. *Transport in Porous Media*, *58*, 173–189.

Tritton, D. J. (1988). *Physical fluid dynamics* (Second). Clarendon Press, Oxford.

Washburn, E. W. (1921). The Dynamics of Capillary Flow. *Phys. Rev.*, *17*(3), 273–283. https://link.aps.org/doi/10.1103/PhysRev.17.273

Wolff, M. (1987). *Geologically Based Fractured Reservoir Simulator.* The University of Taxas at Austin, Austin.

Wyllie, M. R. J., & Gardner, G. H. F. (1958a). The generalized Kozeny-Carman equation: its application to problems of multiphase flow in porous, part 2 - - A novel approach to problems of fluid flow. *World Oil, Production Section*, 210–228.

Wyllie, M. R. J., & Gardner, G. H. F. (1958b). The generalized Kozeny-Carman equation: its application to problems of multiphase flow in porous, Part 1 - - Review of existing theories. *World Oil, Production Section*, 121–126.

Wyllie, M. R. J., & Rose, W. D. (1950). Some theoretical considerations related to the quantitative evaluation of the physical characteristics of reservoir rock from electrical log data. *Petroleum Transactions AIME*, *189*, 105–118.

Wyllie, M. R. J., & Spangler, M. B. (1952). Application of electrical resistivity measurements to problem of fluid flow in porous media. *Bulletin of the American Association of Petroleum Geologists*, *36*(2), 359–403.

Zhou, D., Jia, L., Kamath, J., & Kovscek, A. (2002). Scaling of counter-current imbibition processes in low-permeability porous media. *Journal of Petroleum Science and Engineering*, *33*(1), 61–74. https://doi.org/10.1016/S0920-4105(01)00176-0

Zimmerman, R., & Bodvarsson, G. (1991). A simple approximate solution for horizontal infiltration in a Brooks-Corey medium. *Transport in Porous Media*, *6*(2), 195–205. https://doi.org/10.1007/BF00179281

Conclusions and perspectives

Our study started with a discussion of dual-medium models describing flow in fracture media. These up-scaled models depend on the initial boundary condition and the transfer mechanisms which are single- or two-phase diffusive flow in this study. Matrix-fracture inter-porosity flux is a key player in the fluid flow in fractured porous media. This inter-porosity flux was initially approximated by a linear closure with a constant coefficient, which is called the shape factor. We developed the analytical solutions for linear and non-linear diffusive flow in a matrix-fracture system to tune the shape factor and our study achieved the following concluding points:

- The classical dual-medium averaging approach with a constant shape factor does not allow for good approximations of matrix-fracture flux, especially for transient early time transfers.
- In the case of a constant diffusion coefficient, the preliminary study of a matrix-fracture system enabled us to set up and validate a methodology to undertake the study of up-scaling issues of the dual-medium model that underlies the simulation of matrix-fracture transfers.
- In that case, the analytical solution is associated with Warren and Root formulation to derive the matrix-fracture transfer expression. This transfer model includes two periods of early times (transient or infinite acting) transfer and late times ($t \to \infty$) transfer. A constant shape factor does not approximate the early time flux.
- Analytical shape factor formulation is a series solution that is singular (varying as $t^{-1/2}$) at early-times and that converges to an asymptotic constant value at late times.
- Numerical dual-medium model can underestimate or over-estimate the inter-porosity flux based on the choice of shape factor constant. Matching a dual-medium model based on a constant shape factor equation cannot describe the whole transfer that is transient by essence.
- A non-linear variation of the shape factor matches the conventional dual-medium to fine-grid or analytical solution from early to late times.

- Thanks to the introduction of the *global pressure* approach, we proved that the imbibition of a matrix block embedded in water is driven by a counter current equation (in the case of negligible gravity).
- Counter-current capillary imbibition is driven by a non-linear diffusion equation that presents a singularity at extreme saturations. Few analytical solutions are available over the entire range of time scales.
- The asymptotic behavior of the diffusion function at extreme saturation helps to develop an analytical approximation of the solution in the one-dimensional domain. The asymptotic behavior depends on the rock/fluid properties.
- Two regimes of early- and late-time flux are quantified in all analytical, numerical, and experimental solutions.
- The self-similar analytical solution gives an excellent approximation of the counter-current imbibition. Our investigation on higher-order approximation adjusts the old solution and the numerical calculations totally converge to the analytical ones.
- The analytical solutions give the exact matrix-fracture counter-current imbibition flux in a one-dimensional block at both early- and late-time regimes.
- The flux variation at early times does not depend on the diffusion exponents ($\sim t^{-1/2}$), while it depends on the relative permeability (a_1) exponent of NAPL ($\sim t^{-1/a_1}$) at late time. This change of slope gives a sharp cross-over between two regimes, which is smoother for multi-dimensional and non-symmetrical blocks.
- The diffusion coefficient and block length characterize the transition time between early- and late-times.
- The late-time asymptotic solution converges to the exact solution for long times (when there is little NAPL in the block), and the rate of convergence depends on the exponent a_1.
- The early time self-similar analytical solution is limited to the one-dimensional domain.
- The late-time asymptotic solution (with the power-law dependency of the diffusion coefficient) is general to two- and three-dimensions using the same separation of space and time.
- A fast-converging fixed-point algorithm is useful to find the spatial dependency of the solution. This semi-analytical solution is compared with numerical calculation and is trustworthy on any arbitrary size and shape of matrix block.

– The asymptotic behaviors and corresponding inter-porosity flux variation slopes, along with a correct characteristic time, approximate the full dynamic range of counter-current capillary imbibition flux in any arbitrary matrix block domain.

These findings pave the way to research leading to a more faithful description of the matrix-fracture exchanges when considering a realistic fractured medium composed of a population of matrix blocks of various sizes and shapes. Looking for simple geometric descriptors quantifying the transition time between diffusion regimes will be of interest for such applications. In parallel, developing averaging methods lumping these various matrix blocks within one macro-scale single exchange flux description will be another research avenue. To end this study, the following points require further investigation:

– Other boundary conditions like variable saturation or concentration should be considered for both linear and non-linear PDE of diffusion transfer in chapters 2 and 3.
– A generalization of Parlange solution at early-times and in any dimension of space might be worth investigating, although nothing simple is apparent at first sight.
– Late-time estimates of $(t/\tau_0)_\infty$, such that the fixed-point asymptotic solution obtained for $t \to \infty$ is valid and the flux prefactor A_∞ is accurately computed, should be consolidated.
– The rate of convergence between late-time analytical solution and numerical calculation depends on the asymptotic behavior and can be further investigated.
– The relevant characteristic length, involved in the diffusion time τ_0, should be determined beforehand as previously discussed, to make $(t/\tau_0)_\infty$ estimates generic (indeed, if the timescale differs from one geometry to another, determining $(t/\tau_0)_\infty$ on a case-by-case basis may be tedious). Different approaches to calculate characteristic length (L_c) of 3D matrix blocks are worth investigating.
– Matrix-fracture transfer includes a combination of simultaneous different transfer mechanisms (viscous flow, capillary imbibition, molecular diffusion, and gravity). A further investigation on relative characteristic time is suggested.

Annex A. Puma reservoir numerical discretization and discrete equations

The numerical modeling of multi-phase flow in porous media has been extensively studied using different computational approaches such as Finite Difference, Finite Element and Finite Volume methods. Industrial numerical simulators are generally based on the FV method (Finite Volume method) because the FV method conserves mass fluxes by construction. Before detailing the discrete equation, let first introduce a numerical discretization of the reservoir. Let consider a finite volume mesh of our reservoir as dawned in Figure A-1.

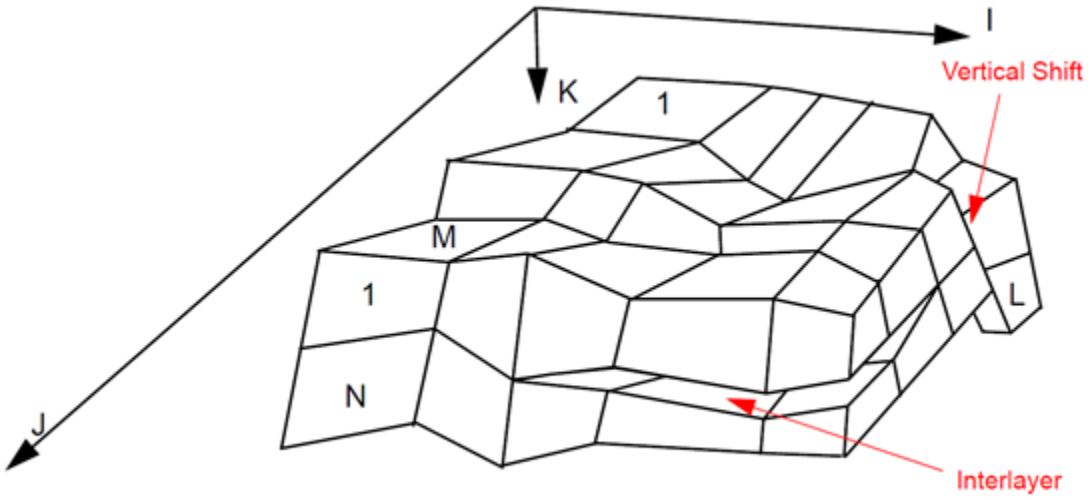


Figure A-1 Example of discretization of a complex mesh in cartesian coordinate to show the capability of a numerical simulator (figure from the technical manual of PumaFlow)

The mesh is constituted of control volumes or cells denoted $\mathfrak{C}_i$ as illustrated in Figure A-2. For any cell $\mathfrak{C}_i$, we note v_i its volume. We note $\mathcal{N}(\mathfrak{C}_i) = \{\mathfrak{C}_j | \mathfrak{C}_j \cap \mathfrak{C}_i \neq \emptyset\}$ the set of neighboring cells of the cell $\mathfrak{C}_i$. For any cell $\mathfrak{C}_j \in \mathcal{N}(\mathfrak{C}_i)$, we note $\boldsymbol{n}_{i,j}$ the unit normal of the surface that separates the cells $\mathfrak{C}_i$ and $\mathfrak{C}_j$ directed from $\mathfrak{C}_i$ to $\mathfrak{C}_j$ and $A_{i,j}$ the area of this surface.

For the sake of brevity, we detail the finite volume scheme for components in the fracture media only; the finite volume scheme for components in the matrix medium can be deduced easily in the same manner. Integrating the equations (Eq. B-2 herein), over a space time interval $\mathfrak{C}_i \times [t^n, t^{n+1} = t^n + \Delta t]$ we obtain:

$$\int_{\mathfrak{C}_i}\int_{t^n}^{t^n+\Delta t}\frac{\partial}{\partial t}\left[\phi^f\sum_{\varphi}(\rho_\varphi^f C_{\varphi k}^f S_\varphi^f)\right]dt\,dv$$
$$+\int_{\mathfrak{C}_i}\int_{t^n}^{t^n+\Delta t} div\left[\sum_{\varphi}(\rho_\varphi^f C_{\varphi k}^f \boldsymbol{u}_\varphi^f)+\boldsymbol{J}_{\varphi k}^f\right]dt\,dv \qquad \text{Eq. A-1}$$
$$+\int_{\mathfrak{C}_i}\int_{t^n}^{t^n+\Delta t}\sum_{\varphi}\left(\rho_\varphi^f C_{\varphi k}^f Q_\varphi^f\right)dt\,dv-\int_{\mathfrak{C}_i}\int_{t^n}^{t^n+\Delta t}F_{\varphi k}^{mf}\,dt\,dv=0.$$

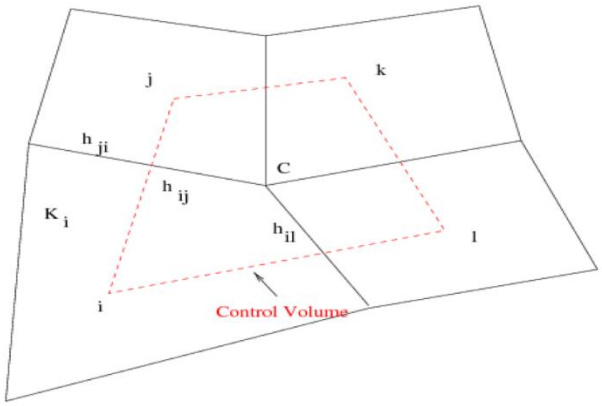


Figure A-2 Example of control volume for a 2-D mesh (figure from the technical manual of PumaFlow)

Now, we define average values over each cell $\mathfrak{C}_i$ for each discrete time t^n for the fracture porosity:

$$(\phi^f)_i^n=\frac{1}{v_i}\int_{\mathfrak{C}_i}\phi^f(x,t^n)\,dv, \qquad \text{Eq. A-2}$$

and for the mass of the component k:

$$(\phi^f)_i^n\left(\sum_{\varphi}(\rho_\varphi^f C_{\varphi k}^f S_\varphi^f)\right)_i^n=\int_{\mathfrak{C}_i}\phi^f(x,t^n)\sum_{\varphi}\rho_\varphi^f(x,t^n)\,C_{\varphi k}^f(x,t^n)\,S_\varphi^f(x,t^n)\,dv, \qquad \text{Eq. A-3}$$

$$\int_{\mathfrak{C}_i}\int_{t^n}^{t^n+\Delta t}\frac{\partial}{\partial t}\left[\phi^f\sum_{\varphi}\left(\rho_\varphi^f C_{\varphi k}^f S_\varphi^f\right)\right]dv\,dt$$
$$=v_i\left((\phi^f)_i^{n+1}\left(\sum_{\varphi}(\rho_\varphi^f C_{\varphi k}^f S_\varphi^f)\right)_i^{n+1}-(\phi^f)_i^n\left(\sum_{\varphi}(\rho_\varphi^f C_{\varphi k}^f S_\varphi^f)\right)_i^n\right). \qquad \text{Eq. A-4}$$

Now, applying the divergence theorem to the divergence of the advection and diffusion/dispersion terms, we obtain:

$$\int_{t^n}^{t^n+\Delta t}\int_{\mathfrak{C}_i} div\left[\sum_{\varphi}\left(\rho_\varphi^f C_{\varphi k}^f \boldsymbol{u}_\varphi^f\right)+\boldsymbol{J}_{k\varphi}^f\right] dv\, dt = \int_{t^n}^{t^n+\Delta t}\int_{\partial\mathfrak{C}_i}\left(\sum_{\varphi}\left(\rho_\varphi^f C_{\varphi k}^f \boldsymbol{u}_\varphi^f\right)+\boldsymbol{J}_{\varphi k}^f\right)\cdot d\boldsymbol{n}_{\partial\mathfrak{C}_i}\, dt. \quad \text{Eq. A-5}$$

To approximate the advection term, we consider whether the IMPES (implicit for pressure, explicit for other variables) upwind scheme or the Fully IMPLICIT (implicit for all variables) upwind scheme. Both schemes write:

$$\int_{t^n}^{t^n+\Delta t}\int_{\mathfrak{C}_i} div\left(\sum_{\varphi}\left(\rho_\varphi^f C_{\varphi k}^f \boldsymbol{u}_\varphi^f\right)\right) dv\, dt \approx \Delta t \sum_{\mathfrak{C}_j\in\mathcal{N}(\mathfrak{C}_i)}\sum_{\varphi} A_{i,j}\left(\rho_\varphi^f C_{\varphi k}^f \boldsymbol{u}_\varphi^f\right)_{i,j}^{l}\cdot \boldsymbol{n}_{i,j}, \quad \text{Eq. A-6}$$

where $\left(\rho_\varphi^f C_{\varphi k}^f \boldsymbol{u}_\varphi^f\right)_{i,j}^{l}$ is an approximation of the advection flux at the interface between cell $\mathfrak{C}_i$ and cell $\mathfrak{C}_j$. An upwind scheme is used:

$$\left(\rho_\varphi^f C_{\varphi k}^f \boldsymbol{u}_\varphi^f\right)_{i,j}^{l} = \begin{cases}\left(\rho_\varphi^f C_{\varphi k}^f \boldsymbol{u}_\varphi^f\right)_{i}^{l} \; if\; \Delta_{i,j}(\Phi_\varphi^f)^{n+1}\geq 0\\ \left(\rho_\varphi^f C_{\varphi k}^f \boldsymbol{u}_\varphi^f\right)_{j}^{l} \; if\; \Delta_{i,j}(\Phi_\varphi^f)^{n+1} > 0\end{cases}, \quad \text{Eq. A-7}$$

where Φ_φ^{n+1} are the phases potential which write for the water, the oil and the gas phases:

$$\Delta_{i,j}(\Phi_w^f)^{n+1} = \left(\left(P^f\right)_j^{n+1} - \left(Pc_w^f\right)_j^{l}\right) - \left(\left(P^f\right)_i^{n+1} - \left(Pc_w^f\right)_i^{l}\right) - \left(\overline{\rho_w^f}\right)_{i,j}^{l}\boldsymbol{g}\cdot(\vec{x}_j-\vec{x}_i) \quad \text{Eq. A-8}$$

$$\Delta_{i,j}(\Phi_o^f)^{n+1} = \left(P^f\right)_j^{n+1} - \left(P^f\right)_i^{n+1} - \left(\overline{\rho_o^f}\right)_{i,j}^{l}\boldsymbol{g}\cdot(\vec{x}_j-\vec{x}_i) \quad \text{Eq. A-9}$$

$$\Delta_{i,j}(\Phi_g^f)^{n+1} = \left(\left(P^f\right)_j^{n+1} + \left(Pc_g^f\right)_j^{l}\right) - \left(\left(P^f\right)_i^{n+1} + \left(Pc_g^f\right)_i^{l}\right) - \left(\overline{\rho_g^f}\right)_{i,j}^{l}\boldsymbol{g}\cdot(\vec{x}_j-\vec{x}_i). \quad \text{Eq. A-10}$$

Let us recall that P^f is the oil pressure (also denoted reference pressure) in the fracture, $Pc_w^f = P_o^f - P_w^f$ and $Pc_g^f = P_o^f - P_g^f$ are the water and gas capillary pressure, which depends respectively on the water and gas saturation. $\boldsymbol{g}$ is the gravity and $\vec{x}_i$ and $\vec{x}_j$ the coordinates of the center of cell $\mathfrak{C}_i$ and cell $\mathfrak{C}_j$. $\overline{\rho_w^f}$, $\overline{\rho_w^f}$ and $\overline{\rho_w^f}$ are respectively average values (not given here) of the water, oil and gas densities on the two neighboring cells. To end with, when the

index $l = n$ we recover the IMPES scheme and when the index $l = n + 1$ we recover the **Fully IMPLICIT** scheme.

For the diffusion dispersion term, we use the following scheme:

$$\int_{t^n}^{t^n+\Delta t} \int_{v_i} div(\boldsymbol{J}_{\varphi k}^f)\, dv\, dt \approx \Delta t \sum_{\mathfrak{C}\in\mathcal{N}(\mathfrak{C}_i)} \sum_{\varphi} A_{i,j} \left(\boldsymbol{J}_{\varphi k}^f\right)_{i,j}^l \cdot \boldsymbol{n}_{i,j}, \qquad \text{Eq. A-11}$$

where, for each phase we take:

$$\left(\boldsymbol{J}_{\varphi k}^f\right)_{i,j}^l = -\left(\phi^f \rho_\varphi^f S_\varphi^f\right)_i^l \overline{D}_{i,j} \frac{\left(C_{\varphi k}^f\right)_j^l - \left(C_{\varphi k}^f\right)_i^l}{(\vec{x}_j - \vec{x}_i)\cdot \overrightarrow{n}_{i,j}}, \qquad \text{Eq. A-12}$$

with $\overline{D}_{i,j}^{eff}$ an effective diffusion/dispersion coefficient given by:

$$\overline{D}_{i,j} = \overline{\overline{D_{\varphi k}}} + \frac{\left\|\boldsymbol{u}_\varphi^f\right\|_{i,j}^n}{\left(\phi^f S_\varphi^f\right)_i^m} \beta^f. \qquad \text{Eq. A-13}$$

Again, if we take $l = n$ we recover an explicit scheme that is known to require a quite troublesome stability condition because the diffusion/equation term is parabolic. Thus, an implicit scheme ($l = n + 1$) will be systematically used.

Regarding the source term and matrix/fracture exchange term, we simply use averages over the space time interval $\mathfrak{C}_i \times [t^n, t^n + \Delta t]$:

$$\int_{\mathfrak{C}_i} \int_{t^n}^{t^n+\Delta t} \sum_{\varphi} \left(\rho_\varphi^f C_{\varphi k}^f Q_\varphi^f\right) dv\, dt = \Delta t v_i \left(\rho_\varphi^f C_{\varphi k}^f Q_\varphi^f\right)_i^l, \qquad \text{Eq. A-14}$$

and:

$$\int_{\mathfrak{C}_i} \int_{t^n}^{t^n+\Delta t} F_{\varphi k}^{mf}\, dv\, dt = \Delta t v_i \left(F_{\varphi k}^{mf}\right)_i^l. \qquad \text{Eq. A-15}$$

Then, the numerical finite volume upwind scheme for the mass conservation of components in the fracture medium writes:

$$\frac{(\phi^f)_i^{n+1}\left(\sum_\varphi\left(\rho_\varphi^f C_{\varphi k}^f S_\varphi^f\right)\right)_i^{n+1} - (\phi^f)_i^n\left(\sum_\varphi\left(\rho_\varphi^f C_{\varphi k}^f S_\varphi^f\right)\right)_i^n}{\Delta t}$$
$$+\frac{1}{v_i}\sum_{\mathbb{C}_j\in\mathcal{N}(\mathbb{C}_i)}\sum_\varphi A_{i,j}\left(\left(\rho_\varphi^f C_{\varphi k}^f \boldsymbol{u}_\varphi^f\right)_{i,j}^l\right. \qquad \text{Eq. A-16}$$
$$\left. -\left(\phi^f\rho_\varphi^f S_\varphi^f\right)_i^m \bar{D}_{i,j}^{eff}\,\frac{\left(C_{\varphi k}^f\right)_j^m - \left(C_{\varphi k}^f\right)_i^m}{(\vec{x}_j-\vec{x}_i)\cdot\vec{n}_{i,j}}\right)\cdot\boldsymbol{n}_{i,j} + \left(\rho_\varphi^f C_{\varphi k}^f Q_\varphi^f\right)_i^l - \left(F_{\varphi k}^{mf}\right)_i^l = 0.$$

Applying the same strategy on the mass conservation of components in the matrix medium, we obtain the following numerical scheme:

$$\frac{(\phi^m)_i^{n+1}\left(\sum_\varphi(\rho_\varphi^m C_{\varphi k}^m S_\varphi^m)\right)_i^{n+1} - (\phi^m)_i^n\left(\sum_\varphi(\rho_\varphi^m C_{\varphi k}^m S_\varphi^m)\right)_i^n}{\Delta t} + \left(\rho_\varphi^m C_{\varphi k}^m Q_\varphi^m\right)_i^l + \left(F_{\varphi k}^{mf}\right)_i^l = 0. \qquad \text{Eq. A-17}$$

Despite this scheme being widely used by reservoir engineers, it is known to include a numerical viscosity. This numerical viscosity results in the presence of an additional artificial diffusion noticeable in the numerical results. It can whether totally spoil the physics of the results for coarse meshes or be negligible to obtain a good match of the physics for sufficiently fine meshes. This numerical viscosity is essential for the scheme stability, so it can be reduced to a certain extent (with more sophisticated schemes for example) but it can never be totally suppressed.

Convergence study

The numerical diffusion of numerical schemes is usually quantified by deriving equivalent equations (continuous equations) from the discrete equations of the considered scheme. The goal of this section is to demonstrate how to select the cell mesh size and the time step to obtain a negligible numerical diffusion while maintaining a reasonable computational time. For that purpose, the convergence of simulation results with grid size refinement has been studied with comparison with the exact solution. In fact, numerical results are known to be dissipative compared to exact solutions because numerical schemes generate an "artificial" diffusion called numerical diffusion. This numerical diffusion is essential for the numerical schemes stability, but it must be controlled as much as possible in order to preserve the numerical solutions accuracy. Depending on the numerical scheme used, the mesh cell size and time step size, the numerical diffusion can be either so high that the physical behavior of the

solution cannot be deduced from the numerical results or sufficiently small to ensure a good match of the modeled physics.

Mesh convergence determines how many calculation grid points are required in a model to ensure that the results are not affected significantly by changing the grid cell number. In fact, numerical results are known to be dissipative compared to exact solutions because numerical schemes generate an "artificial" diffusion called numerical diffusion. This numerical diffusion is essential for the numerical schemes stability, but it must be controlled as much as possible in order to preserve the numerical solutions accuracy.

To study the effect of cell grid size on diffusion solution we have chosen fine to coarse discretized grid cells, including 100, 50, 10, 5, and 1 cell. The 100 grids case gives a cell size (Δx) of 0.5 cm, and 50 cells have 1 cm length, and so on. Discretization details are summarized in Table A-1. The single-cell model is equivalent to a numerical dual-medium model of matrix-fracture transfer. Consider a regular 1-D uniform Cartesian grid ($x_{i+1} - x_i = \Delta x$ for all $i = 1 \dots n_x - 1$ and $\Delta y = \Delta z = 1$) like the one in Figure A-3.

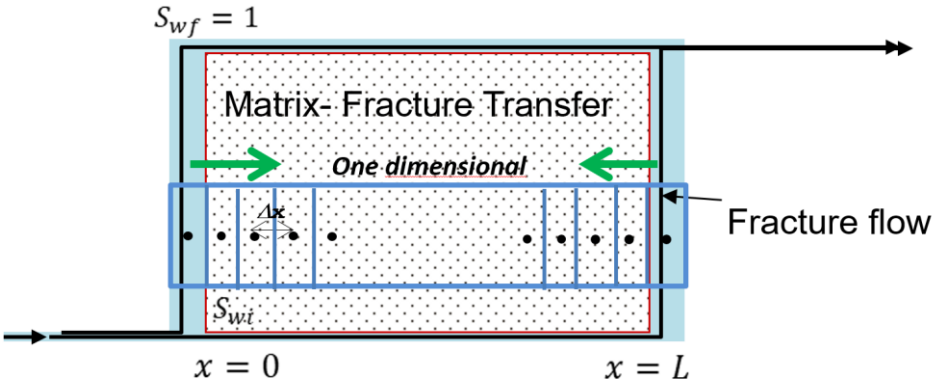


Figure A-3 Discretization schematic of the single medium block in the x-direction to simulate one-dimensional transfer from fracture to finely gridded matrix block.

Also, the time steps (Δt) in the finest case (100 grids) are chosen 0.1 of the main cases to investigate the time step effect. We should add the main cases simulation time is quite satisfying and is less than 1 minute for the base model.

The average concentration of chemical diffused from the fracture into the matrix block is compared Figure A 4. This plot illustrates that the fine grid solutions (100 and 50 cells) do not present noticeable difference on the results. Consequently, our initial 50 cells with a specified time step assumption are satisfying. The model with one grid cell has a large

difference with other cases and, the matrix concentration is estimated with the only point at the center of the block. Generally, a coarser grid block would underestimate the physical diffusion from the fracture to the matrix. The 100, 50 and 10 grid cells model match the exact analytical solution, especially after very early time of infinite acting behavior.

Table A-1 Numerical Simulation mesh grids for convergence study

No. of Cells	Δx (cm)	Δt (day)	$\Delta t/\Delta x^2$ (day/cm^2)	Simulation Time (min)
100	0.5	1e-4	4e-4	<2
50	1	1e-3	1e-3	<1
10	5	1e-3	4e-5	<1
5	1	1e-3	1e-5	<1
1	50	1e-3	4e-8	<1

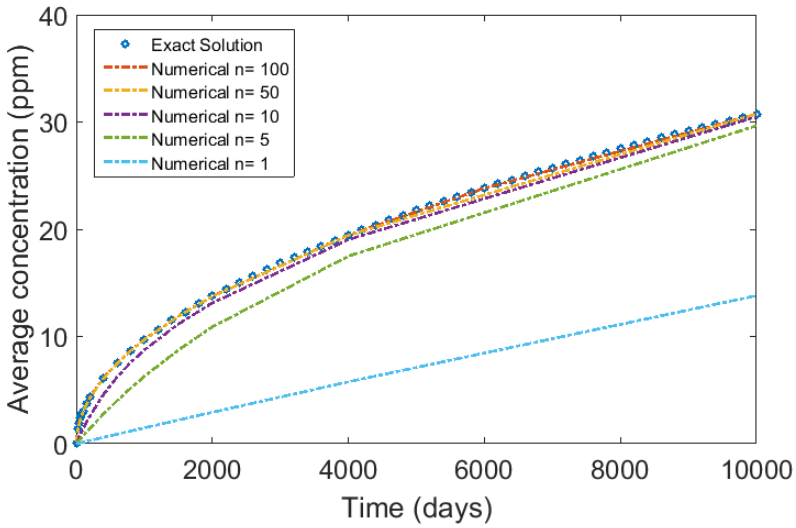


Figure A-4 Discretization effect (n =number of grid cells in one-dimensional gridding) on linear diffusion transfer to the Matrix (dashed lines) versus exact solution (circle dots). The convergence study shows the accuracy of our initial fine-grid model with $n = 50$.

The difference between one grid ($n = 1$) and the discretized numerical calculation can be compared in Figure A-5 giving the concentration profile at different times. Much of the difference is at the beginning of the early time transfer.

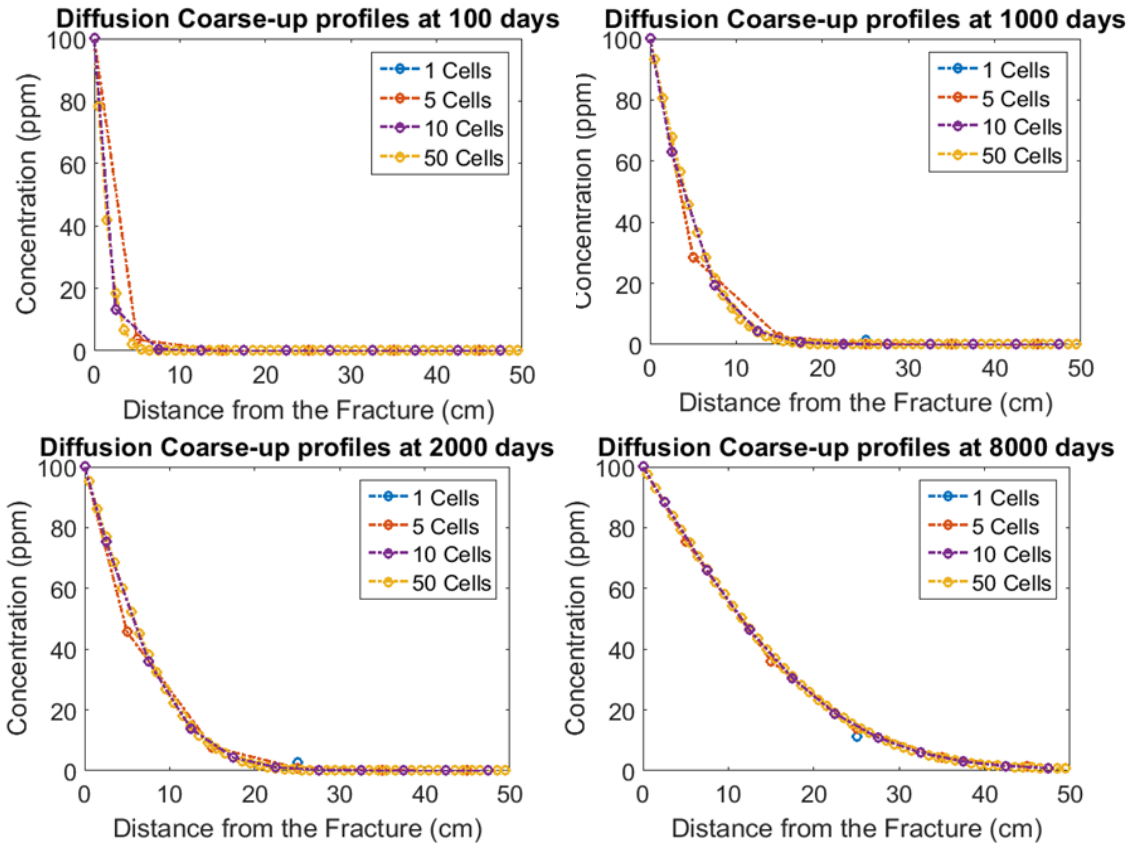


Figure A-5 Comparison of simulated concentration profiles for one-dimensional linear diffusion (with several mesh size) for $t = 100, 1000, 2000, 8000$ days. One cell grid case model has only one concentration calculation point similar to dual-medium approach.

Figure A-6 presents the error in comparison with the exact solution for different grid sizes. M is the total mass of surfactant that has diffused to matrix block ($\int_{-\infty}^{+\infty} C\, dx = M$ from Eq. 1-2), with M_{exact} the value of M calculated from the analytical solution and $M_{numerical}$ the value obtained from numerical models. This figure shows that the numerical model does not match the exact analytical solution at early times for these discretization grid sizes, and that the error decreases as time elapses.

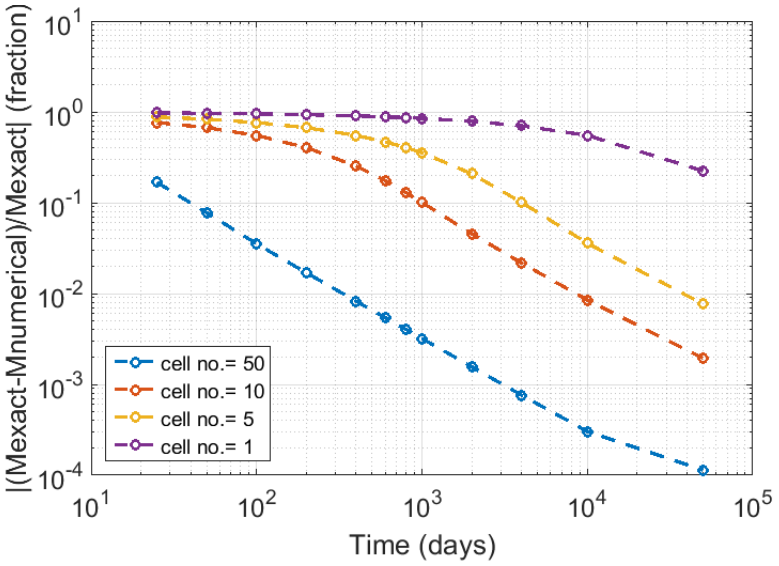


Figure A-6 Coarsening up discretization error plot of simulations (with $n = 1, 5, 10$ and 50 cells) in comparison with exact (analytical) solution for linear diffusion transfer in single phase condition. After very early time simulation, the fine-grid case gives an accurate accumulated transfer in comparison with the exact solution.

Annex B. Preliminary numerical verification of dual-medium model

The dual-medium (so-called dual porosity) and sub-gridding models to the matrix-fracture transfer are solved with a numerical simulator that considers different flow mechanisms with different methodologies.

Dual-medium fluid flow

(Lemonnier & Bourbiaux, 2010a, 2010b) analyze the recovery mechanisms in fractured reservoirs, then presents the method for modeling fractured flow in industrial simulators. This review has presented the flow equations for matrix and fractures medium separately. A material balance equation is written in each medium for each species *k*, which may be present in different phases φ. Equations below are expressed for a unit volume of the reservoir.

An elementary volume of reservoir is composed of porous rock and its fluid content. Because of the presence of fractures, fluid content and fluid flow are modeled by resorting to two fictitious porous media that are superimposed: the matrix medium and the fracture medium. This can be shown by superimposing two block centers of Figure 2-8. To take into account heterogeneities, the matrix medium and fracture medium have their own parameters (such as porosity, permeability) and their dynamic evolution (including transfers between them) is simulated by solving the unknowns (fluid saturation and pressure, mass fraction of species, …) attached to each separate medium.

For matrix medium denoted superscript (*m*), material balance includes transport term from cell to cell or does not whether a dual-porosity single-permeability model or a dual-porosity dual-permeability is considered. Our study considers a dual-porosity single-permeability model. For such a model, based on Eq. 1-5, the mass conservation of the species *k* in the matrix medium denoted (*m*) involves no transport term from block to block, hence simply reads:

$$\frac{\partial}{\partial t}\left[\phi^m \sum_{\varphi}(\rho_\varphi^m C_{\varphi k}^m S_\varphi^m)\right] + \sum_{\varphi}(\rho_\varphi^m C_{\varphi k}^m Q_\varphi^m) + F_{\varphi k}^{mf} = 0, \qquad \text{Eq. B-1}$$

where again ϕ is the porosity, ρ is the density, C is the mass fraction, S is the saturation and Q is the volumetric injection/production rate per unit bulk volume of reservoir. The rate is positive in production and negative in injection. $F_{\varphi k}^{mf}$ is the matrix-fracture mass flow rate as explained in Eq. B-4.

The mass conservation of the species k in the fracture medium denoted (f) reads:

$$\frac{\partial}{\partial t}\left[\phi^f \sum_{\varphi}(\rho_\varphi^f C_{\varphi k}^f S_\varphi^f)\right] + div\left[\sum_{\varphi}(\rho_\varphi^f C_{\varphi k}^f \boldsymbol{u}_\varphi^f) + \boldsymbol{J}_{\varphi k}^f\right] + \sum_{\varphi}(\rho_\varphi^f C_{\varphi k}^f Q_\varphi^f) - F_{\varphi k}^{mf} = 0, \quad \text{Eq. B-2}$$

where in this case $\boldsymbol{u}_\varphi^f$ denotes the velocity of the phase φ in the fracture and is given by the Darcy's law Eq. 1-1. $\boldsymbol{J}_{\varphi k}^f$ represents the diffusion-dispersion flux of the component k in a phase p, and is expressed as:

$$\boldsymbol{J}_{k\varphi}^f = -\rho_\varphi^f\left(\phi^f S_\varphi^f \boldsymbol{D}_{\varphi k} + \beta^f \left\|\boldsymbol{u}_\varphi^f\right\|\right)\boldsymbol{\nabla} C_{\varphi k}^f, \quad \text{Eq. B-3}$$

with $\boldsymbol{D}_{\varphi k}$ the diffusion tensor and β the dispersivity of the medium. Diffusion is generally negligible in comparison with other transfer mechanisms in the fractures. Reversely, flow-induced dispersion is prevailing in the fracture medium, which could be neglected in the presence of other transfers. Scaling of the dispersion coefficient is a delicate job because the dispersion flux depends on both the relative permeability function and dispersion coefficient.

Matrix-fracture dual-medium simulator

The main job with the formulations above is to specify the matrix-fracture transfer ($F_{\varphi k}^{mf}$) of species (k) in each phase (φ). In the context of numerical simulators, the fluxes between the matrix and the fracture medium result from a homogenization process, which relies on the discrete representation of the reservoir. Figure B-1 shows a schematic representation of matrix-fracture connection in a dual-porosity model. A simulation cell stands for the two media represented by two superposed nodes, a fracture node standing for the fracture network at cell scale, and a matrix node standing for the matrix blocks contained in that cell. All matrix blocks of a given cell are modeled as identical rectangle cuboids of given dimensions. The fluxes

between the fracture cell and its associated matrix cell are obtained by multiplying the above values (computed for one block) by the number of blocks $N = (DX.DY.DZ)/(L_x.L_y.L_z)$ where DX, DY, DZ are the simulation cell dimensions.

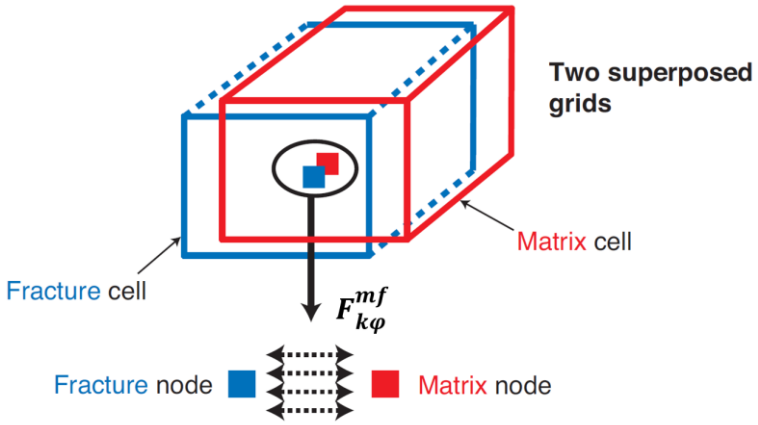


Figure B-1 Schematic for dual-medium matrix-fracture connection with two superimposed nodes (Lemonnier & Bourbiaux, 2010a).

(Lemonnier & Bourbiaux, 2010b) presents a detailed formulation for matrix-fracture transfer simulation, that is implemented PumaFlow software. The calibration and history matching of fractured reservoir simulation models are also reviewed in their paper. We focus on the detailed expression of exchange flux for the general case of compositional multiphase transfer.

For that cell, all matrix-fracture transfer of species k in phase φ per matrix block ($F_{\varphi k}^{mf}$) is expressed as the sum of fluxes across each lateral face (s) of a matrix block per unit volume of matrix, this leads to:

$$F_{\varphi k}^{mf} = \frac{1}{L_x.L_y.L_z}\sum_{s=1}^{6} f_{s\varphi k}. \qquad \text{Eq. B-4}$$

The flux across each block face, $f_{s\varphi k}$, is formulated using a Darcy-type equation. Total transfer between two nodes is the summation of each matrix block face per unit of volume. Separate calculation of exchange flux across each face helps to modify or annihilate selectively the contribution of lateral and top and bottom faces (Note that block orientation is assumed to coincide with model grid orientation). Therefore, no separate shape factor parameter is required using this formulation since it is implicitly considered in the discrete expression of transfers for the matrix block dimensions under consideration.

Mass flux unit is used. So $f_{s\varphi k}$ is the mass transfer of component *k* in the phase φ and across a matrix block face *s*. It is expressed as:

$$f_{sk\varphi} = (f_t)_{s\varphi k} + (f_d)_{s\varphi k}, \qquad \text{Eq. B-5}$$

where f_t is the transport flux term due to convection, and f_d is the diffusion-dispersion flux term.

They recalled that the pseudo-steady stat was initially designed to simulate single phase matrix-fracture transfer due to the average pressure difference between the two media. For multiphase transfers, a matrix-fracture Phase Potential difference must be considered. This potential is linked with the various forces in presence. Their study indicated that no rigorous formulation of multiphase flow transfers was available, especially when at least two mechanisms, such as capillarity and gravity, control the transfer. To deal with such limitations, their selected approach consists in splitting transfers into the contributions of each physical mechanism of transfer, and assigning them scaling factors.

The equations used to simulate matrix-fracture transfers in the dual-porosity option of our simulator PumaFlow are extensively described hereafter because the results of our up-scaling study of molecular diffusion of chemical species in fractured reservoirs (chapter 2) is tested using that framework.

The convection flux across the face *s* with PSS assumption is formulated from a Darcy-type equation written at the entire matrix block scale as (Sabathier et al., 1998);(Lemonnier & Bourbiaux, 2010a):

$$(f_t)_{sk\varphi} = -\left(C_{\varphi k}\rho_\varphi\right)^{(m,f)} \frac{A_s}{l_s/2} \lambda_{s\varphi}^{(m,f)} \left(\Phi_{s\varphi}^f - \Phi_{c\varphi}^m\right), \qquad \text{Eq. B-6}$$

where, $\Phi_{c\varphi}^m$ is the **potential of phase φ** taken in the matrix medium at the center *c* of the matrix block (assumed to coincide with center of the cell). $\Phi_{s\varphi}^f$ is the potential of phase φ taken in the fractures at the middle of the face *s* limiting the block, with $s = x^-, x^+, y^-, y^+, z^-, z^+$.

A_s and l_s=L_x, L_y or L_z, are respectively the cross-section area and the block length in each direction perpendicular to the face. That flux involves a specific phase mobility, $\lambda_{s\varphi}$, that is defined per face *s* (*i.e.* per direction of exchange) as:

$$\lambda_{s\varphi} = k_s^m \left(\frac{k_{r\varphi}}{\mu_\varphi}\right)_s^{(m,f)}. \qquad \text{Eq. B-7}$$

$\lambda_{s\varphi}$ differs also whether the exchange flux is from fracture to matrix or from matrix to fracture because fractures are playing the role of boundary conditions applied to the matrix block whereas transfer takes place within matrix medium from block boundary to block center. As the matrix-fracture flow takes place in matrix medium, the absolute permeability used for the calculation of this flow rate is always the matrix permeability k^m. The viscosity is calculated based on up-stream medium properties however, the relative permeability depends on saturation and matrix to fracture or fracture to matrix flow. If the matrix is upstream, the relative permeability of the transfer corresponds to the saturation of the matrix media. When the flow is entering the matrix from the fractures (fracture is upstream media), the relative permeability depends on the saturation of phase φ in the fracture and maximum relative permeability of the phase *p* in the matrix medium.

In Eq. B-5, f_d is the diffusion-dispersion flux of the component *k* in the phase φ across the face *s* is based on Fick's law:

$$(f_d)_{skp} = -\left[D_{eff}{}_{\varphi k} + \beta\left|u_{\varphi s}^{mf}\right|\right]\frac{A_s}{l_s/2}\rho_\varphi^{(m,f)}\left(C_{\varphi k}^f - C_{\varphi k}^m\right)\left(S_\varphi^f\right), \qquad \text{Eq. B-8}$$

where saturation S_φ^f represents the reduction of flux when the carrying phase *p* in fracture medium, β is the dispersivity coefficient of the flux. $D_{eff}{}_{\varphi k}$ is the **effective diffusion coefficient** of component *k* in phase φ partially saturating matrix block pores and in dual-medium model is expressed as:

$$D_{eff}{}_{\varphi k} = \Phi^m S_\varphi^m \frac{D_{\varphi k}}{\tau_s^m}, \qquad \text{Eq. B-9}$$

where, $D_{\varphi k}$ is the molecular diffusion coefficient of component k in the phase φ. τ_s is the tortuosity of the porous medium. Application of the matrix-fracture transfer model is given in the next chapter for a simple transfer mechanism by molecular diffusion.

For the single matrix block under consideration, the dual-porosity model is a single-cell model with cell dimensions (ΔX, ΔY, and ΔZ) equal to matrix block dimensions (L_X, L_Y, L_Z), hence the transfer flux at the scale of dual-medium model cell is equal to the transfer flux in a single matrix block (note that in reservoir models, the transfer flux at cell scale is computed by multiplying the flux per unit volume of matrix by the cell volume ($\Delta X.\Delta Y.\Delta Z$), assuming an array of identical blocks in a given cell).

Hereafter, we firstly present a preliminary check of dual-porosity model algorithms regarding the computation of matrix-fracture transfer, from a comparison with two numerically-equivalent single-porosity models. Actually, the dual-porosity model of a matrix block limited by two fractures at opposite ends of the block is equivalent to a coarse-grid single-porosity model with one cell representing the matrix block and two cells representing the two opposite fractures as shown in Figure B-2b). For reason of symmetry, it is also equivalent to a single-porosity model with one cell representing half of the matrix block and one cell representing fracture at the open end of the half block (Figure B-2.a). These two equivalent grid of single medium model, referred to as Full Block model and Half Block model, are schematized in Figure B-2, along with the single dual-medium cell of the dual-porosity model.

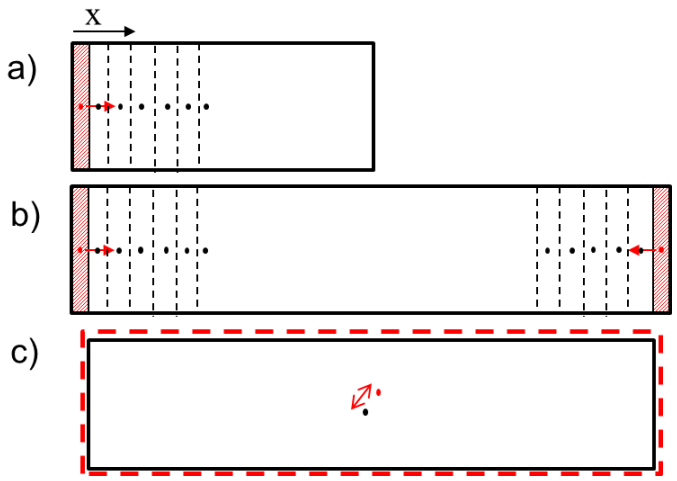


Figure B-2 Schematics of matrix-fracture numerical calculation models: a) single-medium half-block, b) single-medium full-block c) equivalent dual-medium model. Each point shows a calculation node, the dual-medium consists of two superimposed calculation points.

For the sake of clarity, only the full block model was used to validate the dual-porosity model algorithms recalled hereafter for matrix-fracture transfer driven by molecular diffusion alone.

The petro-physical properties of the dual-porosity model are the same as those of the corresponding single-porosity models studied in section 2.3. The same initial boundary value problem with a constant concentration of surfactant in the fracture was assumed.

Based on Eq. B-4 and Eq. B-8, the mass flux of component *k* exchanged by molecular diffusion in phase φ between a matrix block and the surrounding fractures is modeled by the following equation in the dual-medium model:

$$\sum f_{\varphi k}^{mf} = \sum_{s=1}^{6} \left[\phi^m S_\varphi^m \frac{D_{\varphi k}}{\tau_s^m}\right] \frac{A_s}{l_s/2} \rho_\varphi^{(m,f)} \left(C_{\varphi k}^f - C_{\varphi k}^m\right). \qquad \text{Eq. B-10}$$

This flux can also be expressed per unit volume of matrix medium as:

$$\begin{aligned} F_{k\varphi}^{mf} &= \frac{1}{L_x L_y L_z} \sum_{s=1}^{6} \left[\phi^m S_\varphi^m \frac{D_{\varphi k}}{\tau_s^m}\right] \frac{A_s}{l_s/2} \rho_\varphi^{(m,f)} \left(C_{\varphi k}^f - C_{\varphi k}^m\right) \\ &= 4\left(\frac{1}{L_x^2.\tau_x} + \frac{1}{L_y^2.\tau_y} + \frac{1}{L_z^2.\tau_z}\right) \phi^m S_\varphi^m D_{\varphi k} \rho_\varphi^{(m,f)} \left(C_{\varphi k}^f - C_{\varphi k}^m\right) \end{aligned} \qquad \text{Eq. B-11}$$

In this 1D transfer numerical model, diffusion in Y and Z directions are annihilated by choosing high values of tortuosity in those directions ($\tau_x = 2$, $\tau_y = 10^5$, $\tau_z = 10^5$).

Annex C. Numerical scheme of non-linear diffusion

In this annex, we detail the numerical scheme used to solve the singular elliptic partial differential Eq. 3-13 in the matrix block domain Ω. We consider neither the Boltzmann variable form Eq. 3-27 for short times, nor the asymptotic form Eq. 3-44 for long times, but the generic PDE that drives the solution $S(x,t)$ for all x and t. The singular character of this equation comes from the diffusion coefficient D given by Eq. 3-14 which vanishes and is not differentiable with respect to S, for $S = \{0,1\}$, except for particular values of the exponents r, p and q. Because D cancels at the boundary $\partial\Omega$ of the porous medium, one must have $(\nabla S)_{\partial\Omega} = -\infty$ in order to get a non-zero fracture-to-matrix flux $(D(S)\nabla S)_{\partial\Omega}$, as can be seen in Figure 3-12. To prevent numerical instabilities or large rounding errors, we set-up a conservative scheme which does not require to compute the product $D(S)\nabla S$, and is based on the following reformulation as a conservation law:

$$\frac{\partial S}{\partial t} = \nabla^2 G(S) \quad where \quad G(S) = \int_0^S D(s)\, ds, \qquad \text{Eq. C-1}$$

with S the normalized mobile aqueous phase saturation Eq. 3-2. The physical domain considered is Ω with boundary conditions $S(\mathbf{x},t) = 1$ on the boundary $\partial\Omega$ for all $t \geq 0$.

To start with, the function G defined in Eq. C-1 does not admit a simple expression that can be easily handled, except in the limiting cases $M \ll 1$ and $M \gg 1$ (G is then a power-law or an incomplete beta function, respectively) where M is the mobility ratio defined in Eq. 3-17. To derive a conservative numerical scheme, we resort to a discrete integration of the diffusion function D denoted G^h. To do so, we discretize the normalized saturation interval $[0,1]$ with the sequence $(\tilde{S}_k)_{k\in\{0,\dots,N_S\}} = k\Delta\tilde{S}$ composed of $N_S + 1$ points and where $\Delta\tilde{S} = 1/N_S$. For convenience, let us introduce the operator I_G^h which defines the discrete integral of G over two increasing saturation values S_α and S_β. Using the third order Simpson's method, I_G^h writes:

$$I_G^h(S_\alpha, S_\beta) = \frac{S_\beta - S_\alpha}{6}\left[D(S_\alpha) + 4D\left(\frac{S_\alpha + S_\beta}{2}\right) + D(S_\beta)\right]. \qquad \text{Eq. C-2}$$

For any saturation value S such that $S \in [\tilde{S}_k, \tilde{S}_{k+1}]$, we approximate the function $G(S)$ with $G^h(S) = I_G^h(\tilde{S}_k, S) + \sum_{l=1}^{k} I_G^h(\tilde{S}_{l-1}, \tilde{S}_l)$.

Regarding the domain Ω discretization, let $\mathcal{M}_h$ be an admissible finite volume mesh of the domain Ω given by a family of control volumes or cells noted K: for any K of $\mathcal{M}_h$, $|K|$ is its measure, $KL = \partial K \cap \partial L$ is the common interface between K and a neighbouring cell L. The set of neighbors of cell K is denoted $\mathcal{N}(K)$, that is $\mathcal{N}(K) = \{L \in \mathcal{M}_h; \partial K \cap \partial L \neq \emptyset\}$. Time is discretized with the non-decreasing sequence $\{t^n\}$ such that $t^0 = 0$ and $\Delta t = t^{n+1} - t^n$. Let also S_i^n be the approximation of the saturation on the interval $C_i \times [t^n, t^n + \Delta t)$. Finally, it is useful to introduce the vector $\mathbf{S}^n$ such that $(\mathbf{S}^n)_i = S_i^n$ in order to formulate the scheme vectorially.

Partial differential Eq. C-1 is recast in a discrete manner with the following finite-volume implicit scheme. Accounting for the boundary condition of an imposed saturation, i.e. $S(x = 0, t) = 1$, $\forall x \in \partial\Omega$, $\forall t \geq 0$, the numerical scheme can be written by introducing the function $\mathbf{Z}^n$ defined for all $K \in \mathcal{M}_h$ as:

$$[\boldsymbol{Z}^n(S)]_K = S_K^n - S_K^{n-1} - \sum_{L \in \mathcal{N}(K)} \lambda_{KL}(G_K^n - G_L^n) - \lambda_{K,\partial\Omega}\big(G_K^n - G(1)\big), \qquad \text{Eq. C-3}$$

with $G_K^n = G(S_K^n)$, $\lambda_{KL} = \Delta t|KL|/(|K|d_{KL})$ where $|KL|$ is the face measure and d_{KL} the distance between the center of cells K and L. The term $\lambda_{K,\partial\Omega}(G_K^n - G(1))$ stands for the boundary condition contributions, non null when the cell K is a boundary cell. As we use polyhedral mesh cells, it is the sum of several contributions if cell K has several boundary faces. For each boundary face $(\partial K)_j$, that contribution is $\Delta t|(\partial K)_j|/[|K|d_{K,(\partial K)_j}]$ where $|(\partial K)_j|$ is the measure of the face and $d_{K,(\partial K)_j}$ the distance between the cell center and the face.

The updated numerical solution $\mathbf{S}^n$ of this numerical scheme is the zero of the function $\mathbf{Z}^n$. As this function is non-linear because $G(S)$ non-linearly depends on saturation, a Newton-Raphson algorithm is required. Specifically, for each time step we construct a sequence $\mathbf{S}^{n,k}$ such that $\mathbf{Z}^{n,k} = \mathbf{Z}^n(\mathbf{S}^{n,k}) \xrightarrow{k\to\infty} 0$ and recursively defined by $\mathbf{S}^{n,k+1} = \mathbf{S}^{n,k} + \delta\mathbf{S}^{n,k}$ where $\delta\mathbf{S}^{n,k}$ denotes the increment vector given by:

$$\delta\boldsymbol{S}^{n,k} = -[\nabla_S \boldsymbol{Z}^{n,k}]^{-1}\boldsymbol{Z}^{n,k}, \qquad \text{Eq. C-4}$$

where the matrix $[\nabla_S \mathbf{Z}^{n,k}]^{-1}$ is the inverse of the Jacobian matrix $\nabla_{\boldsymbol{S}}\mathbf{Z}^{n,k} = \nabla_{\boldsymbol{S}}\mathbf{Z}^n(\mathbf{S}^{n,k})$. The increment vector $\delta\mathbf{S}^{n,k}$ is thus determined by solving a linear system. The Jacobian matrix is sparse and its non-null terms are given by, for all $K \in \mathcal{M}_h$:

$$\begin{aligned}\left(\nabla_S \mathbf{Z}^{n,k}\right)_{K,K} &= 1 - \left(\lambda_{K,\partial\Omega} + \sum_{L\in\mathcal{N}(K)} \lambda_{KL}\right) D_K^{n,k},\\ \left(\nabla_S \mathbf{Z}^{n,k}\right)_{K,L} &= \lambda_{KL} D_L^{n,k}.\end{aligned} \qquad \text{Eq. C-5}$$

In addition, as the function G is approximated numerically, we used the function G^h instead of G in Eq. C-3 to compute the Newton residue $\mathbf{Z}^{n,k}$. To end with, the Newton algorithm is performed until the L^2 norms of the residue $||\mathbf{Z}^{n,k}||_2$ and of the increment $||\delta\mathbf{S}^{n,k}||_2$ are sufficiently small.

Cylindrical geometry

For a cylindrical domain $\Omega = [0,R]\times[0,2\pi]\times[0,H]$ invariant by rotation and translation along the z-axis, the solution depends only on r (the distance to the axis) $\in [0,R]$. We therefore consider a uniform mesh composed of $N+1$ embedded cylinder of first cell $K_0 = [0,\Delta r/2]\times[0,2\pi]\times[0,H]$ and the following embedded $K_i = [(i-1/2)\Delta r,(i+1/2)\Delta r]\times[0,2\pi]\times[0,H]$ for $1\le i\le N_K$, where $\Delta r = R/(N_K+1/2)$. After some straightforward calculations, the scheme writes in the form Eq. C-3 with

$$\begin{aligned}\lambda_{K_0K_1} &= \frac{4\Delta t}{(\Delta r)^2},\\ \lambda_{K_iK_{i+1}} &= (1+\frac{1}{2i})\frac{\Delta t}{(\Delta r)^2} \quad for \quad 1\le i\le N_K,\\ \lambda_{K_N,\partial\Omega} &= \frac{\Delta t}{[1-(1-\frac{\Delta r}{R})^2]R\Delta r}.\end{aligned} \qquad \text{Eq. C-6}$$

Spherical geometry

For a spherical domain $\Omega = [0,R]^3$ invariant by rotation, we consider a uniform mesh composed of $N+1$ embedded sphere of first cell $K_0 = [0,\Delta r/2]^3$ and the following embedded $K_i = [(i-1/2)\Delta r,(i+1/2)\Delta r]^3$ for $1\le i\le N_K$, with $\Delta r = R/(N_K+1/2)$. In this case, the coefficients of the numerical scheme Eq. C-3 are:

$$\lambda_{K_0K_1} = \frac{6\Delta t}{(\Delta r)^2},$$
$$\lambda_{K_iK_{i+1}} = \frac{(i+\frac{1}{2})^2}{(i+\frac{1}{2})^3-(i-\frac{1}{2})^3}\frac{3\Delta t}{(\Delta r)^2} \quad for \quad 1 \le i \le N_K, \qquad \text{Eq. C-7}$$
$$\lambda_{K_N,\partial\Omega} = \frac{3\Delta t}{[1-(1-\frac{\Delta r}{R})^3]R\Delta r}.$$

Scilab code

Here, an example of our codes to simulate the counter-current capillary imbibition in a simple 2D rectangle is presented:

```
// resolve counter current flow
printf("------------------------------------------------------------------------\n");
printf(" \n");
printf(" \n");
printf("---------------------------------\n");
printf("---resolve cunter current flow---\n");
printf("---------------------------------\n");
printf(" \n");
printf(" \n");

//fileName  =;
fd0=mopen('numerics.log',"w");

mfprintf(fd0,"------------------------------------------------------------------------\n");
mfprintf(fd0," \n");
mfprintf(fd0," \n");
mfprintf(fd0,"---------------------------------\n");
mfprintf(fd0,"---resolve cunter current flow---\n");
mfprintf(fd0,"---------------------------------\n");
mfprintf(fd0," \n");
mfprintf(fd0," \n");

// units
darcy = 9.869233E-13;
day = 86400. ;

//////////////////////////////////////////
// petro values
phi = 0.25 ; // rock porosity [adim]
k = 10e-3*darcy; // absolute permeability [darcy]
swi = 0; // water irreductible saturation [adim]
sor = 0; // oil residual saturation [adim]
krwmax = 0.6; //0.6; // water maximal rel perm [adim]
kromax = 1.; //0.9; // oil maximal rel perm [adim]
nw = 3.; // water exponent [adim]
```

```
no = 2.; // oil exponent [adim]
pe = 5.e+5; // entry capillary pressure [Pa]
m = 2 // capillary pressure exponent [adim];

//////////////////////////////////////////
// fluid pvt values
muw = 4.e-4; // water viscosity [Pa/s]
muo = 4.e-3; // oil viscosity [Pa/s]

Dref = k*krwmax*pe/(m*phi*muw*(1.-sor-swi));
printf("Dref=%e \n", Dref);

// domain values
lx = 1.; // domain lengh [m]
ly = 0.1;

// numerical paramters
nx = 201 ; // number of cells
ny = 41 ;
nx_middle = int( (nx+1) / 2 );
ny_middle = int( (ny+1) / 2 );
printf("nx_middle %i \n",nx_middle);
printf("ny_middle %i \n",ny_middle);
ncell = nx*ny ;
// dx and dy now for finite difference scheme
dx = lx / ( nx + 1 ) ;
dy = ly / ( ny + 1 ) ;
dt_ini = 1.e-5*day; // time step [s]
dt_min = 1.e-8*day; // minimum time step [s]
dt_max = 10.*day; // maximum time step [s]
epsilon_newton = 1.e-8; // maximum value for Newton residu
epsilon_ds = 1.e-8; // maximum value for dsnk
itn_max = 20 ; // maximum number of newton iteration
itn_target = 5 ; // target number for Newton iteration number (adapt time step)
r_dt_m = 0.7 // factor for time step reduction if nitn > itn_target
r_dt_p = 1.2 // factor for time step increase if nitn < itn_target
r_dt_cut = 0.5 // factor for time stem reduction if s<0. or s>1

export_times = [0.0001 0.0002 0.0005 0.001 0.002 0.005 0.01 0.02 0.05 0.1 0.2 0.5 1 2 5 10]*day;

n_export = 15; //size(export_times);
final_time = 5;

// prints
mfprintf(fd0,"lx = %e \n", lx);
mfprintf(fd0,"nx=%i \n", nx);
mfprintf(fd0,"dx=%e \n", dx);

//////////////////////////////////////////
// saturation normalization
dsdsw=1./(1.-sor-swi);
```

```
mfprintf(fd0,'dsdsw= %e \n',dsdsw);
function s=sFromSw(sw)
   s=(sw-swi)*dsdsw;
endfunction

////////////////////////////////////////
// water relative permability

function krw=krwFromS(s)
   krw=krwmax*(s**nw);
endfunction

////////////////////////////////////////
// oil relative permability

function kro=kroFromS(s)
   kro=kromax*((1.-s)**no);
endfunction

////////////////////////////////
// water mobility

function mobw=mobwFromS(s)
   mobw=krwFromS(s)/muw;
endfunction

function mobo=moboFromS(s)
   mobo=kroFromS(s)/muo;
endfunction

////////////////////////////////////////
// capillary pressure

invm=1./m;
r=-1./m-1;
function pc=pcFromS(s)
   pc=pe/(s**(invm));
endfunction

function dpc=dpcFromS(sw)
   dpc=-invm*dsdsw*pe/(s**(invm+1.));
endfunction

////////////////////////////////////
// Fonction D(s)

function D=DFromS(s)
   if( s > 0. )
      mobw=mobwFromS(s);
      mobo=moboFromS(s);
      dpc=dpcFromS(s);
      D=-k*(mobw*mobo)*dpc/phi/(1-swi-sor)/(mobw+mobo);
```

```
   else
      D = 0.
   end
   //D = 1.e-5;
endfunction

function derD=derDFromS(s)
   if( s > 0. )
      f = s**(r+nw)*(1-s)**no;
      g = muw/krwmax*(1-s)**no+muo/kromax*(s)**nw;
      f_prime = (r+nw)*s**(r+nw-1)*(1-s)**no-no*(1-s)**(no-1)*s**(r+nw);
      g_prime = -muw/krwmax*no*(1-s)**(no-1)+muo/kromax*nw*s**(nw-1);
      derD = -k*pe/phi/m/(1-swi-sor)*(f*g_prime-f_prime*g)/g**2;
   else
      derD = 0.;
   end
endfunction

// Compute P(S) the ) Integral of D(S) numerically
// to formulate dx( D(S)dxS ) = dx ( dx( P(S) ) )
// and approximate analtical solution J = integral(D(s)/s *ds)
n_tab = 10000.;
ds_tab = 1./(n_tab-1.);
s_tab = zeros(n_tab,1);
P_tab = zeros(n_tab,1);
J_tab = zeros(n_tab,1);

P_tab(1) = 0. ;
J_tab(1) = 0. ;

for i_tab = 1 : n_tab
   s_tab(i_tab) = (i_tab-1.)*ds_tab;
end

P_tab(1) = 0. ;
for i_tab = 2 : n_tab
   sl = s_tab(i_tab-1);
   sr = s_tab(i_tab);
   sc = 0.5*( sl + sr );
   dl = DFromS(sl);
   dc = DFromS(sc);
   dr = DFromS(sr);

   // Simpson
   P_tab(i_tab) = P_tab(i_tab-1) + (sr-sl)*( dl + 4.*dc + dr)/6.
   dJ = DFromS(sc)/sc;

   J_tab(i_tab) = J_tab(i_tab-1) + dJ * ds_tab ;

end

function interP=interPFromS(s)
```

```
   // search s position in table

   if( s >= 1.)
      interP = P_tab(n_tab);
   elseif( s <= 0. )
      interP = 0.;
   else
      ind = int16(s/ds_tab) + 1 ;
      sl = s_tab(ind);


      // Simpson
      sr = s
      sc = 0.5*( sl + sr );
      dl = DFromS(sl);
      dc = DFromS(sc);
      dr = DFromS(sr);
      interP = P_tab(ind) + (sr-sl)*( dl + 4.*dc + dr)/6.
   end
end

////////////////////////////////////////

// definbe xx tab with x position
for i=1:nx
   xx(i) = i * dx;
end

for j=1:ny
   yy(j) = j * dy;
end

// saturation at time t=tn
sn = zeros(ncell,1);

nt = 100.*final_time/dt_min ;

// Time init
time = 0.;
dt = dt_ini;

i_export = 1;
itn_num = 0;
it_non_phys = 0;
it_max_new = 0;

A=sparse([ncell,ncell]);
B=zeros(ncell,1);

function iglob=ij2iglob(ix,iy)
   iglob = ix + ( iy - 1 ) * nx
endfunction
```

```
dx2 = dx * dx ;
dy2 = dy * dy ;

file_t=mopen("result_TimeVsAvSat.dat","w");

// Time Loop
for it = 1:nt
   mfprintf(fd0,' \n');

   dt_export = export_times(i_export)-time;
   //mfprintf(fd0,'dt_export=%e \n',dt_export/day);
   dt = min(dt,dt_max);
   dt = max(dt,dt_min);
   dt_save = dt;

   if( dt_export < dt)
      mfprintf(fd0,'--dt for file export \n');
      dt = dt_export;
   end

   lambda = 1./dt;
   //snk, Newton iterate
   snk = sn ;

   // Newton loop
   for itn = 1:10+itn_max

      // domain interior
      for iy=1:ny
         for ix=1:nx

            iw = ij2iglob(ix-1,iy);
            ie = ij2iglob(ix+1,iy)
            ic = ij2iglob(ix,iy)
            in = ij2iglob(ix,iy+1)
            is = ij2iglob(ix,iy-1)

            if(ix>1) then
               s_w = snk(iw);
            else
               s_w=1.;
            end

            if(ix<nx) then
               s_e = snk(ie);
            else
               s_e=1.;
            end

            s_c = snk(ic);
```

```
      if(iy<ny) then
         s_n = snk(in);
      else
         s_n=1.;
      end

      if(iy>1) then
         s_s = snk(is);
      else
         s_s=1.;
      end

      d_w = DFromS( s_w );
      d_e = DFromS( s_e );
      d_c = DFromS( s_c );
      d_n = DFromS( s_n );
      d_s = DFromS( s_s );

      if(ix>1) then
         A(ic,iw)= - d_w/dx2;
      end

      if(ix<nx) then
         A(ic,ie)= - d_e/dx2;
      end

      A(ic,ic)= lambda + 2.*d_c/dx2 + 2.*d_c/dy2;

      if(iy<ny) then
         A(ic,in)= - d_n/dy2;
      end

      if(iy>1) then
         A(ic,is)= - d_s/dy2;
      end

      p_w = interPFromS( s_w ) ;
      p_e = interPFromS( s_e ) ;
      p_c = interPFromS( s_c ) ;
      p_n = interPFromS( s_n ) ;
      p_s = interPFromS( s_s ) ;

      B(ic) = -lambda*( snk(ic) -sn(ic) ) + ( p_w - 2.*p_c + p_e )/dx2 + ( p_n - 2.*p_c + p_s )/dy2 ;

   end
end

// Newton residu
residu_rhs = 0.;
for ix=1:ncell
   residu_rhs = residu_rhs + B(ix)*B(ix);
end
```

```
   residu_rhs = sqrt(residu_rhs);

   //  linear system resolution
   dsnk = A\B;

   // residu ds
   residu_ds = 0.
   for ix=1:ncell
      residu_ds = residu_ds + dsnk(ix)*dsnk(ix);
   end
   residu_ds = sqrt(residu_ds);


   // update of Newton loop iterate
   snk = snk + dsnk ;

   mfprintf(fd0,'    itn = %i, r_rhs = %e r_ds = %e \n',itn,residu_rhs, residu_ds);

   // exit the Newton loop if the residu is small
   if( residu_rhs < epsilon_newton & residu_ds < epsilon_ds )
      //mfprintf(fd0,' n_itn = %i, r_rhs = %e r_ds = %e \n',itn,residu_rhs, residu_ds);
      break
   end

   if( itn > itn_max )
      //mfprintf(fd0,' bad ! n_itn = %i, r_rhs = %e r_ds = %e \n',itn,residu_rhs, residu_ds);
      break
   end
end

// check if the solution is physical
snk_min = 1.e+3;
snk_max = -1.e+3;
for ix=1:ncell
   snk_min=min(snk(ix),snk_min);
   snk_max=max(snk(ix),snk_max);
end

// time step management
if( snk_min < 0. | snk_max > 1.)
   if( dt <= dt_min )
      mfprintf(fd0,'non physical solution with dt_min stop \n');
      printf("dt  %e dtmin  %e",dt,dt_min)
      halt("error");
   end
   mfprintf(fd0,'non physical solution, restart with smaller time step \n');
   dt = dt * r_dt_cut;
   it_non_phys = it_non_phys + 1;

elseif( itn > itn_max )
   if( dt <= dt_min )
      mfprintf(fd0,'limit number of Newton iteration reached with dt_min stop \n');
```

```
      stop;
    end
    mfprintf(fd0,'limit number of Newton iteration reached, restart with smaller time step \n');
    dt = dt * r_dt_cut;
    it_max_new = it_max_new + 1;
  else
    // update of time loop iterate
    sn = snk
    time = time + dt ;
    itn_num = itn_num + itn;

    sum_sn = 0.
    for iyy=1:ny
      for ixx=1:nx
        sum_sn = sum_sn + sn(ij2iglob(ixx,iyy))*(dx*dy)/(lx*ly)
      end
    end
    mfprintf(file_t,"  %e  %e \n" , time, sum_sn)

    if( dt == dt_export)
      dt = dt_save;
      mfprintf(fd0,'it = %i t = %e   dt= %e \n',it,time/day,dt/day);
      mfprintf(fd0,'take dt_save\n');
    else
      if( itn > itn_target)
        mfprintf(fd0,'it = %i t = %e --dt= %e \n',it,time/day,dt/day);
        dt = dt*r_dt_m;
      elseif( itn < itn_target)
        mfprintf(fd0,'it = %i t = %e ++dt= %e \n',it,time/day,dt/day);
        dt = dt*r_dt_p;
      else
        mfprintf(fd0,'it = %i t = %e ==dt= %e \n',it,time/day,dt/day);
      end
    end

    // export the results in x and y directions
    if( export_times(i_export) == time)
      fileName1 = "resultSx_it_"+string(it)+"_t_"+string(time/day)+".dat"
      fileName2 = "resultSy_it_"+string(it)+"_t_"+string(time/day)+".dat"

      fd1=mopen(fileName1,"w");
      mfprintf(fd0,' export file '+ fileName1 );
      printf(' \n');
      printf('it = %i t = %e \n',it,time/day);
      printf(' export file '+ fileName1 );
      mfprintf(fd1,'%e   %e \n', 0., 1. );

      for ix=1:nx
        itab =  ij2iglob(ix,ny_middle);
        mfprintf(fd1,'%e   %e \n', xx(ix), sn(itab) );
      end
      mfprintf(fd1,'%e   %e \n', 1., 1. );
```

```
        mclose(fd1);

        fd2=mopen(fileName2,"w");
        mfprintf(fd0,' export file '+ fileName2 );
        printf(' export file '+ fileName2 );
        mfprintf(fd2,'%e   %e \n', 0., 1. );

        for iy=1:ny
           itab =  ij2iglob(nx_middle,iy);
           mfprintf(fd2,'%e   %e \n', yy(iy), sn(itab) );
        end
        mfprintf(fd2,'%e   %e \n', 0.1, 1. );
        mclose(fd2);

        i_export = i_export + 1;
      end

   end

   // if we reach the final export time, quit the time loop
   if(i_export > n_export)
      break;
   end

end

close(file_t)

mfprintf(fd0," \n");
mfprintf(fd0," \n");
mfprintf(fd0,"---------------------------------\n");
mfprintf(fd0,"----------end of program---------\n");
mfprintf(fd0,"---------------------------------\n");
mfprintf(fd0,"Total number of Newton iterations = %i \n",itn_num);
mfprintf(fd0,"Total number of non-physical iterations = %i \n",it_non_phys);
mfprintf(fd0,"Total number of non-converged iterations = %i \n",it_max_new);

mfprintf(fd0," \n");
mfprintf(fd0," \n");
mfprintf(fd0,"-------------------------------------------------------------------\n");
mclose(fd0);

printf(" \n");
printf(" \n");
printf("---------------------------------\n");
printf("----------end of program---------\n");
printf("---------------------------------\n");
printf("Total number of Newton iterations = %i \n",itn_num);
printf("Total number of non-physical iterations = %i \n",it_non_phys);
printf("Total number of non-converged iterations = %i \n",it_max_new);
```

Annex D. Fixed-point algorithm

In this annex the fixed-point algorithm represented in section 3.7.3 to solve the late time differential equation in a 2D rectangle is attached. The code is written for FreeFEM++.

```
// Late time solution delta.(h) = -h^{zeta}
// in a 2D rectangle (symmetrical)
real Lx = 1.;
real Ly = 0.1;
real epsilon = 1e-15;

mesh Mesh2D = square(101, 11, [Lx*x,Ly*y], flags=1);

// Finite Element Space
load "Element_P4";

fespace FES(Mesh2D, P4);
FES h=0., dh=0., v, hold ;

fespace Ph(Mesh2D, P1dc);
Ph D, dD , rhs, drhs ;

plot(Mesh2D, fill=true, ps="latetime_capillarydiffusion_rectangle.eps");
savemesh(Mesh2D,"rectangle.msh");

real hi = 1.e-10;

problem Laplace(h, v, solver=LU)
= int2d(Mesh2D)( dx(h) * dx(v) + dy(h) * dy(v) )
  - int2d(Mesh2D)( rhs * v )
  + on(1, h=0.)
  + on(2, h=0.) // The Dirichlet B.C.
  + on(3, h=0.)
  + on(4, h=0.) // The Dirichlet B.C.
  ;

rhs=1.;
Laplace;

cout << " very large value of alpha_1," << endl;
cout << " initial guess calculation of h: min " << h[].min << ", max = " << h[].max << endl;
cout << " " << endl;

h = max(h,hi) ;

plot(h, fill=true, grey=true, value=true);

real alpha1 = 2.;
real D1 = 2.4675e-6;
```

```
real zeta = 1./(alpha1+1.);
real lambda = pow(alpha1*D1/(alpha1+1), (alpha1+1)/alpha1);
dh = 0.;

// Fixed point or Newton-Raphson method
for (int i = 0; i < 50; i++){
  hold = h ;
  rhs = pow( h , zeta );
  drhs = zeta * pow( h, zeta - 1.) ;
  cout << " rhs[].max " << rhs[].max << " drhs[].max " << drhs[].max << endl ;

  // --- For fixed point
  Laplace;
  dh = abs(h - hold);
  cout << "       h  min " <<  h[].min << " , max = " <<  h[].max << endl;
  cout << "      dh[].linfty "  << dh[].linfty << endl;

  // --- End of loop
  h = max(h,hi) ; //still negative values in final h!

  plot(h, fill=true, grey=true, value=true);

  if( dh[].linfty < epsilon ){
                    cout << "*****converged with " << i+1. << " loops, for error_epsilon = " << epsilon <<
endl;
      break;
                    }

 }

plot(h, fill=true, grey=true, value=true);

load "iovtk"
int[int] Order = [1];
savevtk("h_function_plot.vtk", Mesh2D, h, dataname="h", order=Order);

//extract the f(x,y) in asymptotic late time solution
ofstream output("LateTimesSol_SpatialFunction_RecMesharea.dat");
output << h[] << endl;

//f(x,y=Ly/2) for 1D flow rectangle
ofstream output2("LateTimesSol_SpatialFunction_rectangle_x_line.dat");
                    for(real i = 1; i < 1001; i += 1){
                              //func f = pow(h(i*Lx/2./1000.,0.5*Ly)/lambda, zeta);
                              output2 << i*Lx/2./1000. << " " << h(i*Lx/2./1000.,0.5*Ly) << endl; // FreeFEM
interpolation for profile
                    }

ofstream output3("LateTimesSol_SpatialFunction_rectangle_y_line.dat");
                    for(real i = 1; i < 1001; i += 1){
                              //func f = pow(h(i*Lx/2./1000.,0.5*Ly)/lambda, zeta);
```

```
                output3 << i*Ly/2./1000. << " " << h(0.5*Lx,i*Ly/2./1000.) << endl; // FreeFEM
interpolation for profile
            }

real S = 0.;
```

List of figures

Figure 1-1 Illustration of an element of a fractured porous media including parallel fractures, open channels, vugs, and stylolite (Reiss, 1980). 10
Figure 1-2 A schematic of main matrix-fracture transfer mechanisms in a matrix block (dotted rectangle area) surrounded by fractures flowing with water (light blue). The arrows guide to understand the flow paths. 11
Figure 1-3 Schematics of the matrix-fracture transfer mechanisms in groups of diffusion like and directional driving (Bourbiaux et al., 2003). The blue and orange arrows show the fluid flux of aqueous and non-aqueous phases between the matrix block and the surrounding fracture network. Our study focuses on diffusive driving mechanisms. 13
Figure 1-4 Multi-scale feature of fluid flow modeling in porous medium, up-scaling from pore-scale (Microscopic scale) to reservoir-scale (Macroscopic scale). 15
Figure 1-5 Classical representation of a 3D fractured matrix block (left) with the equivalent dual-medium model (right) known as sugar cube model (Warren & Root, 1963). 21
Figure 1-6 scheme of MINC sub-gridding method to capture the transient transfer inside the matrix blocks (after Pruess & Narasimhan, 1985). 24
Figure 2-1 Pressure profile of one-dimensional pressure diffusion to the matrix block from both sides for different dimensionless time (t/τ) 34
Figure 2-2 Average matrix block pressure of the one-dimensional pressure diffusion versus dimensionless time (t/τ). 35
Figure 2-3 Comparison of the time-dependent part of shape factor (Eq. 2-13) with its late time approximation (Eq. 2-14) in linear and logarithmic y-axis. 36
Figure 2-4 Expansion of the series solution of $\sigma 1,2$ (numerator and denominator of Eq. 2-13) and convergence speed to exact solution. All expansions converges to the exact solution at late times ($t/\tau \gg 1$). 37
Figure 2-5 Comparison of the exact series expansion $\sigma 1$(numerator of time-dependent shape factor in Eq. 2-13) and its early time ($t/\tau \ll 1$) approximation Eq. 2-15. 38
Figure 2-6 Comparison of the exact average block pressure Eq. 2-10 (approximated by analytical series expansion with 100 terms) with its early time approximation ($t/\tau \ll 1$ giving Eq. 2-15) and late time approximation 38
Figure 2-7 Exact analytical ("Instantaneous") shape factor with early- and late-times approximations (from Eq. 2-19) in dimensionless time. Shape factor values are dimensionless based on the block length (l). 39
Figure 2-8 Formulation of shape factor transfer for a parallelepiped matrix block and surrounding fractures by assuming a transfer length from each face ($s = x^-, x^+, y^-, y^+, z^-, z^+$) to the block center ($c$). 40
Figure 2-9 Schematic of molecular diffusion in a matrix block surrounded by fracture. The solution is in one-dimension for analytical and numerical fine-grid calculation (discretized *1m* rectangle in *x*-direction) with a symmetry axis at the middle of the block. 46
Figure 2-10 Comparison between the numerical simulation (dashed line) and the exact solution (solid line) for a one-dimensional linear diffusion from fracture to matrix block with Dirichlet boundary condition. Corresponding time scale is characterized by τ. 46

Figure 2-11 Linear diffusion solution with analytical solution (solid line), numerical fine-grid (dashed line) and numerical dual-medium model (dotted line) in dimensionless time. The classical dual-medium model underestimates the matrix-fracture transfer. 47
Figure 2-12 Matrix-fracture diffusion flux calculation with fine-grid numerical model in (a) log-log and (b) semi-logarithmic scale in dimensionless time. Two distinguished flow behaviour can be observed in both plots. 49
Figure 2-13 Comparison of modified dual-medium model with a multiplier (late time asymptotic correction) with the exact solution (analytical solution or fine-grid simulation). A convergence toward the exact solution is observed, a better modification based on non-linear early time dependency is required. 50
Figure 2-14 Dual-medium shape factor correction versus average concentration of matrix block for a linear diffusion transfer with constant fracture boundary condition. The correction function is based on variable of interest (concentration) and is valid only for early times. 51
Figure 2-15 Matching the dual-medium model with the fine-grid model (or exact solution) using dynamic correction factors (Eq. 2-28) for early times ($t/\tau \ll 1$) and a asymptotic multiplier (2.5) for full period of the transfer. 52
Figure 3-1 A simple example for capillary pressure curve using Corey correlation (Eq. 3-3) with $Swi = 0.1$, $Sor = 0.1$, $Pe = 5$ bars, and $m = 2$. 61
Figure 3-2 Example of Relative Permeability curve with Swi $= 0.1$, Sor $= 0.1$, κw $= 0.6$, κo $= 1$, p $= 3$, q $= 2$. 62
Figure 3-3 Schematic of the simple matrix block surrounded by the fracture saturated by two immiscible phases. Pure spontaneous capillary imbibition in the *x*-direction is considered for matrix-fracture transfer. A symmetry at the middle of block when the flow happens at $x = 0$ and $x = L$ with a same boundary condition. 66
Figure 3-4 Several examples of $D(S)$ given by Eq. 3-14 with $k = 10$ md, $\phi = 0.25$, $Pe = 5$ bar, $Swi = Sorw = 0$, and different exponents and mobility ratios mentioned in the legend. The diffusivity is very low at very low and very high saturation and the relative permeability and capillary pressure exponent can control the diffusion transfer. 68
Figure 3-5 Several $D(S)$ given by Eq. 3-14 for $p = 3$, 5 and $M = 6$, 0.06 with $q = 2$, $m = 2$, $k = 10$ mD, $Pe = 5$ bar, $\phi = 0.25$, $Swi = Sorw = 0$. Asymptotic power laws for the extreme saturations given by Eq. 3-18 are reported as dashed lines. 69
Figure 3-6 Comparison between analytical solution of a capillary imbibition diffusion problem with constant equivalent diffusion coefficients (solid lines calculated from Eq. 2-10) and numerical solution of full non-linear diffusion problem (dashed line). 73
Figure 3-7 Comparison between numerical solution (dashed line) and a hybrid model including analytical solution with constant equivalent diffusion (solid line) for early times plus exponential fit (circle line) for late times. 77
Figure 3-8 Comparison analytical solution and two approximations of non-linear ODE (Eq. 3-29) with power law diffusion function 80
Figure 3-9 Comparison between analytical solution (solid line) of power-law diffusion (Eq. 3-29) and numerical solution (dotted line) of full non-linear diffusion (Eq. 3-13) at early times (semi-infinite flow behavior) with $p = 3$ ($\alpha 0 = 1.5$), $q = 2$, $M = 6$, $= 10$ mD, $Pe = 5$ bar, $\phi = 0.25$, $Swi = Sorw = 0$. 81

Figure 3-10 Evaluation of A values (the coefficient of higher order approximation of analytical solution of Eq. 3-39) based on Eq. 3-41 for power-law (dotted lines) and general forms (solid lines) of non-linear diffusion function for different values of $p = 3,5,7$ and with $q = 2$, $M = 6$, $= 10$ mD, $Pe = 5$ bar, $\phi = 0.25$, $Swi = Sorw = 0$. 83
Figure 3-11 Comparison between analytical solution of lowest order approximation and higher order approximations (solid lines) with different choices of coefficient A and numerical solution (dotted line) for non-linear diffusion Eq. 3-13 with $p = 3$ ($\alpha 0 = 1.5$), $q = 2$, $M = 6$, $= 10$ mD, $Pe = 5$ bar, $\phi = 0.25$, $Swi = Sorw = 0$. 84
Figure 3-12 Comparison of early-time analytical solution given in Eq. 3-43 (solid lines) with the simulated one (dotted lines) for $\alpha 0 = 1.5, 3.5$ ($p = 3, 5$) and $M = 6, 0.06$ with $q = 2$, $m = 2$, $k = 10$ mD, $Pe = 5$ bar, $\phi = 0.25$, $Swi = Sorw = 0$. 85
Figure 3-13 (a)-(b) Late-time analytical solution $y(x)$ given in Eq. 3-58 for several $\alpha 1$ values. (c)-(d) Comparison of the late-time analytical solution and rescaled (solid lines) given in Eq. 3-46 and Eq. 3-58 with the simulated one (symbols) for $\alpha 1 = 2$, $p = 3$, $M = 6$, $m = 2$, $k = 10$ mD, $Pe = 5$ bar, $\phi = 0.25$, $Swi = Sorw = 0$. Red crosses for the fixed-point solution (detailed in section 3.7.3) indicated in (d) correspond to a direct numerical solution of the asymptotic ansatz. 89
Figure 3-14 (a) Time evolution of the matrix-to-fracture flux for a few $\alpha 0$ and $\alpha 1$ exponents $\alpha 0 = 1.5, 3.5$ ($p = 3, 5$, $m = 2$) and $\alpha 1 = 2, 4$ with $M = 6$, $k = 10$ mD, $Pe = 5$ bar, $\phi = 0.25$ and $Swi = Sorw = 0$. Simulated early- and late-time slopes $-\{0.48,0.46,0.44\}$ and $-\{1.45,1.48,1.21\}$, respectively, are in excellent agreement with the early- and late-time predictions (thin solid lines) -12 and $-\alpha 1 + 1\alpha 1 = -32$ and -54 for $\alpha 1 = 2$ and 4, respectively. The time scale is normalized by the diffusion time $\tau 0 = L2/(4D0)$. (b) Time evolution of the matrix-to-fracture flux multiplied by its asymptotic time dependencies (Eq. 3-60) and divided by its asymptotic prefactors $A0$ and $A\infty$ (Eq. 3-61) and (Eq. 3-62) for the same $\alpha 0$ and $\alpha 1$ exponents. 93
Figure 3-15 Two-dimensional geometries studied: disk, square, rectangle and quadrangle (all surfaces are to scale except the rectangle, magnified three times). The characteristic lengths as well as the paths on which the saturation field $1 - S(\mathbf{x}, t)$ is projected in plots below are indicated in blue and red. 97
Figure 3-16 The solution map of Eq. 3-66 for the two-dimensional domains presented in Figure 3-15. The calculation is based on fixed-point algorithm conducted by FreeFEM software. The triangular mesh of the domains are coarser than the real meshes used for the results. 98
Figure 3-17 Disk — comparison of the fixed-point solution (solid lines, $1\,654$ elements) with the numerical solution (symbols, 500 nested rings). The time scale is normalized by the diffusion time with $Lc = 2R = 1$ m. 99
Figure 3-18 Square — comparison of the fixed-point solution (solid lines, $4\,050$ elements) with the numerical solution (symbols, $101 \times 101 = 10\,201$ cells). The time scale is normalized by the diffusion time with $Lc = L = 1$ m. 100
Figure 3-19 Rectangle — comparison of the fixed-point solution (solid lines, $2\,222$ elements) with the numerical solution (symbols, $201 \times 41 = 8\,241$ cells). The time scale is normalized by the diffusion timewith $Lc = Lx = 10\,Ly = 1$ m. 100

Figure 3-20 Quadrangle — comparison of the fixed-point solution (solid lines, 4 272 elements) with the numerical solution (symbols, $101 \times 101 = 10\,201$ cells). The time scale is normalized by the diffusion time with $Lc = Lx = Ly = 0.781$ m. 101
Figure 3-21 Time evolution of the simulated matrix-to-fracture flux for the considered two-dimensional geometries: disk, square, rectangle and quadrangle (see the text and Figs 2, 3, 4 and 5). Simulated early- and late-time slopes are in excellent agreement with the early- and late-time predictions (thin solid lines). The characteristic length Lc is set to 2R, L or Lx or Ly depending on whether the medium is a disk (of radius R), square (of side L), rectangle (of sides Lx and Ly) or quadrangle (of medians Lx and Ly). The tested flow configuration is such that $\alpha 1 = 2$, $p = 3$, $M = 6$, $m = 2$, $k = 10$ mD, $Pe = 5$ bar, $\phi = 0.25$ and $Swi = Sorw = 0$. 102
Figure 3-22 Time evolution of the simulated matrix-to-fracture flux for the square and rectangle (see Figure 3-15) with different diffusion coefficient configuration $\alpha 0 = 1.5, 3.5$ $\alpha 1 = 2,4$, $M = 6, 0.06$. The transition between early- and late-times tried to be scaled using three different dimensionless time. 104
Figure A-1 Example of discretization of a complex mesh in cartesian coordinate to show the capability of a numerical simulator (figure from the technical manual of PumaFlow) 116
Figure A-2 Example of control volume for a 2-D mesh (figure from the technical manual of PumaFlow) 117
Figure A-3 Discretization schematic of the single medium block in the x-direction to simulate one-dimensional transfer from fracture to finely gridded matrix block. 121
Figure A-4 Discretization effect ($n =$number of grid cells in one-dimensional gridding) on linear diffusion transfer to the Matrix (dashed lines) versus exact solution (circle dots). The convergence study shows the accuracy of our initial fine-grid model with $n = 50$. 122
Figure A-5 Comparison of simulated concentration profiles for one-dimensional linear diffusion (with several mesh size) for $t = 100, 1000, 2000, 8000$ days. One cell grid case model has only one concentration calculation point similar to dual-medium approach. 123
Figure A-6 Coarsening up discretization error plot of simulations (with $n = 1, 5, 10$ and 50 cells) in comparison with exact (analytical) solution for linear diffusion transfer in single phase condition. After very early time simulation, the fine-grid case gives an accurate accumulated transfer in comparison with the exact solution. 124
Figure B-1 Schematic for dual-medium matrix-fracture connection with two superimposed nodes (Lemonnier & Bourbiaux, 2010a)..... 127
Figure B-2 Schematics of matrix-fracture numerical calculation models: a) single-medium half-block, b) single-medium full-block c) equivalent dual-medium model. Each point shows a calculation node, the dual-medium consists of two superimposed calculation points. 130

List of tables

Table 2-1 Shape factor constant ($\sigma l2$, dimensionless shape factor) for 1D to 3D shapes based on different calculation approaches and different initial/boundary conditions. 43
Table 2-2 Example set of the properties of the simulation model 45
Table 3-1 Some of dimensionless time scaling for the capillary imbibition process 76
Table A-1 Numerical Simulation mesh grids for convergence study 122

MOMENI Sina – Thèse de doctorat – 2019-2022

Diffusion non-linéaire en milieu poreux fracturé : application à la détermination du flux matrice-fracture

Résumé :

L'amélioration de la qualité des modéles grande échelle des transferts matrice-fracture qui sont utilisés par la modélisation de type « double-milieu » simulant le transport de fluide ou de chaleur dans les réservoirs géologiques reste un défi majeur pour les applications. Les transferts matrice-fracture comprennent des mécanismes monophasiques et multiphasiques décrits par des équations de diffusion linéaires ou pas.

Dans le cas linéaire, des solutions analytiques fournissent des méthodes de mise à l'échelle pour le transfert matrice-fracture. On observe des comportements temps-courts/longs qui sont également utilisés pour résoudre le transfert diphasique non linéaire.

Dans ce dernier cas, une solution asymptotique originale a été développée aux temps longs. Les solutions analytiques sont en très bon accord avec les résultats des simulations numériques. Finalement, le transfert d'une imbibition capillaire à contre-courant en termes de flux matrice fracture est mis à l'échelle.

Mots clés : Transport en milieux poreux fractures, écoulements polyphasiques, modélisation, imbibition capillaire

Non-linear diffusion in fractured porous media and application to dual-medium inter-porosity flux

Abstract :

Increasing the reliability of large-scale matrix-fracture dual-medium models that are adopted to simulate fluid or heat transport in geological fractured reservoirs remains a major challenge in many applications. Matrix-fracture transfers includes single- and multi-phase mechanisms in linear and non-linear forms.

Analytical solutions of single-phase linear diffusion, with specific initial and boundary condition, provide up-scaling methods for matrix-fracture transfer. This transfer is characterized by early- and late-time behaviours that are also used to solve the non-linear two-phase transfer.

In non-linear case, an exact self-similar solution is adapted for early times and an original asymptotic solution is developed for late times. The analytical solutions are in very good agreement with numerical simulations. A fast-converging algorithm was developed for multi- dimensions. Finally, we scale the transfer of a counter-current capillary imbibition in multi-dimensional system.

Keywords : Transport in fractured porous media, Multi-phase flow, Modelling, Capillary imbibition